Spin-orbit effects and competing magnetic correlations in layered Ruthenates:

A neutron scattering study using floating-zone grown single crystals

Inaugural-Dissertation

zur

Erlangung des Doktorgrades

der Mathematisch-Naturwissenschaftlichen Fakultät

der Universität zu Köln

vorgelegt von

Stefan Kunkemöller

aus Dormagen

Köln, 2018

Contents

Chapter 1

Introduction

The research on condensed matter physics is the physical research field for which most resources are spent at German universities [1]. This outstanding interest is motivated by many applications using the knowledge of solid state physics, which dictate our modern life. The most important and numerous applications can be found in electronics. All modern electronic devices are unimaginable without the research of solid state physics. On the one hand an in depth understanding and accurate theoretical description accelerate the construction of new technical devices, which is impressively demonstrated by the semi conductor industries and the exponential improvement of devices (a very famous example is Moore's law). On the other hand the discovery of new physical effects were brought to application within few years. The discovery of the GMR effect which led to data storage devices is, of course, the one to mention as a student of colognes university, but is also a world class example (Nobel prize 2007!).

In the present work all experiments were performed on Ruthenates, which, of course, all contain the chemical element Ru. Ru is a 4d transition metal, which was largely ignored by science, in contrast to the well studied 3d elements, until recently. Then the Ruthenates started to reveal unique competition between fundamental interactions including spin-orbit coupling, coulomb and exchange interactions [2]. Especially the spin-orbit coupling, which can be treated as a small perturbation in the description of 3d elements and which gains strength with increasing atomic number, strongly influences the electronic and magnetic structure [3]. On the contrary, the tendency for strong correlations is weaker in compounds with 4d elements than with 3d elements. By the more in space extended orbitals of the 4d elements the correlation effects are reduced. Thus these energy scales are brought closer together and subtle changes can cause drastic effects.

All here investigated compounds condense in a structure of the Ruddlesden-Popper series [4]. The basic building block is a Ru ion which is surrounded by O ions forming an octahedron. These octahedrons are corner shared in a plane to form a layer. In the infinite layered compounds, these octahedrons are also connected to octahedrons in the third dimension via corners, to form a 3d structure. In the other layered

compounds there is a rock salt layer interrupting the stacking of the RuO octahedrons in the third dimension regularly, so that singly, doubly, triply etc. layered compounds form. The chemical formulas for these compounds can be described as $A_{n+1}B_nO_{3n+1}$. In this work A=Sr, Ca and B=Ru, Ti and n=1, ∞. Considering the most basic assumptions for the valencies, O is 2- and Sr, Ca are 2+ makes the B ions 4+, a valency favorable for Ru and Ti. Ru 4+ ions have a d^4 configuration. The d electrons solely occupy the t_{2g} orbitals because of the crystal field splitting which raises the e_g orbitals of this 4d element expectedly to too high energies to play a role. The Ti has a d^0 configuration with no unpaired electrons. The degeneracy of the t_{2g} orbitals can be lifted by the Jahn-Teller effect [5]. Following these considerations it is obvious that a picture of rigid octahedrons is only an approximation. Beside becoming distorted the octahedrons can rotate. These subtle changes of the crystal structure play an important role in the properties of layered Ruthenates illustrating that subtle changes of the crystal structure [6] can have drastic effects on the physical properties: Sr_2RuO_4 is a superconductor [7]. By replacing Sr by the isovalent Ca the valency of the ions does not alter, but the structure changes because of the smaller ionic radius of the Ca, which cannot fill space like the larger Sr does. To compensate this the O octahedrons start to rotate, which changes the physical properties drastically. The superconductivity of Sr_2RuO_4 is quickly suppressed by replacing Sr with Ca [8] and the ground state becomes a static magnetic order [9], a spin-density wave [10]. For Ca concentrations greater than 75 % the magnetic susceptibility is considerably larger and metamagnetic transitions occur [8, 11]. For Ca concentrations greater than 90 % the ground state becomes Mott insulating [12, 13].

The first report of a synthesized Ruthenate sample was published in 1959 [14]. But it took a long time, until 1994, to discover the superconductivity in Sr_2RuO_4 [7]. This was the starting point for extensive research of Ruthenates because Sr_2RuO_4 was the first superconductor which is isostructural to several high T_c cuprate superconductors containing no copper. But it took not long and the Ruthenates started to reveal their own fascinating physical properties. The first to mention is the triplet pairing of the cooper pairs, which was proposed quickly [15] and is nowadays, after more than 20 years, still a fascinating research field, which is documented by numerous review articles on that topic, for instance: [16, 17, 18, 19, 20, 21]. A part of this work is dedicated to the question of the pairing mechanism of the cooper pairs, which is closely related to the question of the pairing symmetry [22].

The proposition of triplet pairing was inspired by the ferromagnetism of $SrRuO_3$ [23]. Ferromagnetic spin fluctuations were proposed to be the driving force behind the creation of this rare cooper pairs with parallel spins [15]. Most research on $SrRuO_3$ is nowadays not performed in basic science, but in applied science, in the active field of functional perovskite oxides. There it is mainly used as a conducting layer. But also basic research is mostly performed using epitaxial thin films because of the lack of high quality single crystals [24]. In this work large and high quality single crystals could

be repeatably grown [25]. These crystals have already started to reveal unexpected properties, i.e. the possibility to switch the crystal structure by a magnetic field [26] and a related shape-memory effect. They also turned out to be useful for neutron scattering studies to explore their magnetic properties on a microscopic level 3.2. Even though the main building blocks, the RuO octahedrons, are the same in Sr_2RuO_4 and $SrRuO_3$, the physical properties are very different, on the one hand an unconventional superconductor and on the other hand a bad metallic [27] ferromagnet. These differences are due to the dimensionality of the crystal structure, a further parameter to tune physical properties in the Ruthenates. The tendency to ferromagnetism is nicely seen in Sr-Ru members of the Ruddlesden-Popper series with increasing layer thickness. While in Sr_2RuO_4 the ferromagnetic fluctuations are non-static and can be hardly seen by neutron scattering [28], in $Sr_3Ru_2O_7$ there is already a metamagnetic transition for moderate fields [29] and $Sr_4Ru_3O_{10}$ is a ferromagnet, but with a lower T_c and ordered moment than $SrRuO_3$ [30].

Another way to alter the crystal structure without changing the valencies is chemical substitution. On the A sites Sr is most commonly substituted by Ca [31], but also crystals with Ba were synthesized [32]. Both have the same valency, 2^+, but a different size. While Ba is larger, Ca is smaller than Sr. The already mentioned series $Ca_{2-x}Sr_xRuO_4$ with the rich phase diagram is another topic of the present work. For a long time it was believed that the in Sr rich part of the series the ground state is paramagnetic metallic. But Carlo et al. [9] found static magnetic order in that regime of the chemical substitution with μSR. They tried to prove that this static order is a spin-density wave, like the one occurring in Sr_2RuO_4 with Ti substitution [33], with neutron scattering, but they failed in picking up a conclusive signal [9]. In the present work a spin-density wave has been confirmed in $Ca_{0.5}Sr_{1.5}RuO_4$ by neutron-scattering experiments. The propagation vector amounts to $(0.305, 0.305, 1)$ and the spins freeze in like in spin- or cluster- glasses becoming static at about $4\,K$. [10]. Further work on this series is on the end member Ca_2RuO_4. The trigger to start this work was the proposition that in this compound the spin-orbit coupling is strong enough to couple L and S to J which would lead to a non magnetic ground state. That the ground state is magnetic, which the ground state actually is, namely antiferromagnetic, is explained in their proposition by a mechanism they call excitonic magnetism. This mechanism makes the ground state magnetic if the exchange splitting of the excited magnetic state is larger than the energy difference between the ground state singlet and the excited triplet, which of course requires a strong exchange coupling, see e.g.[5]. In a further step they predicted a peculiar shape for the magnon spectra of this excitonic magnetism [34]. This was the starting point of the work presented here [35, 36]. First, large single crystals had to be grown, which was never done before, because of the first order phase transition slightly above room temperature, which destroys the grown crystals [37, 38]. This problem was overcome by introducing 1% of Ti to the crystal, which did not effect the magnetic properties but made it possible to obtain large crystals suitable for neutron scattering. The neutron

scattering studies on the magnon dispersion were performed at the same time by a group from Stuttgart [39]. Now the magnon dispersion is investigated with all state of the art neutron scattering techniques available, triple axis spectroscopy using cold and thermal neutrons with and without polarization analysis and the time-of-flight technique. While the experimentally obtained data agree, the conclusions drawn of them disagree [35, 39, 40, 36].

The neutron scattering experiments performed in this work use single crystals. In case of Sr_2RuO_4, the needed crystals were available at Cologne University via a cooperation with Y. Maeno. Such excellent crystals were used in numerous studies before [17]. The crystals of $SrRuO_3$ and of the series $Ca_{2-x}Sr_xRuO_4$ with several Ti substitutions had to be grown because no crystals with sufficiently size and quality were available at all. The method of choice to grow Ruthenate single-crystals turned out to be the floating-zone method [41, 31, 17, 42, 43, 44, 25]. So all single crystals were grown with a mirror furnace. The advantages of that method are that no crucible or flux material has to be used, which is a source for contaminations of the obtained single crystals and the size of the crystals are in principle only restricted by the dimensions of the used furnace [45]. All grown samples were examined with x-ray scattering using single crystalline pieces or using crushed parts of them. This gave quick and excellent information about phase purity and single crystallinity. Afterwards the growth parameters were altered and the resulting crystal quality was compared. After some iterations phase purity could be achieved and further methods were used to characterize the crystals, which led sometimes to the necessity to alter again the growth parameters to get even better samples. EDX (energy dispersive X-ray spectroscopy) analysis turned out to be helpful with metallic samples. With metallic samples the residual resistivity is also a good indicator for sample quality, which was determined by a standard four-point method using a liquid He bath to cool down the samples. But also the resistivity of insulating samples was measured, especially to find metal-insulator transitions. The magnetization mesurements were performed using a commercial SQUID (superconducting quantum interference device), which is of course very helpful working with samples showing a rich diversity of magnetic properties.

Neutron scattering [a] does not only demand high quality crystals, but also larger crystals than needed for the most other techniques used in solid state research, because of the weak interaction with matter. But the strength of the interaction with matter is the one property, which makes neutrons an unique tool for science. The neutron interacts with the nucleus of an atom and, because of its spin 1/2, with magnetic moments. The strength of the interaction is for many nuclei in the same order of magnitude like the strength of the interaction with a magnetic moment of 1 μ_B. So it is possible to obtain information about the nuclei and the magnetic moments. The

---

[a]The here given information about neutron scattering can be found in the numerous textbooks about neutron scattering like these: [46, 47, 48]

other important property is the non-zero mass of the neutron. This allows to exchange momentum with the sample in a broad range. Therefore, it is possible to measure excitations throughout the whole Brillouin zone, which is, e.g., with electro-magnetic radiation not possible. That makes neutron scattering a unique method to measure lattice dynamics and magnetic excitations. In diffraction, neutron scattering offers also unique advantages compared to other diffraction methods. The interaction with magnetic moments offers the possibility to determine magnetic structures and the interaction with the nuclei allows to detect lighter elements like hydrogen with much higher precision than X-ray diffraction. The neutrons interaction with both, the nucleus and the magnetic moments, sometimes imply disadvantages when separating the scattering intensities coming from both, the nucleus and the magnetic moments. Here the polarization analysis can help. In the polarization analysis the neutron spin is controlled and the difference of the scattering at nuclei and at magnetic moments allows for distinguishing these two contributions of the scattering. The disadvantage is a severe loss of intensity of the scattering signal. In this work several elastic and inelastic neutron scattering techniques were used to find out where the atoms and magnetic moments are and what they do, respectively. Using a sample of $SrRuO_3$ a diffraction experiment with hot neutrons was performed to determine the crystal structure and to find out the twinning of the sample [25, 26]. The Ru is for all twins in $SrRuO_3$ at the same position due to its higher symmetric position. Though, in order to distinguish the twins it is important to be sensitive to the light O ions, a perfect task for neutron scattering. The output was not only an accurate crystal structure of that compound but also the basis for the following experiments using polarized neutrons. With the knowledge revealed by this experiment it was possible to focus on few key reflections to establish the switching of the twinning structure in an applied magnetic field and a related magnetic shape-memory effect [26]. The spin-density distribution in the unit cell could also be determined using polarized neutron diffraction with the possibility to apply a high magnetic field. With neutron diffraction also the magnetic structure of several $Ca_2Ru_{1-y}Ti_yO_4$ crystals were determined. This was performed using a triple-axis spectrometer, which allows to suppress the background drastically with the usage of the analyzer. This analyzer, of course, allows also for measuring inelastic, which was intensively performed on the $Ca_2Ru_{1-y}Ti_yO_4$ crystals to measure the magnon dispersion. The magnon dispersion was measured with a thermal triple-axis spectrometer and afterwards with a cold one, which provides a better resolution than the thermal one but cannot be used for high energy transfers. Polarized thermal neutrons were used to reliably distinguish between the nuclear and magnetic scattering and, another application of polarized neutrons, to determine the direction of the magnetic moments and the direction of their excitations [35, 36]. For that the neutron spin after the scattering process had to be analyzed in contrast to the polarized diffraction experiment described above. Last but not least the newly upgraded cold triple-axis spectrometer THALES was used to measure the incommensurable magnetic fluctuations in Sr_2RuO_4 [49]. With
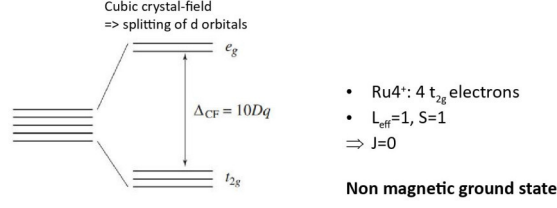
Figure 1.1: *Illustration of the crystal field splitting of the d shell and the realized configuration of Ru^{4+}.*

the good resolution of a cold spectrometer and the high flux of the THALES it was possible to measure these fluctuations to lower energy transfers than ever before [22].

A cohesion of this work is the role of spin-orbit coupling in the investigated Ruthenates, which are $4d$ systems. The spin-orbit coupling strongly increase with the atomic number Z. There are estimations, which show, that the strength of the spin-orbit coupling depends on Z^2 or Z^4, see Chap. 2.3, footnote 5 in Ref. [5]. In the following, aspects of basic concepts like spin-orbit coupling, crystal field splitting and magnetic exchange are presented and reflect their presentation in Ref. [5].

The spin-orbit coupling splits the electronic terms with different total angular momentum. In the LS of Russell-Saunders coupling scheme, there is $J = L + S$, with the total angular momentum J, the total spin S and the total orbital moment L. This coupling scheme is used in the following. There is another coupling scheme, the jj scheme, which holds for very strong spin-orbit coupling. The coupling in the LS scheme can be written as

$$H = \lambda L \cdot S$$

with λ being the spin-orbit coupling constant.

In all layered Ruthenates the Ru is placed in an octahedron of O ions. The resulting cubic crystal field splits the Ru $4d$ states into a doublet and a triplet, the e_g and t_{2g} states, respectively. Covalency effects between the Ru $4d$ and O $2p$ orbitals further increase this splitting. This splitting is big enough to keep the e_g states always unoccupied. The resulting configuration is t_{2g}^4, with a total spin of $S = 1$. In this state the effective orbital moment is $L_{eff} = 1$. Considering the spin-orbit coupling, it becomes apparent that the multiplet with the smallest J is the lowest in energy. Therefore, for the t_{2g}^4 configuration the $J = 0$ state is the lowest in energy, a non-magnetic state, see Fig. 1.2. This state with non-quenched angular momentum is stabilized by the spin-orbit coupling. In a mean field approach the energy gain due to spin-orbit coupling is $\lambda l^z S^z$.
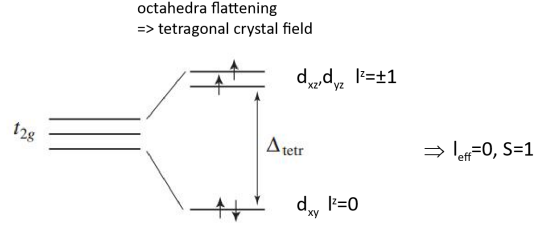
octahedra flattening
=> tetragonal crystal field

t_{2g}

d_{xz}, d_{yz} $l^z = \pm 1$

Δ_{tetr}

$\Rightarrow l_{eff} = 0, S = 1$

d_{xy} $l^z = 0$

Figure 1.2: *Illustration of the crystal field splitting due to a contraction of the O octahedra of the d shell and the realized configuration of Ru^{4+}.*

But the ground state in many Ruthenates is magnetic, at least has an enhanced paramagnetism [23, 8, 30, 33, 9]. There are two possibilities to suppress the non-magnetic ground state in the Ruthenates, crystal fields with lower symmetry than cubic symmetry and exchange interaction.

In case of a contraction of the O octahedra, the dxz and dyz orbitals ($l^z = \pm 1$) are raised in energy while the dxy ($l^z = 0$) is lowered. If the splitting caused by a contraction of the octahedra is large enough the dxy states are doubly occupied and the other two states are singly occupied. Therefore the total angular momentum is quenched and a magnetic state with $S = 1$ is realized. This magnetic state is stabilized by the energy gain of the exchange interaction. An elongation of the octahedra causes the opposite shifting of the energy levels resulting in a non-quenched angular moment and a non-magnetic ground state. This state is stabilized by the spin orbit coupling.

In total, whether the ground state of a Ruthenate is magnetic or not is a question of the interplay between the strength and symmetry of the crystal field, the strength of exchange interaction and spin-orbit coupling.

Spin-density-wave ordering in $Ca_{0.5}Sr_{1.5}RuO_4$ studied by neutron scattering

S. Kunkemöller,[1] A. A. Nugroho,[2] Y. Sidis,[3] and M. Braden[1,*]

[1]*II. Physikalisches Institut, Universität zu Köln, Zülpicher Straße 77, D-50937 Köln, Germany*
[2]*Faculty of Mathematics and Natural Sciences, Institut Teknologi Bandung, Jalan Ganesha 10, 40132 Bandung, Indonesia*
[3]*Laboratoire Léon Brillouin, CEA/CNRS, F-91191 Gif-sur-Yvette Cedex, France*

The spin-density-wave ordering in $Ca_{0.5}Sr_{1.5}RuO_4$ was studied by polarized and unpolarized neutron diffraction experiments. Below about 20 K $Ca_{0.5}Sr_{1.5}RuO_4$ exhibits quasistatic correlations at exactly the incommensurate wave vector at which pure Sr_2RuO_4 shows strong inelastic fluctuations driven by Fermi-surface nesting. The magnetic character of the signal and the orientation of the ordered moments along the c direction can be ascertained by neutron polarization analysis. The magnetic ordering at low temperature is very similar to that found upon minor Ti substitution of Sr_2RuO_4, underlining that this incommensurate spin density wave is the dominant magnetic instability of the unconventional superconductor Sr_2RuO_4.

I. INTRODUCTION

The families of layered ruthenates have attracted strong interest, mostly due to the appearance of unconventional superconductivity in pure Sr_2RuO_4 [1], but many additional fascinating effects can be found in layered ruthenates like a Mott metal-insulator transition with strong involvement of orbital degrees of freedom [2–5], huge linear coefficients of the low-temperature specific heat [6], and metamagnetism associated with quantum criticality [6,7]. Concerning the unconventional superconductivity in Sr_2RuO_4, there is ongoing debate about the symmetry of the order parameter and about the underlying mechanism [8–11]. Many experiments are well interpreted with a triplet p-wave pairing, which can be driven by an interaction between charge carriers and ferromagnetic fluctuations. The magnetic susceptibility in Sr_2RuO_4 indeed is significantly enhanced compared to density functional theory calculations [8], and there also is evidence for ferromagnetic fluctuations in NMR experiments [12]. Inelastic neutron scattering (INS) studied on the magnetic correlations in Sr_2RuO_4, however, reveals dominating incommensurate magnetic excitations [13,14] which arise from Fermi-surface nesting [15] between the sheets related with the d_{xz} and d_{yz} orbital levels, which form almost one-dimensional bands (α,β bands). Ferromagnetic excitations were detected only in polarized INS experiments at higher temperatures [16]; they are less sharp in reciprocal space and exhibit smaller amplitudes. The questions of whether magnetic fluctuations are relevant for the superconducting pairing in Sr_2RuO_4 and if so which ones remain interesting open issues [11].

In order to further analyze the magnetic instabilities of Sr_2RuO_4 one may study magnetically ordered phases that appear upon chemical substitution. Replacing Ru by isovalent Ti, one indeed finds evidence for magnetic ordering already at rather low concentrations of around 2.5% [17,18]. This ordering was shown by neutron scattering experiments to correspond to the same Fermi-surface nesting that causes the strong inelastic excitations in pure Sr_2RuO_4 [19]. Sr_2RuO_4

thus is close to a quantum-critical point associated with the incommensurate spin-density-wave (SDW) magnetic ordering. The magnetic ordering in Ti-substituted Sr_2RuO_4 is only of short range with very weak correlations between the layers and ordered moments point along the c direction, which is in agreement with the anisotropy of the nesting-driven magnetic excitations in pure Sr_2RuO_4 [16].

The substitution of Sr by Ca was intensively studied, leading to the complex phase diagram of $Ca_{2-x}Sr_xRuO_4$ [2,3,6,20,21]. The end member Ca_2RuO_4 is an antiferromagnetic Mott insulator in which only moderate electric fields stabilize a metallic phase [22]. For Sr concentrations around $0.2 \leqslant x \leqslant 0.5$ the magnetic susceptibility is considerably larger and metamagnetic transitions occur [6]. INS experiments reveal various types of magnetic excitations whose competition explains the metamagnetic transitions [23–25]. The nesting-driven magnetic correlations associated with the α,β bands persist in the entire metallic concentration range ($0.2 \leqslant x \leqslant 2$ in $Ca_{2-x}Sr_xRuO_4$), but stronger signals seem to arise from the γ band associated with the d_{xy} orbitals [23,24]. The latter signals are either truly ferromagnetic in nature or incommensurate with propagation vectors much closer to the zone center (see Fig. 1). The region of large Sr content close to the superconducting material was little studied by INS experiments due to the absence of large crystals. However, recent muon spin rotation (μSR) experiments reveal that there is magnetic ordering appearing already for small Ca substitution [26]. Carlo *et al.* find very similar signatures of magnetic ordering in Ti- and Ca-substituted samples indicating that the SDW ordering, which is well documented for Ti substitution, also occurs in $Ca_{2-x}Sr_xRuO_4$ [26]. That Ca and Ti imply the same magnetic instability is astonishing in view of their rather different chemical properties. Furthermore, the SDW order seems to be most stable around the Ca content of $Ca_{0.5}Sr_{1.5}RuO_4$ and gets weakened at larger and lower concentrations [26], although the inelastic neutron scattering studies detect the associated magnetic fluctuations in the entire metallic range of the $Ca_{2-x}Sr_xRuO_4$ phase diagram [25]. By elucidating the magnetic instabilities in the multiband system, $Ca_{2-x}Sr_xRuO_4$ appears interesting not only in view of the unconventional superconductivity in Sr_2RuO_4 but also for the general understanding of the relation between itinerant
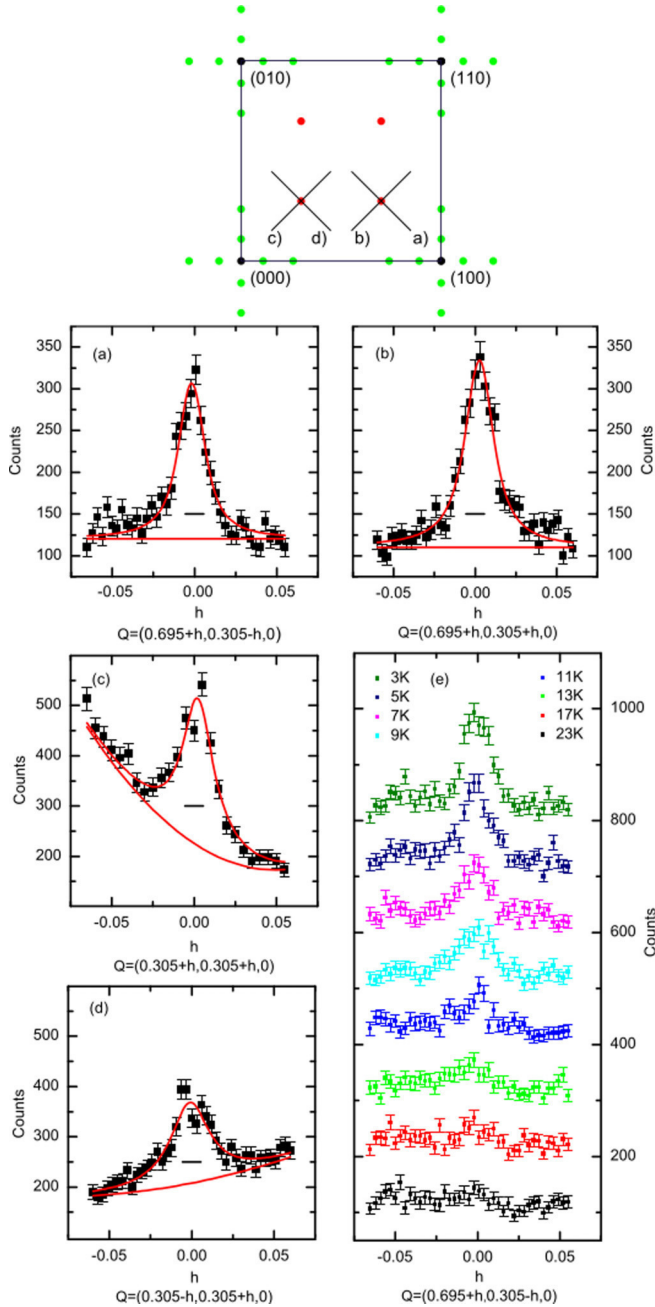
---

*braden@ph2.uni-koeln.de

FIG. 1. (Color online) Neutron diffraction scans across the incommensurate position of the Fermi-surface nesting in $Ca_{0.5}Sr_{1.5}RuO_4$; the upper part gives a scheme of the Brillouin zone with the black dots indicating the two-dimensional zone centers where truly ferromagnetic correlation are located; green dots indicate the position of strong incommensurate correlations in $Ca_{2-x}Sr_xRuO_4$ at large Ca content ($0.2 \leqslant x \leqslant 0.6$ [25]) while the red dots indicate the position of the incommensurate SDW ordering arising from the nesting of the α,β bands. Symbols in panels (a) to (d) correspond to the scans performed at low temperature and lines are fits by Lorentzian distributions folded with the resolution function of the instrument. Panel (a) shows a longitudinal scan parallel to the in-plane component of the modulation vector across (0.305,0.695,0) while panel (b) shows the transversal scan. Panels (c) and (d) show longitudinal and transverse scans, respectively. Scan directions (a)–(d) are illustrated in the upper part. Part (e) presents the temperature dependence of the transversal scan across (0.305,0.695,0).

magnetism and superconductivity in multiorbital systems like, e.g., the Fe-based superconductors.

Here we have grown single crystals of $Ca_{0.5}Sr_{1.5}RuO_4$ and studied them by various neutron scattering techniques and macroscopic methods. In $Ca_{0.5}Sr_{1.5}RuO_4$ magnetic SDW ordering occurs below 20 K and resembles in all aspects studied the SDW ordering in Ti-substituted Sr_2RuO_4 [19]. This underlines the importance of the incommensurate magnetic instability for pure and superconducting Sr_2RuO_4.

II. EXPERIMENTAL

Single crystals of $Ca_{0.5}Sr_{1.5}RuO_4$ were grown by the Ru self-flux traveling floating-zone technique in an image furnace (Canon SC1-MDH-11020) at Cologne University. A feed rod was synthesized following the procedures reported in Ref. [27] while the single-crystal growth was performed as described in Ref. [28]. We identified the following as good growth parameters: growth speed of 25 mm/h; 3.2 bar pressure with 5 l/min argon flow and with 0.25 l/min oxygen flow; and the upper and the lower shafts were rotated in opposite direction at 25 rotations per minute. With this procedure large crystals of up to 1200 mm³ volume could be obtained. Small parts were crushed into powders to perform x-ray diffraction experiments, which did not yield any evidence for an impurity phase. The largest grain was characterized by neutron diffraction, yielding a mosaic spread below 0.5 deg.

Lattice constants were determined by x-ray powder diffraction on a Siemens D5000 diffractometer using Cu K_α radiation ($a = 3.836(2)$ and $c = 12.740(2)$ Å at room temperature). Magnetic susceptibility and magnetization were studied by a superconducting quantum interference device (SQUID) magnetometer. Resistivity measurements were performed with the four-point method.

Elastic neutron scattering experiments were performed with the cold triple-axis spectrometers 4F1 and 4F2 at the Orphée reactor in Saclay. For the unpolarized experiments a double monochromator and an analyzer using the (002) reflection of pyrolytic graphite were utilized, and a Be filter was set between the sample and the analyzer in order to suppress higher-order contaminations. The crystal was oriented in the [100]/[010] scattering geometry and cooled with an Institut-Laue-Langevin-orange-type cryostat. For the polarization analysis we introduced a bender between the monochromator and the sample, and a polarized Heusler crystal was used as analyzer. The polarization of the neutron was guided with a Helmholtz setup. The flipping ratio measured on a nuclear Bragg peak amounted to about 50, documenting the high precision of the polarization setup.

III. RESULTS AND DISCUSSION

Figure 1 shows the main results of our studies. At the position of the Fermi-surface nesting in pure Sr_2RuO_4 we find elastic scattering at low temperature, indicating that $Ca_{0.5}Sr_{1.5}RuO_4$ undergoes the same transition into the SDW phase as Ti-substituted Sr_2RuO_4, in perfect agreement with the interpretation of the μSR experiments [19,26]. Note that (100) is not a zone center in the reciprocal lattice of the body-centered crystal structure of Sr_2RuO_4 (space group $I4/mmm$ with lattice
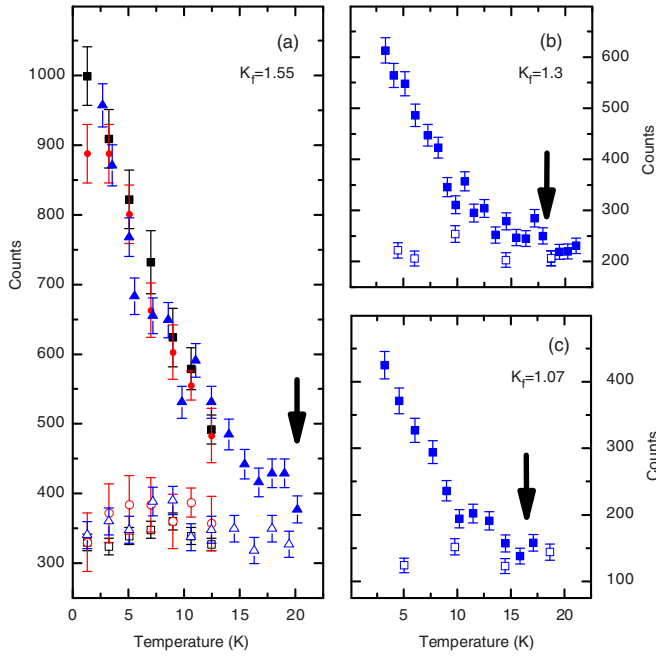
FIG. 2. (Color online) Temperature dependence of the magnetic scattering in Ca$_{0.5}$Sr$_{1.5}$RuO$_4$. Panel (a) gives the results obtained with $k_f = 1.55$ Å^{-1}: Filled symbols denote the intensity at the SDW position and open symbols indicate the background (blue symbols denote counting at the peak position and at the background while black and red symbols correspond to the peak and background values obtained by fitting the transverse and longitudinal scans, respectively). Panels (b) and (c) give the same intensities obtained with $k_f = 1.3$ Å^{-1} and $k_f = 1.07$ Å^{-1}, respectively. Vertical arrows indicate the onset temperature of magnetic scattering at the SDW position that varies for different k_f.

FIG. 3. (Color online) In-plane coherence lengths of the SDW ordering in Ca$_{0.5}$Sr$_{1.5}$RuO$_4$ determined by fitting the raw data with the convolution of Lorentzian peak shape and the resolution function of the instrument; panels (a) and (b) show the longitudinal and transversal correlation lengths, respectively.

parameters of about 3.8·3.8·12.8 Å^3). The crystal structure of Ca$_{0.5}$Sr$_{1.5}$RuO$_4$ is of lower symmetry (space group I4$_1$/acd [23]) due to the rotation of the RuO$_6$ octahedron, which we ignore throughout this paper. We label all reciprocal space vectors in reduced lattice units with respect to the tetragonal cell of pure Sr$_2$RuO$_4$. The observation of magnetic scattering at (0.6955(10),0.3045(10),0) thus points to a propagation vector of (0.305,0.305,1), which is identical to the one found in Ti-substituted Sr$_2$RuO$_4$ [19] and which perfectly agrees with the position of the inelastic fluctuations in pure Sr$_2$RuO$_4$ [13,14]. The $q_l = 1$ value indicates that there is a phase shift between two neighboring layers, but the correlation between the layers is very weak. There is also sizable intensity at (0.305,0.305,0) and (0.695,0.695,0), which after consideration of the Ru form factor and scattering geometry is only ∼2.5 times weaker than the signal at (0.695,0.305,0). Again this is very similar to the Ti substitution, which also induces very little interplane correlations [19].

The temperature dependence of the magnetic scattering is summarized in Fig. 2. Panel (a) shows that magnetic scattering appears near 20 K when measured with $k_f = 1.55$ Å^{-1}. Panels (b) and (c) show the data obtained with better resolution, $k_f = 1.3$ Å^{-1} and $k_f = 1.07$ Å^{-1}. From the larger to the lower k_f the energy resolution (full width at half maximum) increases from 0.19 to 0.11 and 0.05 meV. One clearly sees that
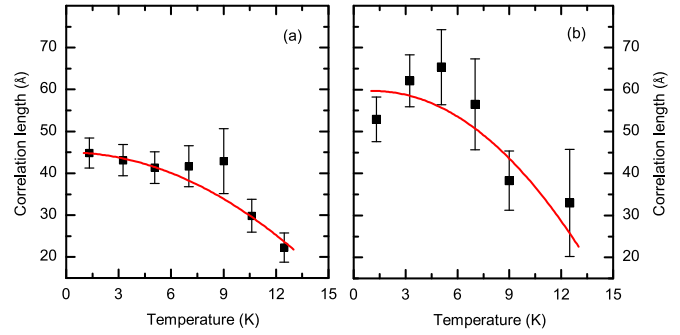
the onset of magnetic scattering shifts to lower temperatures with better resolution, from ∼21 K to ∼18 K and ∼16 K. This behavior suggests a spin freezing similar to spin glasses or cluster glasses [29] as the time windows of the experiments correspond to 3.4, 6, and 13 ps, respectively. In the temperature range from 21 to 16 K the SDW fluctuations thus slow down through the time scale range between a few to tens of picoseconds. We may compare the time scales of our neutron experiments with that of the μSR experiments, which is of the order of 0.1 to 1 μs, and indeed μSR finds a still lower transition temperature of 12 K [26]. Finally the irreversibility between field-cooled and zero-field-cooled susceptibility data, which can be considered as static, lies at the further reduced temperature of 5 K; see below.

The correlation lengths of the SDW ordering in Ca$_{0.5}$Sr$_{1.5}$RuO$_4$ as obtained from the scans similar to those of Fig. 1 are shown in Fig. 3. The raw data were fitted with Lorentzian folded with the instrument resolution, and the coherence lengths were obtained as $\xi = \frac{1}{\kappa}$ with κ the half-width at half-maximum of the Lorentzian distribution. The scattering remains broadened well above the instrument resolution even at the lowest temperature where the in-plane correlation length is roughly isotropic and amounts to ∼50 Å. In spite of the rather different character of the substitution, this value again perfectly agrees with the result obtained by 9% Ti insertion [19].

Due to the low correlation lengths, weak intensities, and possible extinction contamination, a precise determination of the ordered moment is impossible. The ratio between the magnetic peak intensity and the (110) Bragg reflection signal amounts to $\frac{1}{54000}$ in Ca$_{0.5}$Sr$_{1.5}$RuO$_4$, which in close analogy with the Ti substitution (in Sr$_2$Ru$_{0.91}$Ti$_{0.09}$RuO$_4$ this ratio amounts to $\frac{1}{109000}$) indicates an ordered magnetic moment of about 0.42(15)μ_B.

In order to ascertain the magnetic character of the scattering and to determine the orientation of the ordered moment we have performed a polarized neutron experiment. We use the conventional coordinate system in polarized neutron scattering [30] with the x direction along the scattering vector, z vertical to the scattering plane, and y perpendicular to both x and z. This experiment finds the SDW signal in the spin-flip channel for x polarization, which documents the magnetic nature of the
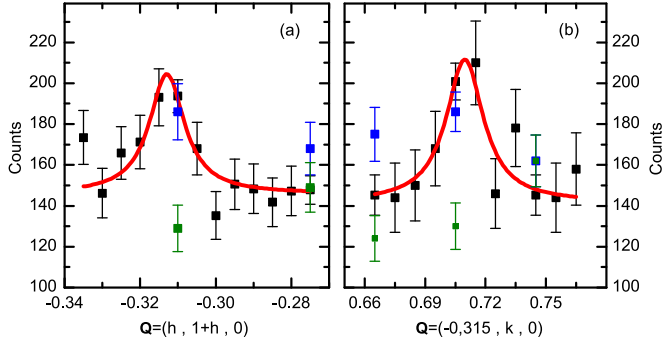
FIG. 4. (Color online) Results of polarized neutron scattering experiments on $Ca_{0.5}Sr_{1.5}RuO_4$. Black, blue, and green symbols denote the intensities in the spin-flip channels for neutron polarization along the x, y, and z directions respectively.

FIG. 5. (Color online) Temperature dependence of the magnetic susceptibility in $Ca_{0.5}Sr_{1.5}RuO_4$ measured with a SQUID magnetometer in fields of 0.1 T along and perpendicular to the c axis; lines in panel (b) are fits with a modified Curie-Weiss law. The data for the in-plane susceptibility in part (b) were shifted by -1×10^{-3} emu/mol for clarity. The inset shows the deviation between field-cooled and zero-field-cooled data below 5 K for the field aligned along the c direction.

signal; see Fig. 4. In addition the signal appears in the spin-flip y channel and not in the spin-flip z channel. This indicates that the ordered moment points along the c direction, which again agrees with the finding for Ti substitution [19] and with the anisotropy of the inelastic nesting signal in pure Sr_2RuO_4 [16].

In all aspects studied, the magnetic orderings in $Sr_2Ru_{1-x}Ti_xO_4$ with $x = 0.09$ and in $Ca_{0.5}Sr_{1.5}RuO_4$ (0.5 Ca per Ru site) are comparable in spite of the very different chemical character of the two replacements. In the case of Ti, one may expect a local weakening of the hopping parameter, t, which enhances the effect of the correlations and thereby causes SDW ordering. The phase diagram of $Ca_{2-x}Sr_xRuO_4$ has been analyzed by density functional calculations, which indicate a strong reduction of the γ band width [31] but less effects on the one-dimensional bands associated with the nesting instability. However, Ca with a much smaller ionic radius and thus with a different crystallographic position may modify the local electronic structure and induce local structural distortions. Upon introduction of Ca, the tetragonal crystal structure of Sr_2RuO_4 first gets distorted by the octahedron rotation around the c axis [21]. This structural phase transition exhibits strong disorder effects partially due to the weak interlayer coupling of the rotation distortion. Long-range order is found only around $Ca_{0.5}Sr_{1.5}RuO_4$ [21]. It appears astonishing that higher Ca contents destabilize the SDW magnetic ordering [26], although the corresponding correlations can be seen in the entire metallic part of the phase diagram [25]. Eventually, the maxima in magnetic ordering temperatures and in ordered moments [26] are related with disorder, whose influence on the physical properties is well documented [32], but the question of why further increase of the Ca content destabilizes the SDW ordering merits further attention.

A comparable neutron diffraction experiment was also performed for $Ca_{0.05}Sr_{1.95}RuO_4$ [33] but did not yield any indication for SDW ordering, in good agreement with the μSR experiments, which also do not find evidence for magnetic ordering for this composition.

The magnetic susceptibility measured with a SQUID magnetometer in fields of 0.1 T along and perpendicular to the c axis is shown in Fig. 5. The temperature dependence can be reasonably well described by the sum of a constant
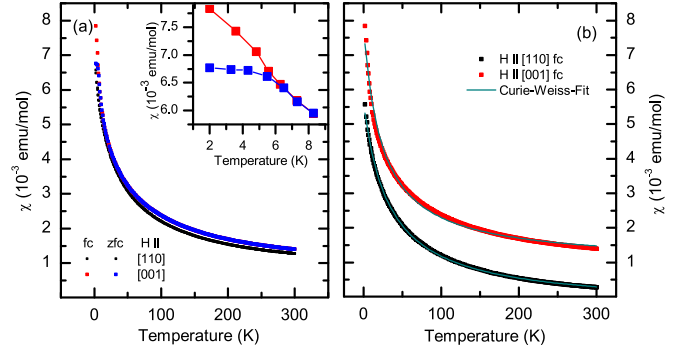
and a Curie-Weiss term, $\chi = \chi_0 + \frac{C}{T-\Theta}$ with $C = \frac{N_A p_{eff}^2 \mu_B^2}{3k_B}$, yielding the values $\chi_0 = 0.837(9)/0.663(3) \times 10^{-3}$ emu/mol, $p = 1.26(1)/1.29(1)\mu_B$/Ru, and $\theta = -32.5(5)/-36.0(2)$ K for field along [001]/[110] directions, respectively. Below 5 K, field-cooled and zero-field-cooled data split, indicating truly static ordering. Magnetization hysteresis cycles were measured for both field directions up to 7 T; see Fig. 6. In both directions pronounced nonlinearities are observed. For the field along the c direction there is a finite remanent magnetization left, indicating a weak ferromagnetic contribution. In order to illustrate the latter we have subtracted in Fig. 6(b) the linear part of the magnetization, yielding a ferromagnetic contribution of $0.01\mu_B$ per formula unit at 7 T. This moment is well below the antiferromagnetically ordered moment of the SDW phase (of the order of $0.4\mu_B$ per formula unit) and should thus be considered as a secondary effect. There are different possibilities to explain this ferromagnetic component.
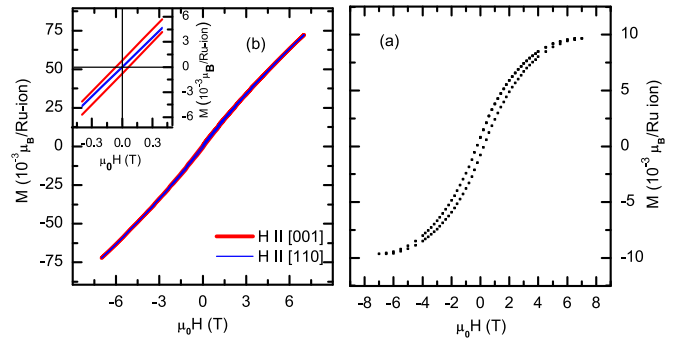
FIG. 6. (Color online) Magnetization hysteresis cycles measured at $T = 2$ K for fields along the [110] and [001] directions (a). The insert zooms into the small field part of the hysteresis to illustrate the finite remanent magnetization obtained with the magnetic field along the c direction. Data of the magnetization hysteresis for fields along c in part (b) were obtained by subtracting the linear contribution to the field dependence to separate the weak ferromagnetic signal.
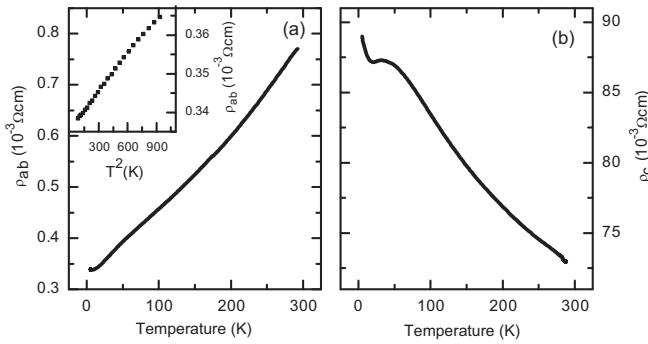
FIG. 7. Temperature dependence of the in-plane and out-of-plane resistivity in Ca$_{0.5}$Sr$_{1.5}$RuO$_4$.

Due to the short coherence lengths sizable ferromagnetic magnetization can arise from field-driven changes of the shapes of the SDW clusters. The ferromagnetic component is also observed in the case of the Ti substitution, although the amounts and the positions of the dopant are so different, but note that the correlation lengths are comparable in both systems. Ferromagnetism in Ca$_{2-x}$Sr$_x$RuO$_4$ is commonly associated with the γ band and its van Hove singularity, which most likely also causes the incommensurate magnetic signals at much smaller wave vector; see Fig. 1 and Ref. [25]. It is possible that the ferromagnetic contribution appearing in the SDW phase induced by Ca or by Ti substitution is an intrinsic effect associated with this γ band.

Ca$_{0.5}$Sr$_{1.5}$RuO$_4$ exhibits strongly anisotropic behavior in its electric resistivity, which is two orders of magnitude larger along the c direction; see Fig. 7. Perpendicular to the layers, the resistivity continuously increases upon cooling down to a maximum near 30 K. Further cooling leads to a slight reduction of resistivity until the onset of quasistatic SDW ordering becomes visible in a resistivity uptake, which can be explained by the opening of at least a partial gap. The resistivity along the layers decreases upon cooling without direct signatures of the SDW ordering. However, below about 25 K the in-plane resistivity roughly exhibits a T^2 behavior on top of a large residual resistivity. We may emphasize that this crossover in electric resistivity coincides with the appearance of the quasistatic SDW correlations.

IV. CONCLUSIONS

The combination of neutron scattering and macroscopic methods unambiguously proves that Ca$_{0.5}$Sr$_{1.5}$RuO$_4$ exhibits incommensurate SDW ordering at the same propagation vector where pure Sr$_2$RuO$_4$ shows strong inelastic fluctuations driven by the nesting of Fermi surfaces. In all studied aspects this SDW phase in Ca$_{0.5}$Sr$_{1.5}$RuO$_4$ resembles that observed in Ti-substituted Sr$_2$RuO$_4$, confirming the previous μSR experiments [26]. This close similarity may appear astonishing as the chemical replacement is so different in the two cases. Ti directly enters the RuO$_2$ layers and 9% of Ti per formula unit seem to possess a similar impact as 50% of Ca per formula unit. In spite of the fact that Ca does not directly affect the RuO$_2$ layers, the nature of the SDW phase and in particular the correlation lengths are comparable. In first view the main difference between Ca and Sr concerns the smaller ionic radius of Ca, which introduces a structural distortion associated with the rotation of the RuO$_6$ octahedra around the c axis. However, the present results suggest that there is also a direct impact on the surrounding Ru sites.

Neutron scattering clearly documents the incommensurate character of the ordering in Ca$_{0.5}$Sr$_{1.5}$RuO$_4$ and the alignment of ordered moments along the c direction. The latter reflects the spin-orbit-coupling-driven anisotropy seen in pure Sr$_2$RuO$_4$. The observation of the SDW phase in a second system underlines the relevance of this magnetic instability in pure Sr$_2$RuO$_4$, whose superconducting properties appear difficult to reconcile with the nesting fluctuations [11].

[1] Y. Maeno, H. Hashimoto, K. Yoshida, S. Nishizaki, T. Fujita, J. G. Bednorz, and F. Lichtenberg, Nature (London) **372**, 532 (1994).

[2] S. Nakatsuji and Y. Maeno, Phys. Rev. Lett. **84**, 2666 (2000).

[3] G. Cao, S. McCall, M. Shepard, J. E. Crow, and R. P. Guertin, Phys. Rev. B **56**, R2916 (1997).

[4] M. Braden, G. André, S. Nakatsuji, and Y. Maeno, Phys. Rev. B **58**, 847 (1998).

[5] E. Gorelov, M. Karolak, T. O. Wehling, F. Lechermann, A. I. Lichtenstein, and E. Pavarini, Phys. Rev. Lett. **104**, 226401 (2010).

[6] S. Nakatsuji and Y. Maeno, Phys. Rev. B **62**, 6458 (2000); S. Nakatsuji, D. Hall, L. Balicas, Z. Fisk, K. Sugahara, M. Yoshioka, and Y. Maeno, Phys. Rev. Lett. **90**, 137202 (2003).

[7] R. S. Perry, L. M. Galvin, S. A. Grigera, L. Capogna, A. J. Schofield, A. P. Mackenzie, M. Chiao, S. R. Julian, S. I. Ikeda, S. Nakatsuji, Y. Maeno, and C. Pfleiderer, Phys. Rev. Lett. **86**, 2661 (2001).

[8] A. P. Mackenzie and Y. Maeno, Rev. Mod. Phys. **75**, 657 (2003).

[9] Y. Maeno, S. Kittaka, T. Nomura, S. Yonezawa, and K. Ishida, J. Phys. Soc. Jpn. **81**, 011009 (2012).

[10] S. Raghu, A. Kapitulnik, and S. A. Kivelson, Phys. Rev. Lett. **105**, 136401 (2010).

[11] J.-W. Huo, T. M. Rice, and F.-C. Zhang, Phys. Rev. Lett. **110**, 167003 (2013).

[12] T. Imai, A. W. Hunt, K. R. Thurber, and F. C. Chou, Phys. Rev. Lett. **81**, 3006 (1998).

[13] Y. Sidis, M. Braden, P. Bourges, B. Hennion, S. NishiZaki, Y. Maeno, and Y. Mori, Phys. Rev. Lett. **83**, 3320 (1999).

[14] M. Braden, Y. Sidis, P. Bourges, P. Pfeuty, J. Kulda, Z. Mao, and Y. Maeno, Phys. Rev. B **66**, 064522 (2002).

[15] I. I. Mazin and D. J. Singh, Phys. Rev. Lett. **79**, 733 (1997).

[16] M. Braden, P. Steffens, Y. Sidis, J. Kulda, P. Bourges, S. Hayden, N. Kikugawa, and Y. Maeno, Phys. Rev. Lett. **92**, 097402 (2004).

[17] M. Minakata and Y. Maeno, Phys. Rev. B **63**, 180504 (2001).

[18] N. Kikugawa and Y. Maeno, Phys. Rev. Lett. **89**, 117001 (2002).

[19] M. Braden, O. Friedt, Y. Sidis, P. Bourges, M. Minakata, and Y. Maeno, Phys. Rev. Lett. **88**, 197002 (2002).

[20] S. Nakatsuji, S. Ikeda, and Y. Maeno, J. Phys. Soc. Jpn. **66**, 1868 (1997).

[21] O. Friedt, M. Braden, G. André, P. Adelmann, S. Nakatsuji, and Y. Maeno, Phys. Rev. B **63**, 174432 (2001).

[22] F. Nakamura, M. Sakaki, Y. Yamanaka, S. Tamaru, T. Suzuki, and Y. Maeno, Sci. Rep. **3**, 2536 (2013).

[23] O. Friedt, P. Steffens, M. Braden, Y. Sidis, S. Nakatsuji, and Y. Maeno, Phys. Rev. Lett. **93**, 147404 (2004).

[24] P. Steffens, Y. Sidis, P. Link, K. Schmalzl, S. Nakatsuji, Y. Maeno, and M. Braden, Phys. Rev. Lett. **99**, 217402 (2007).

[25] P. Steffens, O. Friedt, Y. Sidis, P. Link, J. Kulda, K. Schmalzl, S. Nakatsuji, and M. Braden, Phys. Rev. B **83**, 054429 (2011).

[26] J. P. Carlo, T. Goko, I. M. Gat-Malureanu, P. L. Russo, A. T. Savici, A. A. Aczel, G. J. MacDougall, J. A. Rodriguez, T. J. Williams, G. M. Luke, C. R. Wiebe, Y. Yoshida, S. Nakatsuji, Y. Maeno, T. Taniguchi, and Y. J. Uemura, Nat. Mater. **11**, 323 (2012).

[27] S. Nakatsuji and Y. Maeno, J. Sol. State Chem. **156**, 26 (2001).

[28] Z. Q. Mao, Y. Maeno, and H. Fukazawa, Mater. Res. Bull. **35**, 1813 (2000).

[29] B. R. Coles, B. V. B. Sarkissian, and R. H. Taylor, Philos. Mag. B **37**, 489 (1978).

[30] B. Chatterji (ed.), *Neutron Scattering from Magnetic Materials* (Elsevier, Amsterdam, 2006).

[31] Z. Fang and K. Terakura, Phys. Rev. B **64**, 020509(R) (2001); Z. Fang, N. Nagaosa, and K. Terakura, *ibid.* **69**, 045116 (2004).

[32] J. Zhang, Ismail, R. G. Moore, S.-C. Wang, H. Ding, R. Jin, D. Mandrus, and E. W. Plummer, Phys. Rev. Lett. **96**, 066401 (2006).

[33] M. Braden and Y. Sidis (private communication). By using the same spectrometer configuration for $Ca_{0.05}Sr_{1.95}RuO_4$ at 2.55 K, a peak of 2×10^{-6} times the intensity of the (110) Bragg reflection would have been observed at the SDW position, resulting in an upper limit for the ordered moment of about $0.15\mu_B$ per Ru in $Ca_{0.05}Sr_{1.95}RuO_4$ at 2.55 K.

Highly Anisotropic Magnon Dispersion in Ca_2RuO_4: Evidence for Strong Spin Orbit Coupling

S. Kunkemöller,[1] D. Khomskii,[1] P. Steffens,[2] A. Piovano,[2] A. A. Nugroho,[3] and M. Braden[1,*]

[1]*II. Physikalisches Institut, Universität zu Köln, Zülpicher Str. 77, D-50937 Köln, Germany*
[2]*Institut Laue Langevin, 6 Rue Jules Horowitz BP 156, F-38042 Grenoble CEDEX 9, France*
[3]*Faculty of Mathematics and Natural Sciences, Institut Teknologi Bandung, Jl. Ganesha 10, Bandung 40132, Indonesia*
(Received 23 July 2015; published 8 December 2015)

The magnon dispersion in Ca_2RuO_4 has been determined by inelastic neutron scattering on single crytals containing 1% of Ti. The dispersion is well described by a conventional Heisenberg model suggesting a local moment model with nearest neighbor interaction of $J = 8$ meV. Nearest and next-nearest neighbor interaction as well as interlayer coupling parameters are required to properly describe the entire dispersion. Spin-orbit coupling induces a very large anisotropy gap in the magnetic excitations in apparent contrast with a simple planar magnetic model. Orbital ordering breaking tetragonal symmetry, and strong spin-orbit coupling can thus be identified as important factors in this system.

The properties of strongly correlated systems with significant spin-orbit coupling (SOC) present a challenging problem. For most $3d$ transition-metal compounds one can treat SOC as a weak perturbation. It leads to single-site and exchange magnetic anisotropy, possibly to an antisymmetric (Dzyaloshinskii-Moriya) exchange, and it largely determines the magnetoelastic coupling and magnetostriction. The situation can be different in case of strong SOC, which causes novel phenomena such as the anomalous Hall effect [1], the spin Hall effect [2], and topological insulators [3,4]. Strong SOC is able to change the character of the multiplet state of the corresponding ions, which is intensively studied for the case of the reduction of the magnetic state of Ir^{4+} (electronic structure $5d^5$ or t_{2g}^5, $L_{eff} = 1$, $S = 1/2$) to an effective Kramers doublet with $j = 1/2$ [5]. But even more drastic effects can be expected for heavy ions with d^4 occupation (t_{2g}^4, $L_{eff} = 1$, $S = 1$), e.g., in Ir^{5+}, Ru^{4+}, Os^{4+}, etc. [6]. According to Hund's rules (generalized for ions sensing crystal electric fields) the ground state should be a nonmagnetic singlet with $j = 0$; see, e.g., Refs. [7,8]. And, indeed, isolated Ir^{5+} ions and also most of the concentrated Ir^{5+} compounds are nonmagnetic, although a few magnetic Ir^{5+} cases are known [9]. In a solid, magnetic order can occur even if the ground state of an isolated ion is a singlet, see Chap. 5.5 in Ref. [8], but it requires a strong exchange interaction, so that the exchange splitting of excited magnetic states (in the Ru^{4+} case a $j = 1$ triplet) is larger than the energy difference between the ground-state singlet and the excited triplet, which is given by the SOC parameter λ. The SOC can also be at least partially suppressed by a noncubic crystal field (CF), Δ_{noncub}, which splits the t_{2g} ($L_{eff} = 1$) triplet and stabilizes real orbitals. Both these factors, CF and magnetic interaction, can combine to suppress the $j = 0$ state and to eventually induce the magnetically ordered ground state. In terms of energy scales, one should expect such magnetic ordering for $\Delta_{noncub} + \mu H_{exch} > \lambda$, which seems quite unlikely for Ir^{5+}, where $\lambda = (\zeta/2S) = \zeta/2$ amounts to 0.2 to 0.25 eV (ζ is the atomic spin-orbit parameter). But for $4d$ compounds this relation can easily be reached, as for Ru^{4+} $\lambda \sim 0.075$ eV [6,10]. Indeed, practically all Ru^{4+} compounds order magnetically aside from the metallic ones— and even some metallic ruthenates are magnetic, such as the ferromagnetic metal $SrRuO_3$. The persisting role of SOC in these magnetic Ru^{4+} compounds is an intriguing open issue.

Ca_2RuO_4 (CRO) is such a Ru^{4+} case, which has been intensively studied as the Mott-insulating analogue of the unconventional superconductor Sr_2RuO_4 [11–14]. CRO exhibits a metal-insulator (MI) transition at 357 K, which is accompanied by a flattening of the RuO_6 octahedra [13–16]. This flattening continues upon further cooling until it saturates near the onset of magnetic order at $T_N \sim 110$ K. The magnetic structure is antiferromagnetic (AFM) with moments aligned parallel to the layers [13,16]; see Fig. 1(a). The electronic structure has been studied by various approaches [17–21]. From the spectroscopic study of CRO it was concluded that SOC indeed plays an important role but is not sufficiently strong to stabilize the $j = 0$ state [17]. Density functional theory calculations indicate a pronounced shift in orbital polarization leading to almost full electron occupation of the d_{xy} levels at low temperature [18–22]. More recently, the $j = 0$ state was explicitly proposed for CRO [6,10]. Starting from the scenario of strong SOC and including noncubic CF and intersite exchange, the magnetically ordered state in CRO is reproduced and several unusual features of the magnetic excitation spectrum of CRO are predicted, such as a peculiar shape and large width. The alternative, more conventional picture is to attribute the magnetism of
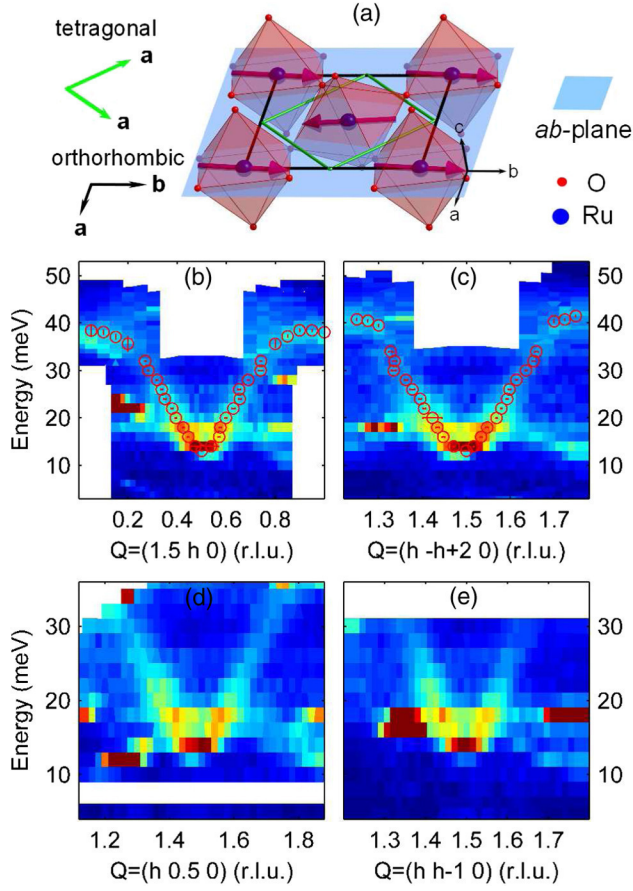
FIG. 1 (color online). (a) Sketch of the magnetic and crystal structure of CRO; only a single layer of RuO$_6$ octahedra is shown (Ru in blue balls, O in small red points) including the tetragonal and larger orthorhombic cells. Note that magnetic moments are slightly canted (by about 6 degrees) resulting in a weak ferromagnetic component in such a single layer [13]. The small arrows added at the tip of the rightmost moment indicate the polarization of the two transversal and the longitudinal modes. (b)–(e) Intensity distribution in energy versus scattering vector **Q** planes taken at 2 K around the (1.5 0.5 0) magnetic zone center. (b) and (d) The symmetrically equivalent dispersion along the $(0, \xi, 0)$ and $(\xi, 0, 0)$ directions, subplot (c) and (e) along $(\xi, \xi, 0)$ and $(\xi, -\xi, 0)$. The color coding corresponds to the raw data. Open symbols indicate the dispersion obtained by fitting single scans. Data were taken on IN8 with final energies of 35 meV for constant **Q** scans at high energy transfer and 14.7 meV elsewhere.

CRO to the conventional $S \sim 1$ state of Ru^{4+} ions, with SOC playing a less significant but still prominent role. In this case one can describe the magnetic state, including spin waves, by the usual exchange Hamiltonian.

Here we present an inelastic neutron scattering (INS) study and spin-wave calculations of the magnetic excitations in CRO. Details of the INS experiments and on the sample characterization of the crystals containing 1% of Ti are given in the Supplemental Material [23]. We find that a conventional model can well describe the obtained dispersion, while there are considerable differences with

the proposed $j = 0$ model [10]. Most interestingly, there is a sizable spin gap which indicates that rotating the magnetic moment within the layers costs large energy. The breaking of the local tetragonal symmetry and the associated orbital polarization, which has been neglected in theory so far [18–22], are important parameters to understand the magnetism in CRO.

Figures 1(b)–1(e) show color mappings of the measured intensity distribution. Because of the weakness of scattering in CRO (small moment and rapidly decreasing form factor) contaminations by various phonon branches are highly visible. By analyzing and comparing results taken in different Brillouin zones and geometries the dispersion can be unambiguously determined. Magnon excitations start at the AFM Bragg points $((2n_h + 1)/2$ $(2n_k + 1)/2$ $n_l)$ with integer n_h, n_k, and n_l. However, there is a sizable spin gap of 13.04(5) meV. For a square planar antiferromagnet the magnon dispersion extends from **Q** = (0.5 0.5) to (0.75 0.75) in the [1 1] direction, as (1 1) is a Bragg point, and to (0 0.5) in the [1 0] direction. **Q** = (0.25 0.25) and (0 0.5) are AFM Brillouin zone boundaries. In CRO there is, however, a severe structural distortion [16]. Some characteristic scans performed to determine the magnon dispersion in CRO are shown in Fig. 2. Constant energy scans at intermediate energy cut through the magnon cones at two positions. Constant **Q** scans taken
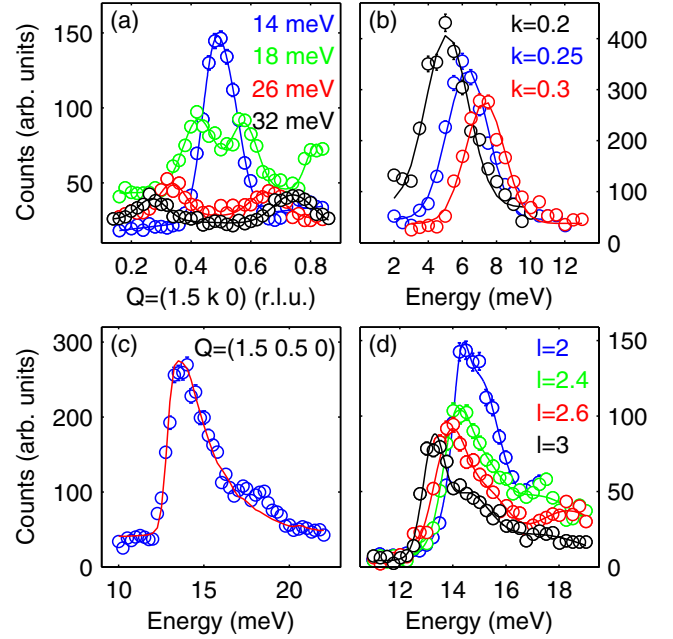
FIG. 2 (color online). Several characteristic scans taken at 2 K on IN8: (a) Constant energy scans at (1.5, k, 0) fitted with Gaussians and background. (b) Phonon scans taken at **Q** = $(\xi, 2, 0)$; the lines correspond to the folding of the resolution function with a simple linear phonon dispersion. No additional parameter is needed to describe the shape of the intensity profile. (c) and (d) Energy scans at the zone center (1.5 0.5 0) and at (0.5 0.5 l).

just at the AFM zone center show a characteristic asymmetric shape, see Figs. 2(c) and 2(d): Intensity rapidly increases when crossing the spin gap and slowly diminishes with further energy increase. We have calculated the folding of the spin-wave dispersion including its expected signal strength with the experimental resolution using the RESLIB [24] package and verified that scans across transversal acoustic phonons are well reproduced; see Fig. 2(b). The steep spin wave dispersion perfectly describes the asymmetric shape of the spectra taken at the zone center; see Fig. 2(c). The total width of the dispersion is low, as maximum energies of 37.8(3) and 41.2(5) meV are reached at the magnetic zone boundaries, $(0.5\,0\,0)$ and $(0.25\,0.25\,0)$.

In order to describe the magnon dispersion we use a conventional Heisenberg equation: $H = \sum_{\mathbf{i},\mathbf{j}} J_{i,j} \mathbf{S_i} \cdot \mathbf{S_j} - \delta \sum_i (S_i^y)^2$. We include a single-site anisotropy term arising from SOC but note that anisotropic exchange parameters would lead to similar results. The model for fully dominant SOC is presented in Ref. [10]. We set $S = 0.67$ following the neutron diffraction study [13]. The sum runs over pairs of magnetic ions, so that each pair or bond appears twice. Spin waves were calculated with the Holstein-Primakoff transformation as described in Refs. [25,26]. We include the nearest-neighbor magnetic exchange of $J = 8$ meV, next-nearest neighbor interaction along the orthorhombic a and b directions of $J_{nna} = J_{nnb} = 0.7$ meV, and an AFM coupling between neighboring layers. The next-nearest neighbor interaction is chosen isotropic, as the twinned crystal used in the $(1\,0\,0)/(0\,1\,0)$ geometry prohibits distinguishing these directions. The need for the additional parameter can be seen when comparing the magnon energies at $\mathbf{q} = (0.25\,0.25\,0)$ and $(0.5\,0\,0)$, which are identical in the model with only nearest-neighbor interaction. The interlayer coupling, $J_c = 0.03$ meV is the only parameter that breaks the tetragonal symmetry in our model aside from the single-ion anisotropy. Note, however, that the crystal structure is orthorhombic, lifting the degeneracy of magnetic interaction parameters. We chose the AFM interaction between the Ru at (0,0,0) and that at (0,0.5,0.5) (in the orthorhombic cell [13]), which stabilizes an A centered magnetic structure with magnetic space group $Pbca$ [16].

The magnetic moment in CRO points along the orthorhombic b direction; see Fig. 1(a). Therefore, one might expect a large gap for the magnetic excitations involving rotations of the moment out of the RuO_2 layers, and much softer in-plane modes. The latter are described by the expectedly small in-plane anisotropy. Following Refs. [26,27] both branches can be described simultaneously with two anisotropy parameters. Surprisingly, in CRO the in-plane anisotropy turned out to be extremely strong. The magnon dispersion starts at 13.04(5) meV, which we may identify with the in-plane gap. There is no magnon branch at lower energy as is clearly shown in the

intensity maps, although there is a weak localized feature observed at 5 meV close to the magnetic zone boundary [23]. As shown in Figs. 2(d) and 3 there is a finite interlayer dispersion visible in the scans taken at $\mathbf{Q} = (0.5\,0.5\,q_l)$ with the second untwinned crystal. The tetragonal [110] direction corresponds to orthorhombic b in the used mounting and thus to the direction of the magnetic moment; therefore, the transverse magnon with in-plane polarization (thus parallel to orthorhombic a) fully contributes. Also, in the other configuration there is a clear difference in spectra taken at $\mathbf{Q} = (0.5\,0.5\,0)$ and $= (1.5\,0.5\,0)$. For the twinned sample we superpose AFM zone centers and zone boundaries, and c polarized magnons will always contribute, while for the in-plane magnon the geometry condition that only magnetic components perpendicular to $\mathbf{Q}$ contribute, suppresses some modes. The fact that we see a clear difference at various $((2n_h + 1)/2\ (2n_k + 1)/2\ n_l)$ unambiguously shows that the modes dispersing between 13.04(5) and 14.2(1) meV possess an in-plane polarization. This furthermore agrees with the Q_l dependence of the signal. We may thus conclude that the lowest magnon branch in CRO possesses an in-plane character and that it disperses between 13.04(5) and 14.2(1) meV along the c direction and up to 41.2 and 37.8 meV along the $(\xi\,\xi\,0)$ and $(\xi\,0\,0)$ paths, respectively. We cannot identify the c polarized modes, as they may remain hidden in the asymmetric shape or even lie at much higher energy. There is some evidence for a nearly flat branch around 36 meV, but we cannot fully rule out that these modes are purely nuclear or that they carry longitudinal polarization. For simplicity, the experimental dispersion is described by an easy-axis anisotropy [27]; see Fig. 3.

The magnon dispersion including its large gap can be very well described within the spin-wave theory, suggesting a conventional local moment $S \sim 1$ magnetism with a strong—but not decisive—impact of SOC. Starting from the other scenario, a spin-orbit driven $j = 0$ singlet nature which is rendered magnetic by
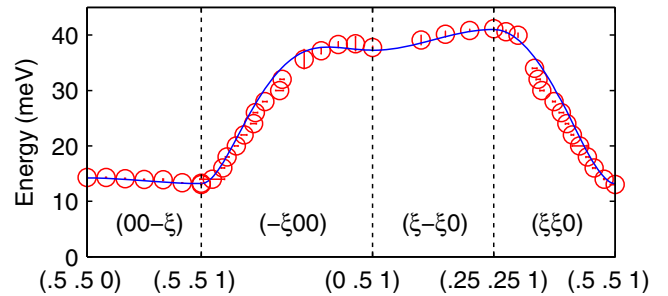

FIG. 3 (color online). Dispersion of the magnon branch along the main symmetry directions at $T = 2$ K. The open symbols indicate the values obtained by fitting the raw data scans with Gaussians or by folding the resolution function with the modeled dispersion. Lines correspond to the spin-wave calculations with the Heisenberg model as described in the text.

noncubic CF and intersite exchange, Akbari and Khaliullin [10] predicted several unusual features of the magnetic excitation spectrum, such as the energy continuously softening from the value λ at Γ, and the presence of extra modes in some part of the spectrum. Our results, however, do not support this model [10]. First, the observed dispersion is much flatter than this prediction, as it does not reach energies of the order of the expectedly large values of λ, and as there is a strong gap. Second, the singlet picture predicts a continuously increasing dispersion near the AFM zone boundaries, while our experiments find the saturation predicted by the Heisenberg model; see Figs. 1 and 2. The Heisenberg scenario also implies several branches: two transversal branches arise from the orthorhombic anisotropy [in-plane and c polarized, see Fig. 1(a)], and longitudinal modes can exist in CRO, which the small ordered moment and the closeness of the MI transition suggest being near the border to itinerancy.

Using the standard description, with the hopping parameters $t \sim 100$ meV, obtained by *ab initio* calculations [28,29], and using the Hubbard's $U \sim 2$ eV, we would obtain for the exchange constant $J = 2t^2/U \sim 10$ meV, in good agreement with our experimental finding. However, CRO is not a strong Mott insulator with completely localized electrons as it is already indicated by the low-lying MI transition. In this case, the basic $j = 0$ ansatz may not be a good starting point, as the $j = 0$ state can be suppressed by electron hopping. Also for Ir^{4+} (specifically for Na_2IrO_3) the sizable hopping modifies the whole picture [30,31], leading to novel quasimolecular orbital states with reduced impact of SOC. The conspicuous but typical absence of $j = 0$ physics in most of the Ru^{4+} materials seems largely connected with the hopping.

Another argument in favor of the applicability of the usual picture of Ru^{4+} ions ($S \sim 1$) is the strong flattening of RuO_6 octahedra [13,15] occurring below the MI transition. Such distortion is typical for the usual Jahn-Teller effect: it stabilizes the electron doubly occupied d_{xy} orbital, leaving two electrons on d_{xz} and d_{yz}. In such a state the orbital moment and spin-orbit interaction are partially quenched. The sign of this distortion proves that in this system the Jahn-Teller effect is stronger than the SOC, which would have caused the opposite distortion and CF splitting [8]. Recent spectroscopy data [21] confirm this significant splitting of t_{2g} orbitals.

On the other hand, the observation of the strong in-plane magnetic gap is remarkable for a layered system. It underlines the relevance of the SOC in CRO even in the conventional scenario. Several Raman scattering experiments observed an additional signal in B_{1g} symmetry appearing in the AFM phase [32–34]. This feature was interpreted as a two-magnon excitation, but our results clearly rule out such explanation. The Raman feature appears at 102 cm^{-1} = 12.6 meV at 10 K, which is much below the energies for two magnon excitations and the

expected peak in the two-magnon density of states (near 80 meV). Instead, this energy is very close to that of the in-plane gap mode in our sample containing 1% of Ti. The single magnon mode, however, is not Raman active in first approximation, demanding further analysis. The temperature dependence and the extreme broadening of the Raman signal at higher temperature agree reasonably well with the corresponding behavior of the magnon gap; see inset in Fig. 4(b).

The magnetic in-plane anisotropy in CRO must originate from SOC and from an orbital arrangement breaking tetragonal symmetry. There have been many experimental and theoretical analyses [17–22] elucidating the change of the orbital polarization upon cooling and the increasing electron occupation of the d_{xy} versus the d_{xz}/d_{yz} orbitals following the flattening of the RuO_6 octahedron. This distortion possesses E_g symmetry, which is the most frequently analyzed in Jahn-Teller models [35]. The t_{2g} orbitals, however, also couple to the T_{2g} octahedron distortions [35] which break tetragonal symmetry in the case of CRO but which were neglected so far. The temperature dependence of the crystal structure of CRO in the insulating phase reveals an ongoing elongation of the RuO_6 octahedra [13,15] along the orthorhombic b direction along which moments align. This distortion corresponds to the T_{2g} "scissor" mode of the free octahedron [35] lifting the d_{xz}/d_{yz} degeneracy. Similar to a tetragonal distortion, e.g., along the z axis, which would stabilize electron orbitals with $l^z = \pm 1$, ($d_{xz} \pm i d_{yz}$), and which, by SOC would orient spins along the z direction, (or a trigonal elongation along [111] (in cubic setting), which would make [111] an easy axis, see, e.g., Ref. [8], such T_{2g} distortion (elongation along the b axis) makes the orthorhombic b direction the easy axis.
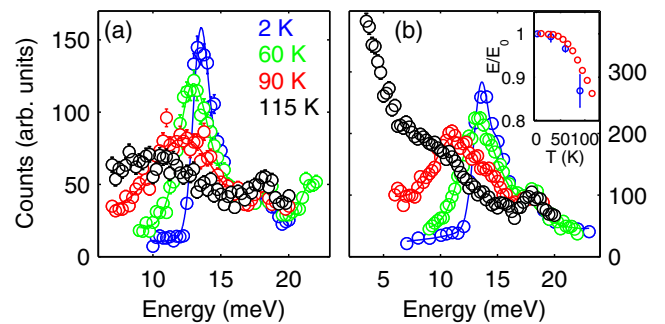
FIG. 4 (color online). Temperature dependence of the magnetic scattering at the AFM zone center (1.5,0.5,0) measured on IN8 with the Si monochromator and $k_F = 1.97$ (a) and 2.662 Å^{-1} (b) The sharp peak associated with the in-plane spin gap mode softens and broadens considerably. The inset shows the energy of the spin gap scaled to its low temperature value (blue) compared to that of a Raman signal taken from Ref. [34] (red). Note that the Raman data were taken on pure Ca_2RuO_4, while our sample contains 1% of Ti.

In conclusion, we have studied the magnon dispersion in CRO, which considerably differs from recent predictions for a $j = 0$ singlet ground state. Instead, the dispersion is well described in a local moment Heisenberg model with strong anisotropy terms yielding a nearest-neighbor exchange interaction of $J = 8$ meV, which agrees with the large calculated hopping integrals. Large hopping seems to be the main cause for the suppression of the $j = 0$ state in Ru^{4+} compounds. On the other hand, the remarkably strong in-plane anisotropy clearly shows that considering tetragonal crystal fields is insufficient. There is important orbital polarization breaking tetragonal symmetry, which is related to the prominent elongation of RuO_6 octahedra along the orthorhombic b direction and which renders spin-orbit coupling still active in this system.

Note added.—After completion of this work we became aware of similar inelastic neutron scattering and theoretical analysis of magnetic excitations in Ca_2RuO_4 [36]. The reported dispersion of the in-plane transverse branch fully agrees with our observations. Jain *et al.* propose a model of an effective $S = 1$ state with strong anisotropy arising from spin-orbit coupling included, which is similar to the interpretation given here.

---

[*]braden@ph2.uni-koeln.de

[1] N. Nagaosa, J. Sinova, S. Onoda, A. H. MacDonald, and N. P. Ong, Rev. Mod. Phys. **82**, 1539 (2010).

[2] A. Shitade, H. Katsura, J. Kunes, X.-L. Qi, S.-C. Zhang, and N. Nagaosa, Phys. Rev. Lett. **102**, 256403 (2009).

[3] M. Z. Hasan and C. L. Kane, Rev. Mod. Phys. **82**, 3045 (2010).

[4] X. L. Xi and S. C. Zhang, Rev. Mod. Phys. **83**, 1057 (2011).

[5] D. Pesin and L. Balents, Nat. Phys. **6**, 376 (2010); W. Witczak-Krempa, G. Chen, Y. B. Kim, and L. Balents, Annu. Rev. Condens. Matter Phys. **5**, 57 (2014).

[6] G. Khaliullin, Phys. Rev. Lett. **111**, 197201 (2013).

[7] A. Abragam and B. Bleaney, *Electron Paramagnetic Resonance of Transition Ions* (Clarendon Press, Oxford, 1970).

[8] D. I. Khomskii, *Transition Metal Compounds* (Cambridge University Press, Cambridge, England, 2014).

[9] G. Cao, T. F. Qi, L. Li, J. Terzic, S. J. Yuan, L. E. DeLong, G. Murthy, and R. K. Kaul, Phys. Rev. Lett. **112**, 056402 (2014).

[10] A. Akbari and G. Khaliullin, Phys. Rev. B **90**, 035137 (2014).

[11] S. Nakatsuji and Y. Maeno, Phys. Rev. Lett. **84**, 2666 (2000); S. Nakatsuji and Y. Maeno, J. Solid State Chem. **156**, 26 (2001).

[12] G. Cao, S. McCall, M. Shepard, J. E. Crow, and R. P. Guertin, Phys. Rev. B **56**, R2916 (1997).

[13] M. Braden, G. André, S. Nakatsuji, and Y. Maeno, Phys. Rev. B **58**, 847 (1998).

[14] C. S. Alexander, G. Cao, V. Dobrosavljevic, S. McCall, J. E. Crow, E. Lochner, and R. P. Guertin, Phys. Rev. B **60**, R8422 (1999).

[15] O. Friedt, M. Braden, G. André, P. Adelmann, S. Nakatsuji, and Y. Maeno, Phys. Rev. B **63**, 174432 (2001).

[16] CRO crystallizes in space group Pbca with lattice constants $a = 5.39$, $b = 5.63$, and $c \approx 12$ Å. We use the tetragonal lattice in space group I4/mmm with $a = b \approx 3.9$ Å and $c \approx 12$ Å in accordance with most publications. Spin-wave calculations were performed in the orthorhombic cell and transformed to the tetragonal one.

[17] T. Mizokawa, L. H. Tjeng, G. A. Sawatzky, G. Ghiringhelli, O. Tjernberg, N. B. Brookes, H. Fukazawa, S. Nakatsuji, and Y. Maeno, Phys. Rev. Lett. **87**, 077202 (2001).

[18] A. Liebsch and H. Ishida, Phys. Rev. Lett. **98**, 216403 (2007).

[19] Z. Fang, N. Nagaosa, and K. Terakura, Phys. Rev. B **69**, 045116 (2004); Z. Fang and K. Terakura, Phys. Rev. B **64**, 020509(R) (2001).

[20] E. Gorelov, M. Karolak, T. O. Wehling, F. Lechermann, A. I. Lichtenstein, and E. Pavarini, Phys. Rev. Lett. **104**, 226401 (2010).

[21] C. G. Fatuzzo, M. Dantz, S. Fatale, P. Olalde-Velasco, N. E. Shaik, B. Dalla Piazza, S. Toth, J. Pelliciari, R. Fittipaldi, A. Vecchione, N. Kikugawa, J. S. Brooks, H. M. Ronnow, M. Grioni, Ch. Rüegg, T. Schmitt, and J. Chang, Phys. Rev. B **91**, 155104 (2015).

[22] V. I. Anisimov, I. A. Nekrasov, D. E. Kondakov, T. M. Rice, and M. Sigrist, Eur. Phys. J. B **25**, 191 (2002).

[23] See Supplemental Material at http://link.aps.org/supplemental/10.1103/PhysRevLett.115.247201 for the experimental details of the INS experiments and concerning the observation of an additional feature at low energy.

[24] A. Zheludev, RESLIB 3.4c (Oak Ridge National Laboratory, Oak Ridge, TN, 2007).

[25] Albert W. Sáenz, Phys. Rev. **125**, 1940 (1962).

[26] M. P. H. Thurlings, E. Frikkee, and H. W. de Wijn, Phys. Rev. B **25**, 4750 (1982).

[27] N. Qureshi, P. Steffens, S. Wurmehl, S. Aswartham, B. Büchner, and M. Braden, Phys. Rev. B **86**, 060410 (2012).

[28] H. Isobe and N. Nagaosa, Phys. Rev. B **90**, 115122 (2014).

[29] O. N. Meetei, W. S. Cole, M. Randeria, and N. Trivedi, Phys. Rev. B **91**, 054412 (2015).

[30] I. I. Mazin, S. Manni, K. Foyevtsova, H. O. Jeschke, P. Gegenwart, and R. Valentí, Phys. Rev. B **88**, 035115 (2013).

[31] K. Foyevtsova, H. O. Jeschke, I. I. Mazin, D. I. Khomskii, and R. Valentí, Phys. Rev. B **88**, 035107 (2013).

[32] C. S. Snow, S. L. Cooper, G. Cao, J. E. Crow, H. Fukazawa, S. Nakatsuji, and Y. Maeno, Phys. Rev. Lett. **89**, 226401 (2002).

[33] J. H. Jung, Solid State Commun. **133**, 103 (2005).

[34] H. Rho, S. L. Cooper, S. Nakatsuji, H. Fukazawa, and Y. Maeno, Phys. Rev. B **71**, 245121 (2005).

[35] I. B. Bersuker, *The Jahn-Teller Effect* (Cambridge University Press, Cambridge, England, 2006).

[36] A. Jain *et al.*, arXiv:1510.07011.

Highly anisotropic magnon dispersion in Ca_2RuO_4: evidence for strong spin orbit coupling
Supplemental information

S. Kunkemöller,[1] D. Khomskii,[1] P. Steffens,[2] A. Piovano,[2] A. Nugroho,[3] and M. Braden[1]

[1]*II. Physikalisches Institut, Universität zu Köln, Zülpicher Str. 77, D-50937 Köln, Germany*
[2]*Institut Laue Langevin, 6 Rue Jules Horowitz BP 156, F-38042 Grenoble CEDEX 9, France*
[3]*Faculty of Mathematics and Natural Sciences, Institut Teknologi Bandung, Jl. Ganesha 10, Bandung 40132, Indonesia*

Ca_2RuO_4 (CRO) single crystals of several $100\,mm^3$ volume containing 1% of Ti were obtained by the traveling solvent floating zone method in a mirror furnace (Canon SC1-MDH11020-CE). The difficulty in the crystal growth consists in passing the first-order metal-insulator transition near 357 K where crystals tend to break apart due to the strong structural strains. We added 1% of Ti as this seems to avoid bursting of the crystal upon cooling below the MI transition. Apparently this non-magnetic substitution sufficiently broadens the transition so that rather large crystals of several $100\,mm^3$ can be obtained at room temperature. These crystals can be cooled to low temperature without any problem. Characterization by magnetic susceptibility and by neutron diffraction experiments indicate a magnetic transition at T_N=112 K and no significant impact of the very small amount of Ti.

Inelastic neutron scattering (INS) experiments were performed with the thermal IN8 and cold THALES triple-axis spectrometers at the Institute Laue Langevin. We used pyrolithic graphite (PG) analyzer crystals that were focused in both directions. Double focusing PG and silicon monochromators were used to define the incoming beam and PG filters to suppress higher harmonics on IN8. Most experiments on IN8 were performed with fixed final momentum of k_f=2.662 Å^{-1} (E_f=14.7 meV); some scans at high energy transfer or aiming at better resolution were performed with k_f=4.1 and k_f=1.97 Å^{-1}, respectively. On IN8 we studied the magnon dispersion in the two scattering geometries (100)/(010) and (110)/(001) in reduced units of the tetragonal lattice, see main text. For both setups two crystals were coaligned. The sample of the second scattering plane was essentially untwinned as determined on the IN3 spectrometer. On THALES the second sample with (110)/(001) geometry was studied with a final k_f=1.5 Å^{-1} (E_f=4.66 meV) using a cooled Be filter to suppress higher-order contaminations. All samples were cooled with a standard ILL-type liquid-helium cryostat.

Besides the dispersing magnon scattering described in the main text, we find weak intensity at an energy transfer of 5 meV appearing near the magnetic zone center $\mathbf{Q}$=(0.5 0.5 0). Results obtained in the IN8 experiment with the first scattering geometry are shown in Fig. 1. This signal is sharp in energy and limited to a small
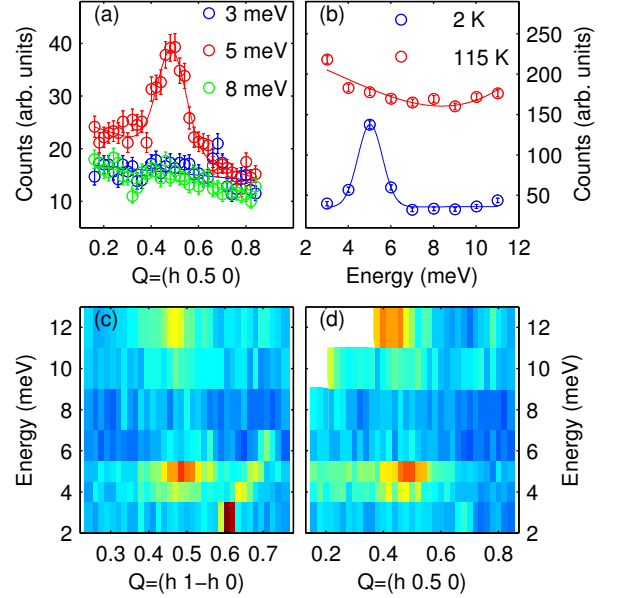
FIG. 1: INS results obtained on IN8 on the low-energy feature appearing near the magnetic zone center $\mathbf{Q}$=(0.5 0.5 0): (a) shows constant energy cuts and (b) constant $\mathbf{Q}$=(0.5 0.5 0) scans. (c) and (d) present scattering maps of energy versus $\mathbf{Q}$; the intensity appearing near $\mathbf{Q}$=(0.66 0.33 0) arises from a higher order contamination and should be ignored.

$\mathbf{Q}$ range near the zone center. The flat constant energy scan at 8 meV excludes that this feature connects with the magnon dispersion at higher energies. Taking into account its lower energy, the scattering strength of the 5 meV feature is considerably weaker. Upon heating above the Néel temperature the sharp signal disappears in an energy scan but strong magnetic scattering persists due to the closing of the magnon gap. In an almost two-dimensional magnetic system strong magnetic correlations remain visible above the Néel temperature. The 5 meV feature was also observed with the THALES spectrometer using cold neutrons, see Fig. 2, confirming in particular its sharp structure in energy and $\mathbf{Q}$ space. In addition it could be shown that this signal is not modulated in c direction, see Fig. 2(b) suggesting zero correlation perpendicular to the layers. The origin of this extra mode cannot be unambiguously clarified. It may arise from the small perturbation implied by the Ti substitu-
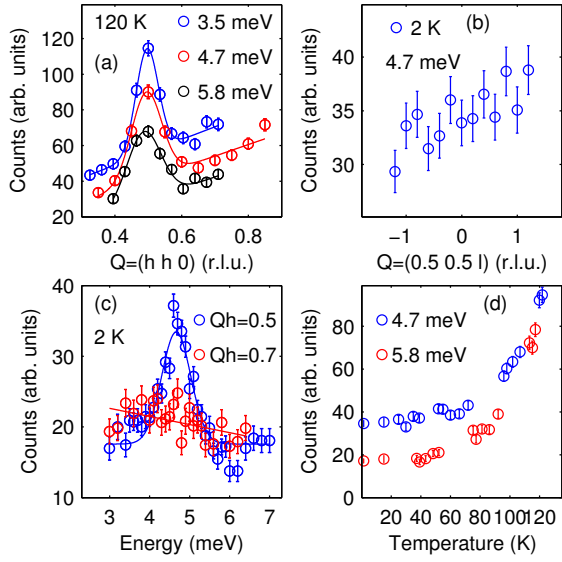
FIG. 2: INS results obtained on THALES on the low-energy feature appearing near the magnetic zone center $\mathbf{Q}=(0.5\,0.5\,0)$: (a) and (b) show constant energy scans along the [110] and [001] directions, respectively; (c) presents energy scans at different $\mathbf{Q}$ values at 2 K and (d) the temperature dependence of the $\mathbf{Q}=(0.5\,0.5\,0)$ signals at 4.7 and 5.8 meV.

tion which will locally modify the orbital arrangement of its neighbors.

CRYSTAL
Research & Technology

Magnetic anisotropy of large floating-zone-grown single-crystals of SrRuO$_3$

S. Kunkemöller[1], F. Sauer[1], A. A. Nugroho[2], and M. Braden[1,]*

SrRuO$_3$ is a highly interesting material due to its anomalous-metal properties related with ferromagnetism and its relevance as conductive perovskite layer or substrate in heterostructure devices. We have used optical floating zone technique in an infrared image furnace to grow large single crystals of SrRuO$_3$ with volumes attaining several hundred mm^3. Crystals obtained for optimized growth parameters exhibit a high ferromagnetic Curie temperature of 165 K and a low-temperature magnetization of 1.6 μ_B at a magnetic field of 6 T. The high quality of the crystals is further documented by large residual resistance ratios of 75 and by crystal structure and chemical analyzes. With these crystals the magnetic anisotropy could be determined.

1 Introduction

SrRuO$_3$ is the infinite-layer material of the Ruddlesden-Popper series of ruthenates Sr$_{n+1}$Ru$_n$O$_{3n}$, which have attracted enormous interest mostly due to the unconventional superconductivity in Sr$_2$RuO$_4$, which is thought to be related to a ferromagnetic instability [1, 2]. In addition to unconventional superconductivity, perovskite ruthenates exhibit metamagnetic transitions, Mott insulating phases, spin-density wave ordering arising from nesting and hidden order phases, to cite the most prominent features [3–6].

SrRuO$_3$ is particularly interesting as it is the only simple material (otherwise one has to study three or higher-number layer members of the Ruddlesden-Popper series) that exhibits ferromagnetic order at ambient conditions [7], which still is a rare phenomenon in the broader class of transition metal oxides. Its ferromagnetism inspired the proposal of p-wave superconductivity mediated through magnetic fluctuations in Sr$_2$RuO$_4$ [1, 2] and it is coupled to the quantum-phenomena associated with the metamagnetic transitions in double and single layered materials [3, 4]. The magnetic moment of

ferromagnetic SrRuO$_3$ amounts to 1.6 μ_B and the ferromagnetic order occurs near 160 K [7]. Ferromagnetism in SrRuO$_3$ is associated with strongly anomalous behavior in various properties: Thermal expansion shows an invar effect in the ferromagnetic phase suggesting a change in the local versus itinerant character of magnetic moments [8, 9]. Furthermore, ferromagnetic correlations clearly interfere with the electronic transport yielding a linear resistivity that breaks the Ioffe rule already at 500 K [10]. Further interest in this material arises from its suitability as a conducting and magnetic layer in various perovskite oxide heterostructures [9]. With the possibility to grow large crystals, SrRuO$_3$ could even be used as a substrate.

In 1959 Randall and Ward reported the first synthesis of polycrystalline SrRuO$_3$ [11]. Single crystals grown by a flux method yield masses in the mg regime [12], but the purity of these SrRuO$_3$ crystals is not comparable with that of other layered ruthenates crystals grown with the floating zone technique [13]. Ikeda et al. reported attempts to grow also SrRuO$_3$ with the floating zone method, but no single crystals could be obtained due to difficulties in stabilizing the floating zone [14]. Very recently Kikugawa et al. reported about the successful growth of single crystals in the floating zone [15].

Here we also present a detailed description of the successful single-crystal growth of SrRuO$_3$ using the optical floating zone technique [16]. The parameters we used for the crystal growth strongly differ from the ones used by Kikugawa et al. [15]. Most importantly, we used more than the double speed for the crystal growth and oxygen content. Therefor crystals with a mass of up to 3 g could be obtained for optimized growth parameters. These crystals were characterized by several microscopic and macroscopic methods. In addition we present

* Corresponding authors: e-mail: braden@ph2.uni-koeln.de, phone: +49 221 470 3655
[1] II. Physikalisches Institut, Universität zu Köln, Zülpicher Straße 77, D-50937 Köln, Germany
[2] Faculty of Mathematics and Natural Science, Institut Teknologi Bandung, Jalan Ganesha 10, 40132 Bandung, Indonesia

Table 1 Summary of various growth parameters and their effect on the single-crystal growth of SrRuO$_3$. The optimized parameters for the crystal growth of SrRuO$_3$ are given in the last row.

parameter	variation	remarks	optimum
Sintering	O$_2$, 1000°C, 12 h	High evaporation of RuO$_2$	Air, 1350°C, 3 h
Feed rod			
RuO$_2$ excess	60 %	327 and 214 phase	90 %
Ø, RuO$_2$ excess	1 cm, 60 %	Crystals with minor quality	0.7 cm, 90 %
Gas flow	1.5 l/min	More RuO$_2$ deposition on the glass tube	4.5 l/min
Atmosphere	100 % O$_2$	No stable molten zone	33 % O$_2$
	40 % O$_2$	Unstable molten zone	
	25 % O$_2$	High melting ruthenium metal phase	
Growth rate	17 mm/h	Small crystallites	15 mm/h
	10 mm/h	327 and 214 phase	
	7 mm/h	214 and 327 phase	

a full structural characterization by several x-ray scattering techniques, which allows us to determine the complex twinning of that perovskite. We also describe detwinning of SrRuO$_3$ crystals, which gives access to the anisotropic magnetic properties.

2 Single-Crystal growth of SrRuO$_3$ in a mirror furnace

2.1 General procedure of the crystal growth of SrRuO$_3$

The parameters to obtain large high quality crystals had to be determined by stepwise variation following a common general procedure. The detailed parameters and their effect on the growth are summarized in table 1. SrCO$_3$ and RuO$_2$ powders both with minimum purity of 99.95 % were mixed with a molar ratio of 1:1.6 or 1:1.9 and homogenized by ball-mixing. A preliminary reaction was performed by heating the powder in a platinum crucible at 1000°C for 24 hours in air with an intermediate grinding. The feed rod was fabricated by pressing the powder in a hydraulic press with a pressure of 1500 kg/cm^2. The resulting rod was sintered for several hours at 1000°C or 1350°C trying different atmospheres. Powder x-ray diffraction (XRD) measurements show that the polycrystalline materials obtained in the preliminary reaction and in the sintered rod consist of a mixture of SrRuO$_3$ and excess RuO$_2$.

For the single-crystal growth an infrared image furnace Canon Machinery Inc. SC1-MDH11020-CE equipped with two 2000 W halogen lamps and a cold trap was used. The atmosphere was varied by mixing argon and oxygen while steadily applying the maximum available total pressure of 10 bar and a gas flow of 1.5 l/min or 4.5 l/min. The crystals were grown with a speed varying between 7 mm/h and 17 mm/h, the speed of the feed rod was set to twice that speed. Both shafts rotated with 15 rpm in opposite directions.

Crystals grown with an optical floating zone technique are usually limited in length by the restrictions of the furnace used, such as the possibility to move the feed and seed rod with respect to the lamps. In contrast, the crystal size of SrRuO$_3$ is essentially limited by the volatility of RuO$_2$. The evaporated material condenses at the glass tube absorbing the incoming light. To compensate for this absorption the power of the lamps has to be continuously enhanced until reaching the maximum power or substantial heating of the glass tube, which can cause serious damage to the furnace. A cold trap is used to absorb the evaporated material, but the trap becomes rapidly saturated. After evaporation of about 2 g of RuO$_2$, we observe that the material is no longer fixed at the cold trap but rapidly covers the glass tube and blocks the heating. Therefore, the growth parameter had also to be optimized with respect to the amount of evaporated RuO$_2$ per volume of single-crystalline material.

2.2 Optimization of growth parameters

For the preparation of the feed rod we tried diameters of 0.7 cm and 1 cm with excess of RuO$_2$ of 60 % and 90 %. With the thicker feed rod an excess of 60 % turned out to be sufficient to get single crystals as the larger diameter slightly reduces the evaporation problem. But the quality of the crystals obtained with this larger diameter was

Cryst. Res. Technol. **51**, No. 4, 299–305 (2016)

CRYSTAL
Research & Technology

Original Paper

significantly below that of those obtained with the thinner diameter. The minor crystalline quality is observed as smeared spots of the Laue images, and the saturation magnetic moment of only 1.55 μ_B and the RRR of 16 are well beyond the values found for the optimized crystals.

The pressure was always set to 10 bar, the highest one applicable to the furnace, since for high pressure less evaporation is expected. Also the rotation speeds of both shafts of 15 rpm were not varied, because they are expected to have little effect on the crystal growth.

The optimum growth speed was found to be 15 mm/h. For the higher speed of 17 mm/h only small single crystalline grains could be obtained even though the molten zone was as stable as in the attempts with optimum speed. In the attempts with lower growth speed, 10 mm/h and 7 mm/h, respectively, the resulting crystals consist of a mixture of $Sr_3Ru_2O_7$ (327) and Sr_2RuO_4 (214) with more Sr_2RuO_4 in the attempt with the lower speed. This shows that more RuO_2 evaporates during the growth processes with slower growth speed, which needs to be compensated by a greater excess of RuO_2 in the feed rod.

The constitution of the atmosphere has strong impact on the stability of the molten zone. For a high oxygen content of 40 % and 100 % it was not possible to keep the molten zone stable for a sufficiently long period to grow single crystalline material. In several attempts with lower oxygen partial pressure (only 25 %) a Ru metal phase formed, and the crystal growth was not stable. The formation of this metallic phase could be suppressed by stopping the motion of the feed rod. This indicates that this phase occurs only in Ru rich floating zones. The O_2 reduced atmosphere suppresses thus the evaporation of RuO_2, however, it is much more difficult to keep the floating zone stable under these conditions. The higher oxygen partial pressure clearly results in larger crystals and makes the crystal growth more reproducible.

With a total gas flow of 1.5 l/min the power of the lamps had to be increased by 6 % during the crystal growth to compensate for the absorption of light by the material deposited on the glass tube. With a higher gas flow of 4.5 l/min electric power had to be increased by only 1 % for the same growth length in order to keep the molten zone stable. Applying a higher gas flow is technically not possible.

3 Chemical and structural analysis of the optimized single crystals

In Figure 1 the single crystalline part of a successful crystal growth can be seen in part a). As-grown
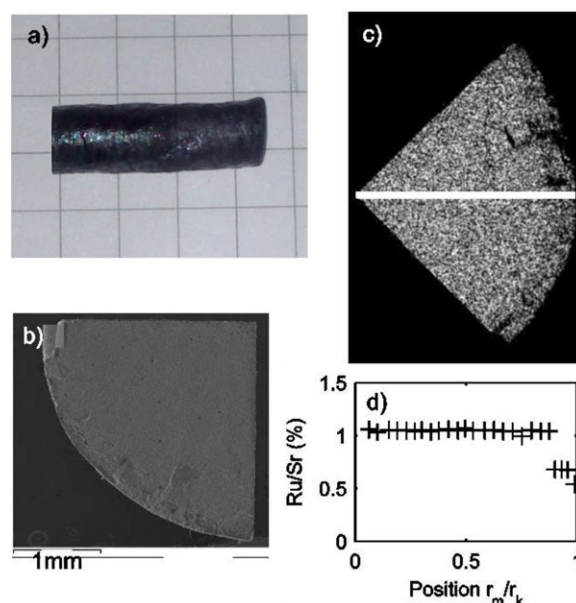
Fig. 1 (a) Single crystalline part of a growth attempt. (b) Electron microscopy picture of a quarter of a slice cut perpendicular to the rod. (c) Mapping of the Ru content with EDX analysis of the piece shown in (b). (d) Ratio of Sr to Ru contents along the white marked path in (c).

crystals have a thick polycrystalline skin. An electron microscopy picture of a quarter of a slice can be seen in b). This piece was further investigated by electron dispersive x-ray spectroscopy (EDX). The obtained mapping of the Ru content can be seen in panel c). This picture reveals an inner bulk part with the correct Ru content and a skin containing less Ru. The white line indicates the positions of EDX measurements, whose results are shown in d) as a function of the distance from the center of the rod, r_m, scaled to the total radius of the crystal, r_k. These EDX results confirm the existence of a bulk $SrRuO_3$ crystal containing the correct amount of Ru covered by a skin with a total volume of about one quarter of the entire cylinder. The skin can be easily removed by filing. The EDX analysis of the bulk yields an average ratio of ruthenium to strontium of 1.044(3). The powder XRD measurements were performed with Cu Kα radiation on crushed single crystals. Rietveld fits were performed with the FulProf Suite [17] in the orthorhombic space group Pnma with the structural data taken from our single crystal XRD measurements, see below. The powder diffraction studies show that the bulk crystals are indeed $SrRuO_3$ with a very small inclusion (~3 %) of a RuO_2 impurity phase (see Figure 2). The position of the strongest RuO_2 peak is marked in the pattern. The expected ratio of ruthenium to strontium for crystals

Fig. 2 XRD powder pattern of a crushed single crystal. The red circles denote the data points, the black line is the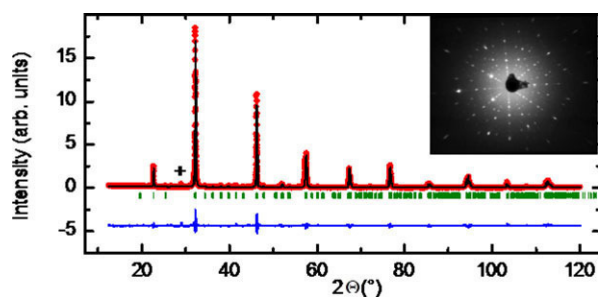 Rietveld fit, the green marks indicate the peak positions according to space group Pnma and the blue line is the difference between the data and the fit. The asterisk marks the position of the strongest RuO_2 peak. The inset shows a Laue image of a single crystal.

Table 2 Crystal structure of $SrRuO_3$ at room temperature. The atomic positions are given in fractions of the unit cell, the atomic displacements are given in Å², values in brackets indicates the error on the last digits.

	Sr	Ru	O_1	$O_2$2
X	0.01676(5)	0	0.4972(3)	0.2769(3)
Y	0.25	0	0.25	0.0273(2)
Z	-0.00256(7)	0,5	0.0544(4)	0.7235(3)
U_{11}	0.00663(14)	0.00147(10)	0.0153(14)	0.0115(8)
U_{22}	0.00455(16)	0.00168(11)	0.0011(11)	0.0077(8)
U_{33}	0.00697(16)	0.00355(11)	0.0067(11)	-0.0019(8)
U_{12}	0	-0.00009(10)	0	-0.0019(6)
U_{13}	-0.00102(13)	0.00030(13)	0.0009(7)	-0.0045(6)
U_{23}	0	0.00009(11)	0	0.0011(6)

including this impurity phase is greater than one which is supported by the EDX analysis. Powder patterns of the skin show a mixture of the layered Strontium Ruthenates, especially the single and double-layered materials. The lattice constants determined by our powder XRD studies are a = 5.5322(1) Å, b = 7.8495(2) Å and c = 5.5730(1) Å in good agreement with previously published neutron powder measurements [18, 19]. Laue images (see inset Figure 2) taken at different positions at the surface of the crystals indicate single crystallinity. For a complete crystal structure determination we used a single crystal X-ray diffractometer X8-APEX by Bruker AXS with a goniometer in kappa-geometry and x-ray radiation from a molybdenum anode. The wavelength was λ = 0.71073 Å and the distance between the sample and the detector was set to 50 mm. The analysis of several crystals shows that even small $SrRuO_3$ crystals with dimensions below 0.1 mm are twinned with non-equal twinning fractions. In the structure refinement the 6 possible orientations of twin domains were taken into account. Structure refinements were carried out using Jana2006 [20]. 20720 observations were merged into 3801 Bragg intensities by averaging only identical and Friedelequivalent reflections. The data were corrected for absorption, and a type I extinction correction was applied during the refinements. A good description of the experimental intensities was achieved yielding weighted reliability-values of Rw = 3.08 % and 3.82 % for the observed (larger than three σ - values) and all reflections, respectively. The goodness of fit value amounts to 1.27 for the observed reflections. The positional and anisotropic displacement parameters from our structure refinements are given in Table 2. Most of the positional parameters agree within the error bars with a previous powder neutron diffraction study [19], just the minor difference of the z

parameter of the O_1 site seems to arise from the refinement of isotropic displacement parameters in the powder study. Note, that the precision of the parameters is significantly higher in our single-crystal analysis, even for the light O sites. The refinement of the occupation of the strontium to ruthenium ratio yields 1.0009(12) indicating perfect stoichiometry of the crystals obtained with the optimized growth conditions.

The crystal structure of $SrRuO_3$ (see Figure 3) differs from the ideal cubic perovskite structure by a rotation of the RuO_6-octahedra around the b-axis (long axis in space group Pnma), combined with a tilt [18, 22]. Here, the corresponding angles are called "rotation angle" and "tilt angle", respectively. The rotation angle and the tilt angle are not defined unambiguously since the octahedra are slightly distorted. In order to determine the rotation angle φ, the atom O_2 is projected onto the ac-plane and a Ru – Ru − O_2' angle is measured yielding φ = 6.10(3) °. The tilting angle can be measured via the displacement of the apical oxygen O_1, Θ_{ap} = 8.79(5) ° and via the tilt of the basal plane, Θ_{bas} = 8.72(5) °. The space group Pnma also allows for a deformation of the RuO_6 octahedron which can be associated with orbital polarization of ferro- or antiferro-orbital type [22]. In $SrRuO_3$ there is no significant splitting of the two Ru - O_2 distances of 1.9858 Å and 1.9859 Å, also the Ru-O_1 distance is almost identic, but the basal plane of the octahedron is distorted, the distance of the octahedron edge length along a O_2 - O_{2a} = 2.782 Å is significantly smaller than that along c O_2 - O_{2c} = 2.835 Å. A qualitatively similar but

Cryst. Res. Technol. **51**, No. 4, 299–305 (2016)
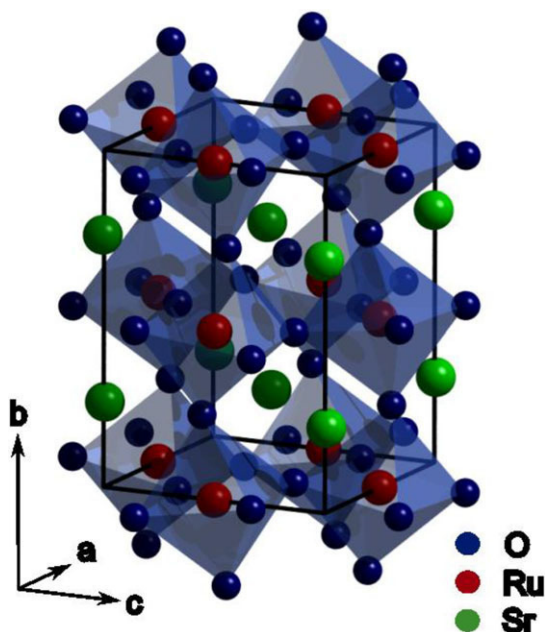
CRYSTAL
Research & Technology

Fig. 3 Drawing of the crystal structure of $SrRuO_3$ as obtained by the single-crystal X-ray diffraction experiment at room temperature, see table 1.

much larger splitting is observed in insulating Ca_2RuO_4 [23]. This deformation is related with the fact that the lattice is shorter along the tilt axis, which contrasts with a rigid picture, but which is observed in many transition-metal oxides [22].

4 Characterization of physical properties

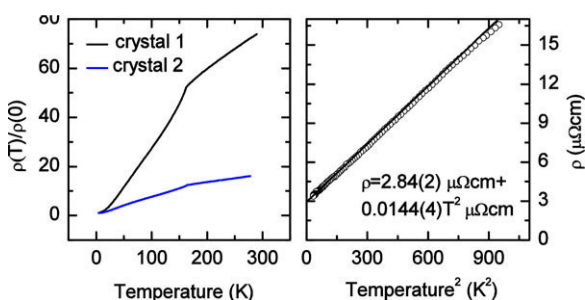Resistivity measurements on our crystals are presented in Figure 4. In a) the temperature dependent resistiv-

Fig. 4 (a) Temperature dependent resistivity divided by the residual resistivity. The black and blue lines correspond to the measurements on a crystal with optimized and non-optimized growth conditions, respectively. (b) Resistivity plotted against the squared temperature for the crystal with optimized growth parameters. The black line is a linear fit of the data between 5 K and 10 K
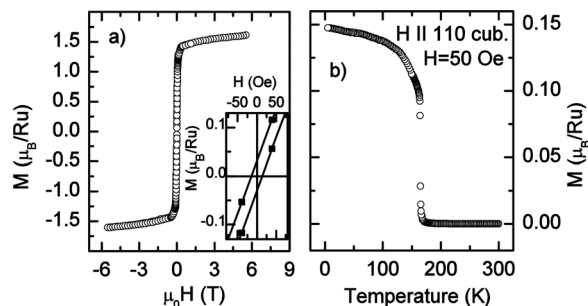

Fig. 5 Magnetic characterization. The magnetic field is applied along a pseudo cubic [110] direction. (a) Magnetization curve measured at 5 K. The inset shows the coercive field of only 14 Oe. (b) Temperature dependent magnetization measured upon cooling in 50 Oe. The magnetic phase transition occurs at 165 K.

ity divided by the low-temperature residual resistivity measured with a standard four-point method between 5 K and room temperature is shown.

The results are in good agreement with the data presented in reference [21]; in particular we find the clear kink in the resistivity at the ferromagnetic phase transition. The residual resistivity ratio obtained for the crystal grown under optimized conditions amounts to 75, and is thus larger than that in the cleanest $SrRuO_3$ films [24]. Furthermore, the residual resistivity of $\rho_0 = 3$ $\mu\Omega$cm is less than half of the value observed in flux grown single crystals [12]. In contrast a crystal grown with non-optimum conditions (feed rod diameter 1 cm, RuO_2 excess 60 %) exhibits a much lower residual resistivity ratio, although a high ferromagnetic T_c is clearly visible. In b) the specific resistivity is plotted against the squared temperature, and the data between 5 K and 10 K are fitted with a linear function indicating Fermi liquid behavior. From this fit the residual resistivity and the A coefficient were determined: $\rho = \rho_0 + A \cdot T^2$ with $A = 0.0144(4)$ $\mu\Omega$ cm/K^2 and $\rho_0 = 2.84(2)$ $\mu\Omega$ cm. Note that the errors do not include uncertainties in the geometry. Magnetization measurements (Figure 5) were performed with a commercial SQUID Magnetometer (Quantum Design) and show the same characteristics of the ferromagnetic order as the data from reference [7]. The magnetization loop in a) is measured at 5 K with the field applied along a pseudocubic [110] direction (note that our crystals are twinned). The magnetic moment does not saturate in the applied field of 6 T and reaches values of 1.6 μ_B. The coercive field amounts only to 14(2) Oe. The ferromagnetic phase transition occurs at 165 K as it can be seen in panel b), which shows the temperature dependent magnetization measured in a magnetic field of 50 Oe applied along a pseudocubic [110] direction measured on

Original Paper

cooling. Kikugawa et al. report a lower magnetic quality, a maximum magnetic moment of about 1.4 μ_B in a magnetic field of 7 T and a coercive field of 40 Oe [15] most likely because of mixing of various directions.

5 Anisotropic magnetic properties

In order to detwin the crystals uniaxial pressure of 1.5 kg/mm^2 were applied on a rectangular crystal on a cubic (110) face heated to 730°C and furnace cooled to room temperature. With the single-crystal x-ray diffractometer several unique reflexions (e.g. (850)) for the twins were measured in reflection geometry confirming the successful and complete detwinning of the crystal.

Magnetic hysteresis loops recorded at 5K are shown in Fig. 6 for magnetic fields applied along the three orthorhombic axes, which are accessible with the untwinned crystal. There is little anisotropy between the orthorhombic a and c axes although these lattice constants and the O$_2$-O$_2$ octahedron edges differ considerably. In contrast, the magnetization along the **b** direction is strongly reduced. The fact that anisotropy persists to large fields is remarkable and points to strong spin-orbit coupling in SrRuO$_3$. Along the **b** direction magnetization rapidly increases to ∼0.5 μ_B but then grows with a small field slope. This behavior indicates that the directions parallel to the O-O edges of the RuO6 octahedron are softer than those along the bonds. A first principles study should be able to shed further light on this issue. The magnetic anisotropy reported by Kikugawa et al. [15] is much smaller than what we observe, most likely due to twinning, and an early study [25] finds qualitatively a similar anisotropy but with ∼30\% smaller saturation magnetization most likely due to lower quality of flux-grown samples.
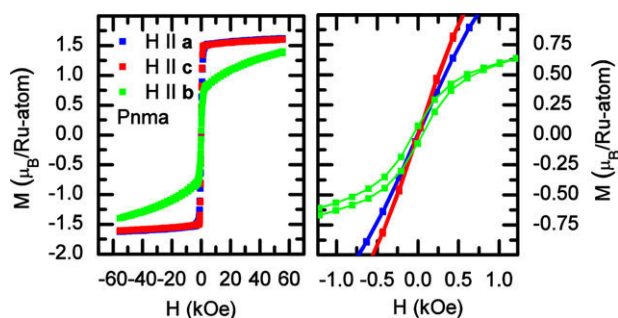

Fig. 6 Magnetic anisotropy. (a) Magnetization curves measured at 5 K. The magnetic field is applied along the three principal symmetry directions. (b) A zoom into panel (a).

6 Conclusion

We present the crystal growth of large SrRuO$_3$ single crystals with the optical floating zone technique. Crystals with a mass of up to 3 g (several hundred mm^3 volume) could be obtained. The residual resistivity ratio and the small coercive field as well as chemical analyzes denote the high purity of the crystals. The single-crystal XRD analysis confirms the ideal stoichiometry of these crystals and reveals that even sub-mm sized crystals exhibit complex twinning with six possible domain orientations. The magnetic anisotropy of untwinned crystals is shown.

References

[1] Y. Maeno, H. Hashimoto, K. Yoshida, S. Nishizaki, T. Fujita, J. G. Bednorz, F. Lichtenberg, Nature (London) **372**, 532–534 (1994).

[2] T. M. Rice, M. Sigrist, J. Phys.: Cond. Matter **7**, L643–L648 (1995)

[3] R. S. Perry, L. M. Galvin, S. A. Grigera, L. Capogna, A. J. Schofield, A. P. Mackenzie, M. Chiao, S. R. Julian, S. I. Ikeda, S. Nakatsuji, Y. Maeno, C. Pfleiderer, Phys. Rev. Lett. **86**, 2661–2664 (2001).

[4] S. Nakatsuji, D. Hall, L. Balicas, Z. Fisk, K. Sugahara, M. Yoshioka, Y. Maeno, Phys. Rev. Lett. **90**, 137202 (2003).

[5] S. Nakatsuji, T. Ando, Z. Mao, Y. Maeno, Physica B **259–261**, 949–950 (1999).

[6] M. Braden, O. Friedt, Y. Sidis, P. Bourges, M. Minakata, Y. Maeno, Phys. Rev. Lett. **88**, 197002 (2002).

[7] A. Kanbayasi, Journal of the J. Phys. Soc. Jpn. **41**, 1876–1878 (1976).

[8] T. Kiyama, K. Yoshimura, K. Kosuge, Y. Ikeda, Y. Bando, Phys. Rev. B **54**, R756–R759 (1996).

[9] G. Koster, L. Klein, W. Siemons, G. Rijnders, J. S. Dodge, C.-B. Eom, D. H. A. Blank, M. R. Beasley, Rev. Mod. Phys. **84**, 253–298 (2012).

[10] L. Klein, J. S. Dodge, C. H. Ahn, G. J. Snyder, T. H. Geballe, M. R. Beasley, A. Kapitulnik, Phys. Rev. Lett. **77**, 2774–2777 (1996).

[11] J. J. Randall, R. Ward, J. Am. Chem. Soc. **81**, 2629–2631 (1959).

[12] R. Bouchard, J. Gillson, Mater. Res. Bull. **7**, 873–878 (1972).

[13] L. Capogna, A. P. Mackenzie, R. S. Perry, S. A. Grigera, L. M. Galvin, P. Raychaudhuri, A. J. Schofield, C.

S. Alexander, G. Cao, S. R. Julian, Y. Maeno, Phys. Rev. Lett. **88**, 076602 (2002).

[14] S. I. Ikeda, U. Azuma, N. Shirakawa, Y. Nishihara, Y. Maeno, J. Cryst. Growth **237–239**, 787–791 (2002).

[15] N. Kikugawa, R. Baumbach, J. S. Brooks, T. Terashima, S. Uji, Y. Maeno, Cryst. Growth Des. **15**, 5573–5577 (2015)

[16] H. A. Dabkowska and A. B. Dabkowski, Springer Handbook of Crystal Growth, G. Dhanaraj, K. Byrappa, V. Prasad, M. Dudley, Springer Verlag, Berlin Heidelberg (2010).

[17] J. Rodríguez-Carvajal, Physica B **192**, 55–69 (1993).

[18] C. W. Jones, P. D. Battle, P. Lightfoot, W. T. A. Harrison, Acta Crystallogr. **45**, 365–367 (1989).

[19] S. N. Bushmeleva, V. Yu. Pomjakushin, E. V. Pomjakushina, D. V. Sheptyakov, A. M. Balagurov, J Magn. Magn. Mater. **305**, 491–496 (2006).

[20] V. Petříček, M. Dušek, L. Palatinus, Z. Kristallogr. **229**, 345–352 (2004)

[21] P. B. Allen, H. Berger, O. Chauvet, L. Forro, T. Jarlborg, A. Junod, B. Revaz, G. Santi, Phys. Rev. B **53**, 4393–4398 (1996).

[22] M. Cwik, T. Lorenz, J. Baier, R. Müller, G. André, F. Bourée, F. Lichtenberg, A. Freimuth, R. Schmitz, E. Müller-Hartmann, M. Braden, Phys. Rev. B **68**, 060401(R) (2003)

[23] M. Braden, G. André, S. Nakatsuji, Y. Maeno, Phys. Rev. B **58**, 847 (1998).

[24] A. P. Mackenzie, J. W. Reiner, A. W. Tyler, L. M. Galvin, S. R. Julian, M. R. Beasley, T. H. Geballe, A. Kapitulnik, Phys. Rev. B **58**, R13318–R13321 (1998).

[25] G. Cao, S. McCall, M. Shepard, J. E. Crow, Phys. Rev B **56**, 321–329 (1997)

Absence of a Large Superconductivity-Induced Gap in Magnetic Fluctuations of Sr$_2$RuO$_4$

S. Kunkemöller,[1] P. Steffens,[2] P. Link,[3] Y. Sidis,[4] Z. Q. Mao,[5,6] Y. Maeno,[5] and M. Braden[1,*]

[1]*II. Physikalisches Institut, Universität zu Köln, Zülpicher Straße 77, D-50937 Köln, Germany*
[2]*Institut Laue Langevin, 71 avenue des Martyrs, 38000 Grenoble, France*
[3]*Heinz Maier-Leibnitz Zentrum, Technische Universität München, Lichtenbergstrasse 1, 85748 Garching, Germany*
[4]*Laboratoire Léon Brillouin, C.E.A./C.N.R.S., F-91191 Gif-sur-Yvette CEDEX, France*
[5]*Department of Physics, Graduate School of Science, Kyoto University, Kyoto 606-8502, Japan*
[6]*Department of Physics, Tulane University, New Orleans, Louisiana 70118, USA*

Inelastic neutron scattering experiments on Sr$_2$RuO$_4$ determine the spectral weight of the nesting induced magnetic fluctuations across the superconducting transition. There is no observable change at the superconducting transition down to an energy of ∼0.35 meV, which is well below the 2Δ values reported in several tunneling experiments. At this and higher energies magnetic fluctuations clearly persist in the superconducting state. Only at energies below ∼0.3 meV can evidence for partial suppression of spectral weight in the superconducting state be observed. This strongly suggests that the one-dimensional bands with the associated nesting fluctuations do not form the active, highly gapped bands in the superconducting pairing in Sr$_2$RuO$_4$.

Sr$_2$RuO$_4$ is one of the best studied unconventional superconductors [1–5] but its pairing symmetry and mechanism still remain a subject of very active debate. There is newly added evidence in favor of the most advocated symmetry of the superconducting order, namely, the spin-triplet chiral p-wave symmetry, such as the increase in the Knight shift expected in the equal-spin-pairing triplet state [6], observation of the surface density of states consistent with the chiral edge state [7], and the magnetization steps corresponding to the half-quantum fluxoids [8]. On the other hand, there are results challenging the p-wave pairing scenario, such as the strong limiting of the in-plane upper critical fields [9], the first-order superconducting transition [10,11], and the absence of the chiral edge current [12]. At present, there seems to be no symmetry model that can explain all the experimental facts available. If the most advocated symmetry of the superconducting order is correct, Sr$_2$RuO$_4$ is a topological superconductor proposed as a promising candidate for quantum computing [13,14].

Another prominent feature of Sr$_2$RuO$_4$ is that its normal state is quantitatively well characterized as a quasitwo-dimensional (Q2D) Fermi liquid [2,3]. The Fermi surface consists of three cylindrical sheets [2]: two originate from the d_{xz} and d_{yz} orbitals, called the α and β bands, and retain a quasione-dimensional (Q1D) character as well; the other one from the d_{xy}, called the γ band, shows a Q2D character. All three bands disperse weakly along the interlayer c direction [15]. In such a multiband system with distinct orbital symmetries, superconductivity may be strongly orbital dependent [16]. The strong nesting between the Q1D bands results in strongly enhanced spin-density wave (SDW) fluctuations [17–22] and even minor chemical

substitution leads to static ordering of this SDW instability with the moment along the c direction. Only 2.5% of Ti induces this SDW phase [23,24], and recent muSR experiments and neutron scattering studies show that the same magnetic order occurs upon replacing Sr with isovalent Ca [25,26]. Such spin fluctuations originating from the nesting of the Q1D Fermi surface sheets cannot easily lead to the most likely chiral superconducting state [2]. The equal-spin p-wave pairing scenario is based on quasiferromagnetic correlations associated with the γ band, and amongst the various p-wave possibilities a chiral (and topological) state, $k_x + ik_y$, was proposed to explain various experiments [2,3]. Evidence for strong quasiferromagnetic fluctuations can be found in susceptibility [2,3] and nuclear magnetic resonance (NMR) measurements [27], but a thorough study of such fluctuations is still lacking. Thus, one important step toward resolving the apparent controversy is to identify which of the bands are mainly responsible for the superconductivity.

Many attempts were made to reconcile the discrepancy between the pairing symmetry and the apparently dominant magnetic fluctuations [2,3,5]. Treating the on-site Coulomb repulsion within perturbation theory corroborates the scenario of p-wave pairing mainly arising in the Q2D band [28]. This scenario is challenged by Raghu *et al.*, who apply renormalization group techniques and discuss orbital and charge fluctuations in the Q1D bands as the main ingredient [29]. These calculations were extended by Scaffidi *et al.* [30] to include interband and spin-orbit coupling yielding similar sized gaps on all bands without tuning of parameters. In contrast the recent analysis by Huo *et al.* argues in favor of superconductivity arising in the

Q2D bands with the nesting fluctuations perturbing the superconductivity [31]. Experimentally, the observation of a strong enhancement of the superconducting T_c (by a factor 2!) under both tensile and compressive strain [32] may suggest a dominant influence of the van Hove singularity in the Q2D bands associated with the ferromagnetic instability. The question of which bands drive superconductivity in Sr_2RuO_4 remains as open and fascinating as ever [33].

Inelastic neutron scattering (INS) can yield valuable information concerning the role of the different bands in the pairing [31]. If superconductivity directly arises from the Q1D bands as active bands, which thus exhibit a large gap, there must be a clear impact on the associated incommensurate magnetic excitations. Several calculations explicitly predict the occurrence of a resonance mode in at least one of the spin excitation channels for p-wave superconducting symmetry [31,34–36]. On the other hand, if superconductivity is mainly driven by the Q2D band associated with ferromagnetic fluctuations, a lower gap in the Q1D bands and only a small impact on the magnetic fluctuations is expected [16,31]. Here we report INS experiments across the superconducting transition in Sr_2RuO_4, which clearly show that nesting-induced magnetic fluctuations only sense a very small gap suggesting that the Q1D bands are not the active ones in the superconducting pairing.

The difficulty of INS experiments on the magnetic response in the superconducting state of Sr_2RuO_4 consists in the weakness of the signal combined with the high resolution needed. The INS intensity is given by the imaginary part of the generalized susceptibility, $\chi''(\mathbf{Q}, E)$, multiplied by the Bose factor [19],

$$\frac{d^2\sigma}{d\Omega dE} = \frac{k_f r_0^2 F^2(Q)}{k_i \pi (g\mu_B)^2} \frac{2\chi''(\mathbf{Q}, E)}{1 - \exp(-E/k_b T)}, \quad (1)$$

where we ignore the spin anisotropy of the magnetic susceptibility [21] [k_i and k_f denote incoming and final neutron momentum, $F(Q)$ denotes the magnetic form factor of Ru at the scattering vector, and $r_0^2 = 0.29 \times 10^{-28}$ m^2]. The nesting-induced magnetic excitations at $\mathbf{q}_{\text{inc}}$ follow a single relaxor behavior [18,19,21,22],

$$\chi''(\mathbf{q}_{\text{inc}}, E) = \chi'(\mathbf{q}_{\text{inc}}, 0) \frac{\Gamma E}{\Gamma^2 + E^2}, \quad (2)$$

which is maximum at the characteristic energy Γ and almost linear for much lower energies. INS experiments in the normal state indicate strong magnetic scattering at the nesting vector, $\mathbf{q}_{\text{inc}}$, with the characteristic energy decreasing towards low temperatures. But this softening stops at $\Gamma \sim 6$ meV, which is well above the values of the superconducting gap [18,19,21]. Therefore, the INS signal in the range, where one may expect an impact of the superconducting gap, is very small. In addition, the experiment requires a high energy-resolution in order to study this region close to the strong

elastic response, which considerably reduces the INS intensity. Because of these difficulties the previous INS experiments on Sr_2RuO_4 in the superconducting phase yielded reliable statistics on the nesting fluctuations only for energy transfer above ~ 1 meV [19].

INS experiments were carried out on the PANDA triple-axis spectrometer at the Forschungsreaktor Munich II and at the recently upgraded THALES instrument at the Institut Laue Langevin. In all experiments we used an assembly of 12 Sr_2RuO_4 crystals with a total volume of 2.2 cm^3. The crystals were grown at Kyoto University using a floating-zone image furnace and similar crystals were studied in many different experiments [2,3]. We choose the $[100]/[010]$ scattering geometry, because this yields the best INS signal due to the integration along the vertical direction along c where little modulation of magnetic response is expected. For all experiments the crystal assembly was cooled with a dilution refrigerator attaining minimum temperature of the order of ~ 50 mK. There is some impact on the neutron absorption on the sample temperature of the order of 10 mK, which, however, is negligible compared to the transition temperature. On PANDA we mostly used a final momentum of $k_f = 1.2$ Å^{-1} to obtain sufficient resolution and pyrolitic graphite (PG) (002) as monochromator and analyzer. In order to decrease the background a BeO filter was put in front of the analyzer and a Be filter between the monochromator and sample. On THALES a much better intensity to background ratio was achieved, but some residual background at low energies remained when using PG (002) monochromator and analyzer crystals (PG-PG configuration) even for rather small values of the final momentum. In order to further suppress this low-energy background we included a radial collimator and a Be filter in front of the analyzer and we used a Si (111) monochromator (SI-PG configuration). We applied vertical and horizontal focusing at both the monochromator and analyzer. In addition, a velocity selector in front of the monochromator was inserted to suppress higher order contaminations. Most scans on THALES were performed with a fixed final momentum of $k_f = 1.57$ Å^{-1} where the Be filter effectively cuts all neutrons with only slightly larger final energy. Some scans were performed by scattering at the sample and at the analyzer in the same sense (U configuration), which reduces the background as the detector is positioned farther away from the direct beam, but slightly worsens the resolution.

In spite of serious efforts the measurements on PANDA considerably suffered from the background scattering. Scans at the scattering vectors of (0.3,0.3,0) and (0.7,0.7,0.4) did not yield any indication for a superconductivity-induced change at T_c above $E \sim 0.6$ meV but the achieved statistics at lower energy remained insufficient to characterize the weak magnetic signal. In the following we therefore focus on the results obtained on THALES, which exhibit significantly better statistics.
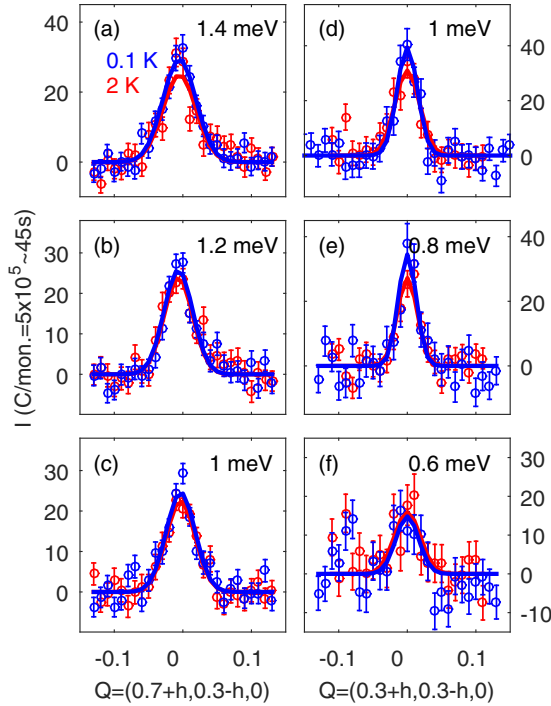
FIG. 1.   Constant-energy scans obtained on THALES with $k_f = 1.57$ Å^{-1} using the PG-PG configuration. Intensity profiles were fitted by the sum of a Gaussian peak and a curved background, which was assumed identical at both temperatures and subtracted from the data.

FIG. 2.   [(a)–(d)] Constant-energy scans obtained on THALES with $k_f = 1.57$ Å^{-1} using the Si-PG configuration. A flat background was subtracted from the data. [(e) and (f)] Inelastic rocking scans using the Si-PG configuration. The sample was rotated through the (0.3,0.3,0) $E = 0.4$ and 0.325 meV positions at the center of the scans yielding a flat background that was subtracted from the data.

Figures 1 and 2 show constant-energy scans for temperatures above and below the superconducting transition. The data in Fig. 1 were taken with the PG-PG configuration on THALES (energy resolution at the elastic line $\Delta E_0 = 0.20$ meV full width at half maximum) and those in Fig. 2 with the SI-PG configuration, which yields a lower background at small energies and improves the resolution ($\Delta E_0 = 0.12$ meV) but considerably reduces the signal. With the dilution refrigerator cryostat used in these experiments, it is not possible to obtain sufficient temperature stability in the range of 1.2 to 1.6 K; therefore, we could not follow the signals close to T_c. The data shown in Figs. 1 and 2 unambiguously show that the nesting related fluctuations in the energy range 0.6 to 1 meV can be easily studied by our INS experiment and that this signal is not affected by the superconducting transition concerning either the intensity or the width. We have studied the nesting signal at the two scattering vectors $\mathbf{Q} = (0.3, 0.3, 0)$, see Fig. 1(d)–1(f) and Fig. 2(c)–2(f), and $\mathbf{Q} = (0.7, 0.3, 0)$, see Fig. 1(a)–1(c) and Fig. 2(a)–2(b), which are not equivalent due to the centering of the body centered lattice in Sr$_2$RuO$_4$ and due to the lower form factor at the latter reducing the magnetic signal. Because of the quasitwo-dimensional nature of the magnetic correlations in Sr$_2$RuO$_4$, however, one does not expect an essential difference, and the signal at both scattering vectors is comparable; in particular, there is no change at the

superconducting transition, $T_c = 1.4$ K, for energies above 0.6 meV at both $\mathbf{Q}$ values.

Experiments at lower energy transfer are more difficult as described above. Since the background depends on the length of the scattering vector (i.e., the scattering angle), it is not constant in a straight transversal constant-energy scan like those shown in Figs. 1 and 2(a)–2(d) but may peak at the scan center. Therefore, we performed inelastic rocking scans by turning the sample with fixed $|\mathbf{Q}|$; see Figs. 2(e) and 2(f). These scans posses a flat background and clearly confirm that magnetic scattering persists in the superconducting state essentially unchanged down to energies of the order of 0.325 meV. Note that the Bose factor explains a small intensity reduction between 2 and 0.1 K of 1.18 and 1.11 at $E = 0.325$ and 0.4 meV, respectively, so that the data do not yield any significant reduction of spectral weight even at 0.325 meV.

Figure 3 resumes the energy dependence of the magnetic nesting signal. Figure 3(a) shows the fitted peak heights of the constant-E scans taken in different configurations at the two scattering vectors. In order to compare data taken at different $\mathbf{Q}$ positions, in different configurations (scattering sense at the analyzer) and in different runs, intensities are normalized to the values at 1 meV and 2 K. The peak

FIG. 3.   (a) Fitted Gaussian peak heights obtained from the constant-E scans taken with the two configurations at the two scattering vectors. In order to allow for compari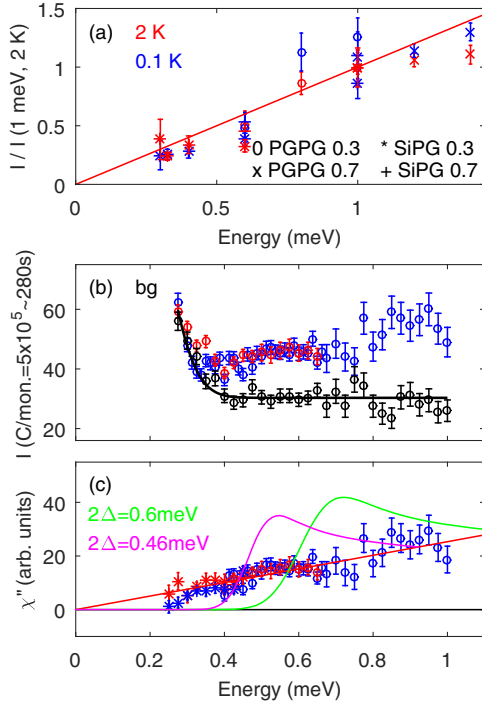son, the data were normalized to the values at 1 meV and 2 K and a correction for the Bose factor was applied. (b) Constant-Q scans obtained with $k_f = 1.57$ Å^{-1} using the Si-PG configuration. Red and blue symbols denote the data taken at $\mathbf{Q} = (0.3, 0.3, 0)$ above and below the superconducting transition, respectively, and black symbols denote background intensity observed at a $\mathbf{Q}$ vector of the same length but rotated by 16° with respect to the $\mathbf{Q}$ position of the nesting response. (c) Magnetic signal at $\mathbf{Q} = (0.3, 0.3, 0)$ obtained by subtracting the background signal and by correcting for the Bose factor. Straight lines in (a) and (c) denote the linear relation $\chi'' \propto E$ expected for the single relaxor at low energy; see Eq. (2). The magenta and green lines in (c) correspond to the calculated magnetic response in the case of active Q1D bands [31], which results in a resonance excitation at the energy of twice the superconducting gap taken at the weak coupling BCS value 0.46 meV and at the value observed in tunneling experiments (0.6 meV; see the text). The theoretical result was folded with the experimental resolution. Data in (b) and part of the data in (c) (circles) were taken in U configuration yielding lower background at energies above 0.4 meV and slightly reduced energy resolution, $\Delta E_0 = 0.16$ meV, while the low-energy part of (c) was recorded in Z configuration (stars) in a dedicated experiment. In this Z configuration the background remains flat and a better statistics could be reached resulting in much smaller error bars.

heights at larger energies remain unchanged upon entering the superconducting state while evidence for partial suppression of spectral weight is observed below ~0.3 meV. Figure 3(b) shows constant Q scans taken at the nesting scattering vector (0.3,0.3,0) above and below the superconducting transition as well as a background scan taken at

a scattering vector of the same length but rotated 16 degrees away from the nesting position. Subtracting this background signal from that obtained at the nesting $\mathbf{Q}$ position we can deduce the magnetic signal at both temperatures; see Fig. 3(c). This analysis shows that the nesting scattering remains essentially unchanged for energies above ~0.325 meV. The constant Q scan data yield weak evidence for partial suppression of spectral weight due to the opening of the superconducting gap only at very low energies, see Fig. 3(c), but additional studies are desirable.

The magnetic response of an itinerant system corresponds to a particle-hole excitation, which in a superconductor must cross twice the superconducting gap, 2Δ. There have been several reports on the superconducting gap in Sr_2RuO_4 [7,17,37–39]: The first tunneling experiments were interpreted as evidence for very large gap and $2\Delta/k_BT_c$ values [37,38] while more recent studies conclusively suggest smaller values: Suderov *et al.*, $2\Delta = 0.56$ meV [39]; Kashiwara *et al.*, $2\Delta = 0.93$ meV [7]; and Firmo *et al.*, $2\Delta = 0.7$ meV slightly above the weak coupling Bardeen Cooper Schrieffer (BCS) theory value $2\Delta = 0.46$ meV. None of the tunneling studies can safely identify the band carrying the largest gap, leaving the discussion about active and passive bands open. On the theoretical side, different studies arrive at nearly the same conclusion that opening the p-wave gap in the Q1D sheets results in a full suppression of spectral weight below $2\Delta_{1d}$ and even a resonance enhancement at or close to this value [12,34–36]. In Fig. 3(c) we include the calculation for a superconducting gap opening in the Q1D bands of 0.46 and 0.6 meV [31] folded with the experimental resolution. Our results clearly contradict such a picture. A resonance enhancement of the magnetic response in the superconducting state has been reported in several unconventional superconductors [40]. In particular, in superconductors in which the pairing appears mediated by well-defined magnetic fluctuations such as the cuprates or the FeAs-based compounds, strong resonance modes are found [40]. Such a behavior can be excluded for the nesting scattering in Sr_2RuO_4, which exhibits no significant suppression of magnetic weight at energies well below the maximum 2Δ reported in the tunneling experiments or the weak coupling BCS value. It seems therefore very unlikely that the Q1D bands are the active ones for the superconducting pairing in Sr_2RuO_4. Instead the ferromagnetic fluctuations arising from the large density of states in the Q2D bands can imply superconductivity primordially in the Q2D bands. This scenario is supported by the field-orientation dependence of the specific heat [41,42] and NMR data [2,3,5,33], and direct evidence for ferromagnetic fluctuations can be obtained from magnetization [2,3] and polarized INS studies [43].

Nodes of the gap function may lead to persisting magnetic scattering in the superconducting state for energies below the maximum values of 2Δ. But in the scenario of Q1D bands being the active ones for the superconducting

pairing mediated by nesting-induced fluctuations, some effect of the gap opening must be observed. The fact that there is no change in the magnetic scattering (below 20% for $E > 0.325$ meV) well below the observed maximum values of 2Δ [7,17,37–39] renders such a scenario very unlikely.

In conclusion we have studied the low-energy magnetic fluctuations associated with the nesting of Q1D bands in Sr_2RuO_4. The fact that we do not observe a significant change in this signal when passing the superconducting transition disagrees with a scenario of nesting-related fluctuations driving superconductivity primordially in the Q1D bands.

---

[*]braden@ph2.uni-koeln.de

[1] Y. Maeno, H. Hashimoto, K. Yoshida, S. Nishizaki, T. Fujita, J. G. Bednorz, and F. Lichtenberg, Nature (London) **372**, 532 (1994).

[2] A. P. Mackenzie and Y. Maeno, Rev. Mod. Phys. **75**, 657 (2003).

[3] Y. Maeno, S. Kittaka, T. Nomura, S. Yonezawa, and K. Ishida, J. Phys. Soc. Jpn. **81**, 011009 (2012).

[4] Y. Liu and Z.-Q. Mao, Physica (Amsterdam) **514C**, 339 (2015).

[5] C. Kallin and A. Berlinsky, Rep. Prog. Phys. **79**, 054502 (2016).

[6] K. Ishida, M. Manago, T. Yamanaka, H. Fukazawa, Z. Q. Mao, Y. Maeno, and K. Miyake, Phys. Rev. B **92**, 100502(R) (2015).

[7] S. Kashiwaya, H. Kashiwaya, H. Kambara, T. Furuta, H. Yaguchi, Y. Tanaka, and Y. Maeno, Phys. Rev. Lett. **107**, 077003 (2011).

[8] J. Jang, D. G. Ferguson, V. Vakaryuk, R. Budakin, S. B. Chung, P. M. Golbart, and Y. Maeno, Science **331**, 186 (2011).

[9] C. Rastovski, C. D. Dewhurst, W. J. Gannon, D. C. Peets, H. Takatsu, Y. Maeno, M. Ichioka, K. Machida, and M. R. Eskildsen, Phys. Rev. Lett. **111**, 087003 (2013).

[10] S. Yonezawa, T. Kajikawa, and Y. Maeno, Phys. Rev. Lett. **110**, 077003 (2013).

[11] S. Kittaka, A. Kasahara, T. Sakakibara, D. Shibata, S. Yonezawa, Y. Maeno, K. Tenya, and K. Machida, Phys. Rev. B **90**, 220502(R) (2014).

[12] C. W. Hicks, J. R. Kirtley, T. M. Lippman, N. C. Koshnick, M. E. Huber, Y. Maeno, W. M. Yuhasz, M. B. Maple, and K. A. Moler, Phys. Rev. B **81**, 214501 (2010).

[13] D. A. Ivanov, Phys. Rev. Lett. **86**, 268 (2001).

[14] C. Nayak, S. H. Simon, A. Stern, M. Freedman, and S. D. Sarma, Rev. Mod. Phys. **80**, 1083 (2008).

[15] C. N. Veenstra, Z.-H. Zhu, M. Raichle, B. M. Ludbrook, A. Nicolaou, B. Slomski, G. Landolt, S. Kittaka, Y. Maeno, J. H. Dil, I. S. Elfimov, M. W. Haverkort, and A. Damascelli, Phys. Rev. Lett. **112**, 127002 (2014).

[16] D. F. Agterberg, T. M. Rice, and M. Sigrist, Phys. Rev. Lett. **78**, 3374 (1997).

[17] I. A. Firmo, S. Lederer, C. Lupien, A. P. Mackenzie, J. C. Davis, and S. A. Kivelson, Phys. Rev. B **88**, 134521 (2013).

[18] Y. Sidis, M. Braden, P. Bourges, B. Hennion, S. NishiZaki, Y. Maeno, and Y. Mori, Phys. Rev. Lett. **83**, 3320 (1999).

[19] M. Braden, Y. Sidis, P. Bourges, P. Pfeuty, J. Kulda, Z. Mao, and Y. Maeno, Phys. Rev. B **66**, 064522 (2002).

[20] F. Servant, B. Fak, S. Raymond, J. P. Brison, P. Lejay, and J. Flouquet, Phys. Rev. B **65**, 184511 (2002).

[21] M. Braden, P. Steffens, Y. Sidis, J. Kulda, P. Bourges, S. Hayden, N. Kikugawa, and Y. Maeno, Phys. Rev. Lett. **92**, 097402 (2004).

[22] K. Iida, M. Kofu, N. Katayama, J. Lee, R. Kajimoto, Y. Inamura, M. Nakamura, M. Arai, Y. Yoshida, M. Fujita, K. Yamada, and S.-H. Lee, Phys. Rev. B **84**, 060402(R) (2011).

[23] M. Minakata and Y. Maeno, Phys. Rev. B **63**, 180504(R) (2001).

[24] M. Braden, O. Friedt, Y. Sidis, P. Bourges, M. Minakata, and Y. Maeno, Phys. Rev. Lett. **88**, 197002 (2002).

[25] J. P. Carlo, T. Goko, I. M. Gat-Malureanu, P. L. Russo, A. T. Savici, A. A. Aczel, G. J. MacDougall, J. A. Rodriguez, T. J. Williams, G. M. Luke, C. R. Wiebe, Y. Yoshida, S. Nakatsuji, Y. Maeno, T. Taniguchi, and Y. J. Uemura, Nat. Mater. **11**, 323 (2012).

[26] S. Kunkemöller, A. A. Nugroho, Y. Sidis, and M. Braden, Phys. Rev. B **89**, 045119 (2014).

[27] K. Ishida, H. Mukuda, Y. Minami, Y. Kitaoka, Z. Q. Mao, H. Fukazawa, and Y. Maeno, Phys. Rev. B **64**, 100501 (2001).

[28] Y. Yanase, T. Jujo, T. Nomura, H. Ikeda, T. Hotta, and K. Yamada, Phys. Rep. **387**, 1 (2003).

[29] S. Raghu, A. Kapitulnik, and S. A. Kivelson, Phys. Rev. Lett. **105**, 136401 (2010).

[30] T. Scaffidi, J. C. Romers, and S. H. Simon, Phys. Rev. B **89**, 220510(R) (2014).

[31] J. W. Huo, T. M. Rice, and F.-C. Zhang, Phys. Rev. Lett. **110**, 167003 (2013).

[32] C. W. Hicks, D. O. Brodsky, E. A. Yelland, A. S. Gibbs, J. A. N. Bruin, M. E. Barber, S. D. Edkins, K. N. Nishimura, S. Yonezawa, Y. Maeno, and A. P. Mackenzie, Science **344**, 283 (2014).

[33] C. Kallin, Rep. Prog. Phys. **75**, 042501 (2012).

[34] H.-Y. Kee, J. Phys. Condens. Matter **12**, 2279 (2000).

[35] D. K. Morr, P. F. Trautman, and M. J. Graf, Phys. Rev. Lett. **86**, 5978 (2001).

[36] M. Yakiyama and Y. Hasegawa, Phys. Rev. B **67**, 014512 (2003).

[37] F. Laube, G. Goll, H. v. Löhneysen, M. Fogelström, and F. Lichtenberg, Phys. Rev. Lett. **84**, 1595 (2000).

[38] M. D. Upward, L. P. Kouwenhoven, A. F. Morpurgo, N. Kikugawa, Z. Q. Mao, and Y. Maeno, Phys. Rev. B **65**, 220512(R) (2002).

[39] H. Suderow, V. Crespo, I. Guillamon, S. Vieira, F. Servant, P. Lejay, J. P. Brison, and J. Flouquet, New J. Phys. **11**, 093004 (2009).

[40] D. J. Scalapino, Rev. Mod. Phys. **84**, 1383 (2012).

[41] K. Deguchi, Z. Q. Mao, H. Yaguchi, and Y. Maeno, Phys. Rev. Lett. **92**, 047002 (2004).

[42] K. Deguchi, Z. Q. Mao, H. Yaguchi, and Y. Maeno, Phys. Soc. Jpn. **73**, 1313 (2004).

[43] M. Braden, P. Steffens, Y. Sidis, J. Kulda, P. Bourges, S. Hayden, N. Kikugawa, and Y. Maeno, Phys. Rev. Lett. **92**, 097402 (2004).

Magnon dispersion in Ca$_2$Ru$_{1-x}$Ti$_x$O$_4$: Impact of spin-orbit coupling and oxygen moments

S. Kunkemöller,[1] E. Komleva,[2] S. V. Streltsov,[2,3] S. Hoffmann,[1] D. I. Khomskii,[1] P. Steffens,[4]
Y. Sidis,[5] K. Schmalzl,[6] and M. Braden[1,*]

[1]*II. Physikalisches Institut, Universität zu Köln, Zülpicher Str. 77, D-50937 Köln, Germany*
[2]*Ural Federal University, Mira Street 19, 620002 Ekaterinburg, Russia*
[3]*M. N. Miheev Institute of Metal Physics of Ural Branch of Russian Academy of Sciences, 620137 Ekaterinburg, Russia*
[4]*Institut Laue Langevin, 6 Rue Jules Horowitz BP 156, F-38042 Grenoble CEDEX 9, France*
[5]*Laboratoire Léon Brillouin, C.E.A./C.N.R.S., F-91191 Gif-sur-Yvette CEDEX, France*
[6]*Jülich Centre for Neutron Science JCNS, Forschungszentrum Jülich GmbH, Outstation at ILL, 38042 Grenoble, France*

The magnon dispersion of Ca$_2$RuO$_4$ has been studied by polarized and unpolarized neutron scattering experiments on crystals containing 0, 1, and 10% of Ti. Ti is inserted in order to enable the growth of large, partially detwinned crystals. One percent of Ti has a negligible impact on structural and magnetic properties. Also for 10% Ti content magnetic properties still change very little, but the insulating phase is stabilized up to at least 700 K and structural distortions are reduced. The full dispersion of transverse magnons studied for 1% Ti substitution can be well described by a conventional spin-wave model with interaction and anisotropy parameters that agree with density functional theory calculations. Spin-orbit coupling strongly influences the magnetic excitations, as it is most visible in large energies of the magnetic zone-center modes arising from magnetic anisotropy. Additional modes appear at low energy near the antiferromagnetic zone center and can be explained by a sizable magnetic moment of 0.11 Bohr magnetons, which the density functional theory calculations find located on the apical oxygens. The energy and the signal strength of the additional branch are well described by taking into account this oxygen moment with weak ferromagnetic coupling to the Ru moments.

I. INTRODUCTION

Ca$_2$RuO$_4$ (CRO) is the Mott insulating [1] end member of the series Ca$_{2-x}$Sr$_x$RuO$_4$, which possesses a rich diversity of structural, magnetic, and transport properties [2–5]. Sr$_2$RuO$_4$, the other end member, is proposed to be a spin-triplet superconductor with broken time-reversal symmetry [6–9]. The metal-insulator transition in CRO goes along with severe structural distortions [3,10], in particular a flattening of the RuO$_6$ octahedron, that increase until the onset of antiferromagnetic order [11]. The nowadays widely used picture assumes that an orbital ordering is associated with the structural changes [12–14]. The 4d_{xy} orbitals become doubly occupied and the 4$d_{xz,yz}$ singly occupied resulting in flattened octahedrons and a $S = 1$ state. In the past the nature of the Mott transition of this multiband system with four d electrons on the Ru site was intensively discussed [12,15–20]. Recently, it was proposed that spin-orbit coupling (SOC) in this 4d system is strong enough to change the multiplet structure and couples S and L to j resulting in a nonmagetic $j = 0$ ground state. The occurrence of magnetic order was proposed to be of a singlet-magnetism type (see, e.g., Sec. 5.5. in Ref. [21]), which was called excitonic magnetism in Ref. [22], and a special type of magnon dispersion was predicted in this theory [23]. The main branches of the dispersion obtained by inelastic neutron scattering (INS) experiments, however, could be successfully described with a conventional Heisenberg model [24,25] and disagree with the $j = 0$ calculations [23]. Nevertheless, neutron scattering experiments revealed features such as an upward dispersion beyond the zone boundary

[25] and additional magnetic scattering not describable with a simple square-lattice antiferromagnet. The main in-plane transverse modes exhibit a large anisotropy gap, underlining the impact of broken tetragonal symmetry in combination with SOC. Furthermore, additional signals were detected in the neutron scattering experiments at low and at high energies [24,25] that cannot be explained by the two transverse magnon branches.

The crystal growth of insulating CRO is severely hampered by the metal-insulator transition occurring in pure CRO at $T_{MIT} = 360$ K [3,10]. The space group does not change at this first-order phase transition, but there are sizable jumps in the lattice parameters, in particular for c, with $\Delta c \sim 0.2$ Å [3]. Therefore, the crystals tend to crack upon cooling after the growth process, and only small pieces of mm^3 size can be recovered. We circumvented this problem by introducing Ti that seems to broaden the metal-insulator transition.

The paper is arranged as follows. We first show that only for 10% of Ti there are significant changes of physical properties, see Sec. III A. This large substitution considerably stabilizes the insulating phase and suppresses structural distortions, but magnetic properties are nearly identical to those in pure CRO. Therefore, the results on the magnon dispersion discussed in Sec. III B that were obtained from polarized and unpolarized INS experiments on 1% Ti substituted CRO can be taken as representative for the pure material. In addition we performed density functional theory (DFT) calculations that may well reproduce the rather peculiar magnon dispersion. The DFT calculations also reveal a sizable ordered moment located on the apical oxygens, which explains the occurrence of an additional low-energy branch. The magnon dispersion in CRO thus reveals a very strong impact of SOC and of oxygen magnetic moments.

———————
*braden@ph2.uni-koeln.de

II. EXPERIMENTAL

Because INS experiments require samples of ~cm^3 size, we substituted a small amount of Ru by Ti in order to cool the crystals through the metal-insulator transition without breaking them into small pieces. Crystals with a mass of 0.5 g to 1 g were obtained with only 1% Ti substitution. We were also able to obtain two larger pieces of pure CRO, one with a mass of 0.45 g and one with 0.3 g, but these crystals possess a bad mosaic spread of 5°, which most likely is the reason why they were not destroyed upon cooling. Nevertheless, these crystals are suitable for some INS studies.

The $Ca_2Ru_xTi_{1-x}O_4$ crystals with $x = 0, 1$, and 10% used in this neutron scattering study (labeled 0Ti, 1Ti, 10Ti, respectively) were grown by the floating-zone method in a Canon Machinery Inc. SC1-MDH11020-CE furnace equipped with two 2000 W halogen lamps and a cold trap following the procedure described in Refs. [26,27]. $CaCO_3$, RuO_2, and TiO_2 were mixed in stoichiometric ratios and a Ru excess of 32% was added. The powder was mixed and reacted for 24 h with an intermediate grinding. Then a rod was pressed and sintered at 1350 °C. A growth speed of 17 mm/h and a feed-rod speed of 20 mm/h were used and the atmosphere contained 90% Ar and 10% O at a total pressure of 9 bar. Phase purity was checked by x-ray powder diffraction from crushed parts of the single crystals, which indicates no impurity phases. The lattice constants at room temperature were obtained by LeBail fits of these powder pattern using the FullProf Suite [28]. Single-crystal x-ray diffraction experiments were performed on a Bruker X8 Apex diffractometer equipped with a charge-coupled-device detector. Details of this structure determination and a detailed list of the refined parameters can be found in Appendix A. Magnetization measurements were performed with a superconducting quantum interference device (SQUID) magnetometer from Quantum Design, and the resistivity was measured with a standard four-point method. Spin wave calculations were performed using SpinW [29].

Elastic and inelastic neutron scattering experiments were performed with the cold triple-axis spectrometer (TAS) 4F1 at the LLB, with the thermal TAS IN3 at the ILL and with the polarized thermal TAS IN22 at the ILL. The polarized neutron scattering experiments were performed using Heusler (111) monochromator and analyzer crystals. A PG filter was inserted on the scattered beam before the neutron-spin flipper and the monitor was put on the incoming beam between monochromator and sample. A set of Helmholtz coils was used to produce the guide field and the sample was zero field cooled (less than 2 G) in an orange-type cryostat. A mounting of three crystals with a total mass of 2.5 g containing 1% Ti (1Ti) was used for the polarized neutron scattering experiment. The sample was twinned with nonequal twinning fractions of 2.5:1 determined by scanning the orthorhombic (200) and (020) reflections. The a,b plane [see Fig. 1(a)] was chosen as the scattering plane in order to efficiently integrate the inelastic signal along the vertical direction, where the resolution is poor. We used the standard coordinate system in polarized neutron scattering [30]. **x** is parallel to the scattering vector (**Q**); **y** and **z** are perpendicular to **Q**. While **y** is in the scattering plane, **z** is perpendicular to it. Therefore, **y** lies in the a,b plane of the crystal and **z** parallel to the c axis. In
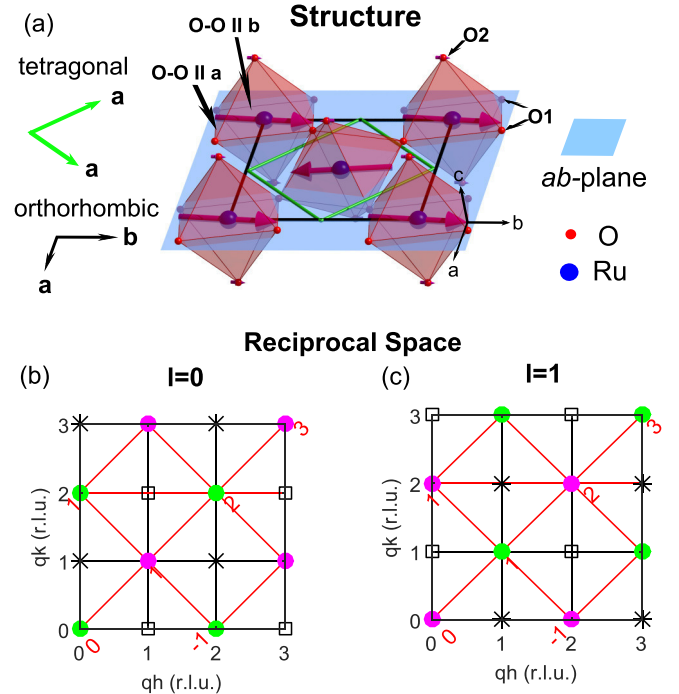

FIG. 1. Crystal and magnetic structure of CRO and the associated reciprocal space. In (a) one layer of the crystal and magnetic structure is shown. The Ru (blue balls) sit in octahedrons of oxygen (red balls). The ab-plane is indicated in light blue. In black and green the orthorhombic and tetragonal cells are shown. The pink arrows denote the magnetic moments on the Ru and O sites. At the tip of the low right Ru moment, the directions of the different polarizations of the magnon modes are indicated by black arrows and some labellings of atoms and atom distances are given. In (b,c) the (hkl) planes in reciprocal space are illustrated for $l = 0$ and $l = 1$, respectively. The orthorhombic and tetragonal cells are drawn in black and red, respectively. Green circles denote tetragonal zone centers and pink circles zone boundaries. Black squares (stars) mark antiferromagnetic zone centers of the A- (B-) centered antiferromagnetic order.

neutron scattering only magnetic moments perpendicular to **Q** intervene. Therefore, the magnetic scattering intensities sense a geometry factor $\sin^2(\alpha)$ with α being the angle between **Q** and the magnetic moment, which corresponds to either the static ordering moment in diffraction or to the oscillating moment in a magnon. With longitudinal neutron polarization six different channels can be analyzed: three spin-flip (SF) and three non-spin-flip (nSF) channels. While phonons always contribute to the nSF channel there is an additional selection rule for magnetic scattering. The magnetic component parallel to the direction of the neutron polarization contributes to the nSF channel, while the components perpendicular to the neutron polarization generate SF scattering. By combining this polarization rule with the geometry factor one can distinguish the different magnetic components. In the geometry we use for the polarized neutron scattering experiment we see the c polarized modes in the SFy channel and they do not loose intensity due to the geometry factor, because the scattering vector is always parallel to the a,b plane and thus perpendicular to c. In contrast the SFz channel contains the in-plane modes, the transverse and longitudinal ones, but weighted with the

geometry factor. For example at $\mathbf{Q} = (2,1,0)$ the geometry factor for the transverse mode (a polarized) is $\sin^2(\alpha) = 0.2$ and that for the longitudinal mode (b polarized) $\sin^2(\alpha) = 0.8$. At $\mathbf{Q} = (1,2,0)$ this ratio is inverted [see Figs. 1(b) and 1(c)]. Respecting the twinning ratio of 2.5:1, we expect that the intensities at $\mathbf{Q} = (2,1,0)$ and $\mathbf{Q} = (1,2,0)$ have a ratio of 0.6 for the transverse mode. For the longitudinal mode this ratio is inverted. Thus, it is possible to distinguish between transverse modes and longitudinal modes by comparing scattering at properly chosen $\mathbf{Q}$. Because the polarization of the neutron beam is not perfect, one has to correct the intensities for the finite flipping ratio (FR) [30,31]. Thereby, the magnetic signals are obtained from the intensities of the different SF channels corrected for the FR:

$$I(M_{y,z}) = \frac{FR+1}{FR-1}[I(SF_x) - I(SF_{y,z})]. \tag{1}$$

The FR of our experiment on IN22 amounts to 12, which is determined by comparing the signals of rocking scans on the (200) Bragg reflection in the SF and nSF channels.

On the cold TAS 4F1 crystals with different Ti content were used, 0Ti and 10Ti. 0Ti has a mass of 0.45 g and a twinning ratio of 1:1 and 10Ti a mass of 0.93 g and a twinning ratio of 9:1. The scattering plane for both samples was chosen to be the [010]/[001] plane, so the scattering plane for the other twin domains was the [100]/[001] plane. For all 4F1 scans a pyrolytic graphite monochromator and analyzer were used, a cooled Be filter was put on k_f to suppress higher order contaminations. For the cooling of the samples an orange-type cryostat was used and k_f was set to 1.55 Å^{-1} for all scans.

With the IN3 TAS we analyzed the magnetic order of the crystal containing 1% Ti used in the previous neutron scattering study [24] (1TiB). This crystal was found to exhibit a majority twin domain of 95% and the experiment was performed in the [010]/[001] orientation used in the INS experiment.

III. RESULTS AND DISCUSSION

A. Impact of Ti substitution on structural, magnetic, and electronic properties of Ca$_2$Ru$_{1-x}$Ti$_x$O$_4$

1. Crystal structure of Ca$_2$Ru$_{1-x}$Ti$_x$O$_4$

The crystal structure of CRO [11] is similar to the structure of Sr$_2$RuO$_4$ of K$_2$NiF$_4$ type [32], where the Ru atoms sit in oxygen-octahedron cages, which are corner shared in the a,b plane. In CRO the octahedrons are rotated and tilted and they also become severely distorted. As a consequence, the tetragonal symmetry of Sr$_2$RuO$_4$ is reduced to the orthorhombic space group $Pbca$ [11]. One layer of the crystal structure is drawn in Fig. 1, which also depicts the magnetic order with antiferromagnetic moments on Ru pointing along b. The orthorhombic unit cell is rotated by 45° with respect to the tetragonal one and enhanced to: $\mathbf{a}_{\mathrm{orth}} = \mathbf{a}_{\mathrm{tet}} + \mathbf{b}_{\mathrm{tet}}$, $\mathbf{b}_{\mathrm{orth}} = \mathbf{a}_{\mathrm{tet}} - \mathbf{b}_{\mathrm{tet}}$, $a_{\mathrm{orth}} \sim b_{\mathrm{orth}} \sim \sqrt{2}a_{\mathrm{tet}}$. Unless otherwise specified all notations refer to the orthorhombic lattice of the majority twin orientation. Our crystals usually possess two twin orientations, which are obtained by interchanging the a_{orth} and b_{orth} directions.
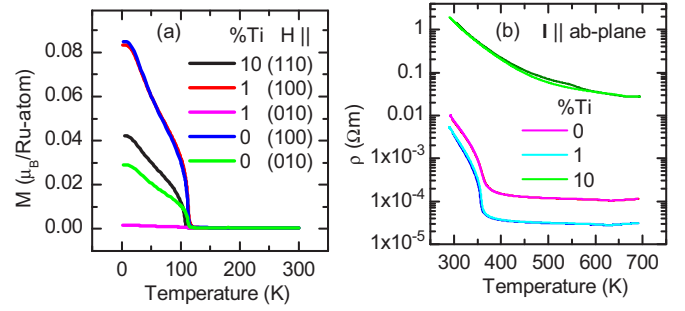

FIG. 2. Temperature dependence of physical properties of CRO with different Ti content. (a) Field-cooled magnetization curves in 0.1 T measured on heating. (b) Resistivity on heating in dark color and on cooling in bright color. Only the 10% Ti curves do not coincide.

All crystals were examined by x-ray diffraction, magnetization, and resistivity measurements in addition to the neutron scattering experiments described below. Figure 2 shows the magnetization and electric resistance data of the three Ti concentrations. The temperature of the metal-insulator transition is 4 K lower for the sample containing 1% Ti than for the pure compound. The sample containing 10% Ti does not show indications for a phase transition upon cooling down to 80 K where the experimental limit of the increasing resistivity is reached. The absolute values of the resistivity curves have a large uncertainty because of the first-order structural phase transition. There the crystals tend to crack, which prohibits the current to flow through the hole sample. This effect has been frequently observed during a single measurement cycle. The resistivity is enhanced by a multiplication factor after passing the structural transition. As the samples have already passed this transition after the crystal growth, there are some cracks inside the sample, which is evident from measuring several pieces of the same crystal without obtaining the same room-temperature specific resistivity.

The magnetic and insulating properties in Ca$_{2-x}$Sr$_x$RuO$_4$ are closely related to the crystal structure [3]. CRO is heavily distorted with respect to Sr$_2$RuO$_4$, which possesses the ideal structure of K$_2$NiF$_4$ type without structural distortions, but which already is close to such a structural instability [33–35]. In the layered ruthenates the distortions can be described as octahedron rotation around the c direction and tilting around an in-plane axis. These distortions and the associated structural phase transitions result from bond-length mismatch, and the distortions in CRO are induced by the chemical substitution of Sr by the isovalent but smaller Ca, which is not able to fill the space between the oxygen octahedrons like Sr does. So the octahedrons start to rotate and tilt in order to reduce the coordination volume around Ca. By chemically substituting the smaller Ti for Ru, one expects a small decrease of these deformations, which is indeed realized. The tilt and rotation angles of 10Ti are significantly smaller than the values determined in the samples containing only 0 and 1% Ti, see Appendix A, Table II.

Most interesting is the impact of the Ti doping on the deformation of the RuO$_6$ octahedron, which is a fingerprint of the lifting of orbital degeneracy [3,11,12]. The structural change at the metal-insulator transition in pure CRO is
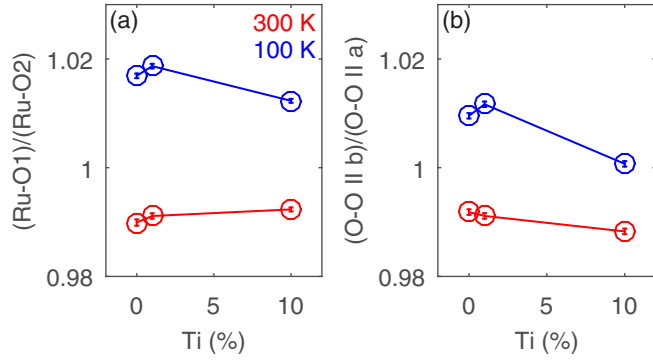
FIG. 3. Temperature and Ti doping dependence of the RuO$_6$ octahedron distortion obtained by single crystal x-ray diffraction analyses; (a,b) presents the ratios of in-plane to out-of-plane RuO bond distances (flattening) and of the two octahedron edges parallel to b and a, respectively. Both entities are enhanced in the insulating phase at low temperature due to the lifting of orbital degeneracy.

characterized by a jump of the c lattice constant and by a flattening of the octahedron as it is visible in the Ru-O bond distance ratio [3]. Upon cooling into the insulating phase this octahedron flattening continues until it saturates at the antiferromagnetic phase transition. Slightly below room temperature the octahedron shape passes from elongated to flattened [3]. In all samples studied here, this crossover occurs below room temperature, thus at 100 K the octahedron shape is flattened for all Ti substitutions, see Fig. 3. Due to flattening of the octahedron the d_{xy} orbital shifts down in energy compared to the d_{xz}, d_{yz} orbitals. A similarly strong and anomalous temperature dependence is also observed for the ratio of the two O-O octahedron edge lengths parallel a and b which is related to the orthorhombic splitting [$\epsilon = (b - a)/(a + b)$] [3]. At room temperature the octahedron is longer along a, while it is elongated along b at low temperature. All these effects can be attributed to a temperature dependent orbital ordering [3,11,13,24]. The considerable elongation along b at low temperature agrees with SOC and the alignment of the magnetic moment mainly along the b direction [24]. Figure 3 illustrates that these two distortions of the RuO$_6$ octahedron become suppressed by the 10% Ti substitution. This underlines the orbital ordering character of these distortions, which is obviously suppressed by Ti^{4+} with an empty 3d shell.

While the a,b plane (or the average in-plane parameter) increases with high Ti content, the c lattice constant decreases at room temperature. The reduction of the c lattice constant, in hand with an increase of the a,b plane, is the structural signature of the insulating state of CRO. With 1% of Ti substitution there is only a small decrease in T_{MIT} (Fig. 2), but with 10% of Ti substitution there are drastic effects. In the resistivity of 10Ti there are no indications for a sharp metal-insulator transition on cooling from 700 down to 80 K, where the upper experimental limit of the resistance experiment is reached. Note that the absolute values of the resistivity curves are prone to a large uncertainty because of the first order structural phase transition which causes cracks in the crystals. But the orders of magnitude larger resistivity of the 10Ti sample and the absence of the metal-insulator transition is unambiguous. This remarkable stabilization of the insulating

state by only small amounts of Ti substitution is also seen in Ca$_3$Ru$_2$O$_7$ [36]. Since the ionic radii of Ti and Ru are very similar, this suppression of the metallic state seems to originate from the very effective suppression of the hopping. The Ti does not contribute states near the Fermi level in metallic ruthenates [36], so that the hopping becomes disrupted. Also in Sr$_2$RuO$_4$ Ti substitution has a strong impact: It stabilizes spin-density wave ordering associated with the Fermi-surface nesting of the pure material for only 2.5% Ti [37]. Furthermore, Ti substitution also stabilizes a spin-density wave magnetic instability in Sr$_3$Ru$_2$O$_7$ [38]. On the other hand Ti substitution yields little impact on the insulating low-temperature state in CRO as visible in the little changes of magnetic properties induced by 10% Ti concentration.

2. Magnetic structure of Ca$_2$Ru$_x$Ti$_{1-x}$O$_4$

The magnetic structure of 1Ti was studied on IN22 with polarization analysis. The analysis of the magnetic structure of 1TiB on IN3 is described in Appendix B. Scans along the (200) and (020) reflections (Fig. 4) reveal that crystal 1Ti exhibits both twin-domain orientations in the ratio 2.5:1. Figures 4(c)–4(f) show the SF intensities in the three channels for scans across the (100), (010), (120), and ($\bar{1}$20) magnetic reflections for crystal 1Ti. The magnetic structure of CRO has been previously determined by neutron powder diffraction [11]. As illustrated in Fig. 1(a) the magnetic moments are essentially aligned along the b direction (corresponding to the tilt axis) with antiferromagnetic alignment between nearest neighbors. The moments are canted along a yielding a net ferromagnetic moment in a single layer. There are two different magnetic structures reported for CRO [3,11,39], which differ by the stacking of the single layer arrangement shown in Fig. 1(a). The magnetic structure of the main antiferromagnetic b component is either A or B centered. In the A-centered phase the two magnetic moments at (0,0,0) and (0,0.5,0.5) are parallel; in the B-centered one the two moments at (0,0,0) and (0.5,0,0.5) are parallel. The magnetic space groups are $Pbca$ (A centered) and $Pbc'a'$ (B centered). While in $Pbca$ the net ferromagnetic canted moments per layer cancel due to an antiferromagnetic stacking, the B-centered $Pbc'a'$ structure results in a total ferromagnetic moment that can be measured with a magnetometer. There is also canting along the c direction in both magnetic structures. This canting corresponds to an antiferromagnetic c component that is B centered in $Pbca$ and A centered in $Pbc'a'$. This moment should, however, be small because the main part of the ordered moment points along the tilt axis, and only microscopic methods can detect such an antiferromagnetic c component.

The analysis of the magnetic Bragg peaks with polarization analysis first confirms that moments point along the b direction and show a dominating B-centered scheme for 1Ti and an almost exclusive B-centered scheme for 1TiB, see Appendix B. In contrast, small pure CRO samples show only the A-centered scheme [39].

In Fig. 2(a) the magnetization upon heating in a magnetic field of 0.1 T applied in the ab plane is shown for different Ti contents. The weak ferromagnetic component dominates the magnetization below T_N. The fact that the magnetization of the lowest temperature is the highest, points to a dominating
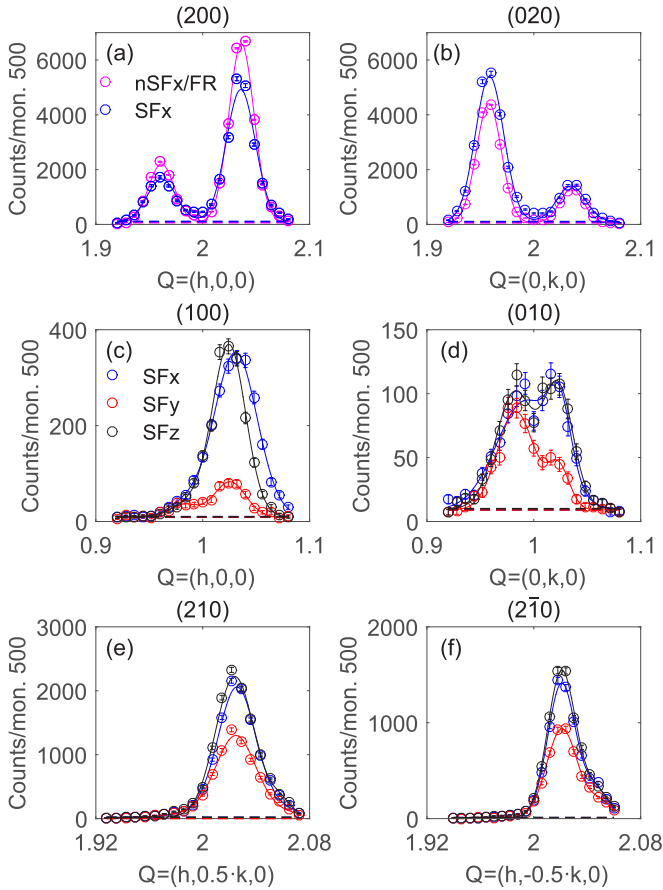
FIG. 4. Elastic neutron scattering scans with polarization analysis. The orthorhombic splitting is clearly visible in these elastic scans. (a),(b) present the values of the nSFx (SFx) channel in magenta (blue) of longitudinal scans across the strong nuclear reflections (200) and (020), respectively. The values of the nSFx channel are divided by the FR. These elastic longitudinal scans show that both twins are well separated. (c)–(f) present data of the SFx (blue), SFy (red), and SFz (black) channels of scans across the magnetic (c) (100), (d) (010), (e) (210), and (f) (2$\bar{1}$0) reflections.
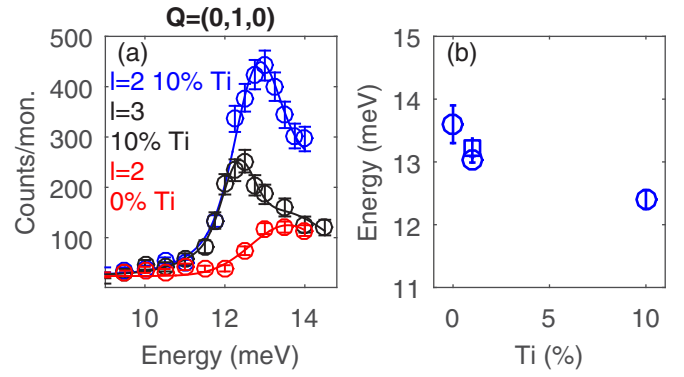

FIG. 5. Influence of Ti substitution on the anisotropy gap. (a) shows energy scans through the anisotropy gap at the antiferromagnetic zone center using the crystal 10Ti, $l = 2$ (blue) and $l = 3$ (black) and 0Ti, $l = 2$ (red). In (b) the energy of the lower zone-center mode of crystals with different Ti content is shown, the data for 1% Ti are from Ref. [24].

thus a rough estimate of the Dzyaloshinski-Moriya interaction in CRO: $D = 0.06J$. The magnetization curves further show a decrease of the Néel temperature with increasing Ti content, see Table II in Appendix A, which can be explained by the dilution of the magnetic lattice by nonmagnetic Ti.

3. Impact of Ti substitution on magnetic excitations

In Fig. 5 the influence of different Ti substitutions on the anisotropy gap in the magnon dispersion is addressed by comparing constant **Q** scans across the in-plane gap at the antiferromagnetic zone center. The modes are slightly split due to finite interlayer interaction, see Sec. III B. Even l corresponds to the higher and odd to the lower modes, respectively. The lower zone-center magnon energy is displayed as function of Ti doping in Fig. 5(b). The anisotropy gap clearly diminishes with increasing Ti content. Since the nonmagnetic Ti dilutes the magnetic lattice, a general softening can be expected, as it is visible in the anisotropy gap, which in first view corresponds to the square root of exchange and anisotropy energies. In addition, Ti also perturbs the lifting of orbital degeneracy, as it is shown in Fig. 3. In consequence also the single-ion anisotropy will be reduced with increasing Ti content. The impact of a small Ti content of the order of one percent on the magnon dispersion can, however, safely be neglected. 10Ti, which is essentially untwinned, shows a l dependence of the anisotropy gap [Fig. 5(a)] consistent with the previous study [24].

B. Magnon dispersion in Ca$_2$Ru$_{0.99}$Ti$_{0.01}$O$_4$

1. Polarization of magnon modes

With the alignment of the antiferromagnetic moment along b one expects nondegenerate transverse magnon modes corresponding to polarization along a or c [31]. With our previous unpolarized INS experiments [24] only the a polarized mode could be clearly identified. The gap of the c polarized transverse mode could either be hidden in the shoulder of the in-plane signal, which inevitably arises from the folding of the instrument resolution with the steep spin-

B-centered phase [11] in agreement with the neutron diffraction studies. The small crystal used for the magnetization measurement with 1% Ti content is essentially untwinned, while the sample containing no Ti is partially twinned with nonidentical twin fractions. If the field is applied along [110], the observable ferromagnetic component is reduced by a factor $1/\sqrt{2}$ but both twin domain orientations contribute (sample containing 10% Ti). The highest total ferromagnetic component is observed in the pure sample, and the reduced ferromagnetic component in 1Ti is possibly caused by a slightly reduced B-centered phase fraction. We can conclude that CRO exhibits sizable moment canting resulting in an ordered ferromagnetic component along the a direction of $\sim 0.08\mu_B$ (canting angle $\alpha = 3.5$ deg). The canting of the magnetic moment arises from a strong Dzyaloshinski-Moriya interaction that in turn stems from the strong SOC. Minimizing the static energy of a pair sensing only the Heisenberg interaction J and the Dzyaloshinski-Moriya interaction, $-\mathbf{D} \cdot \mathbf{S_i} \times \mathbf{S_j} - J\mathbf{S_i} \cdot \mathbf{S_j}$, yields the condition $\tan(2\alpha) = D/J$, and

wave dispersion, or appear at higher energies where weak signals were detected [24]. With the new polarized experiment the in-plane and c polarized transverse magnons can be easily separated in the polarization, and it was the first aim to search for the c polarized mode at the antiferromagnetic zone center.

Figures 6(a)–6(c) shows energy scans through the anisotropy gap at the antiferromagnetic zone centers **Q** = (2,1,0) and (1,2,0). The nSF channels shown in Fig. 6(a) have a larger background than the SF channels [Figs. 6(b) and 6a(c)] and are thus less informative but confirm the main conclusions. The c polarized mode must entirely contribute to the SFy and nSFz channels with a complete geometry factor. Spin-wave calculations show that the two nondegenerate transverse modes exhibit an intrinsic signal strength inversely proportional to their zone-center energy [31]. Therefore, the c polarized mode can be excluded in the asymmetric peak of the in-plane transverse mode. These scans confirm the in-plane character of the signal in the range 14 to 20 meV, see Fig. 6(d). A special effort was laid on the analysis of the signal maximum at the in-plane magnon gap, $E = 14$ meV, see Figs. 6(e) and 6(f). With the partially detwinned crystal one expects this signal from the transverse magnon to be reduced by a factor 0.6 for **Q** = (2,1,0), which agrees with the measured ratio of the intensities at 14 meV between **Q** = (2,1,0) and **Q** = (1,2,0) of 0.55(10). We also measured the backfolded mode at the ferromagnetic zone center, which according to the spin-wave calculations, see below, exhibits a c polarization. Indeed such a c polarized signal can be determined at $Q = (2,0,0)$ and $E = 14$ meV [Fig. 6(g)] by counting for a very long time (45 min for each data point).

In view of the recent observation of longitudinal magnetic excitations in CRO [25] it seemed worthwhile to further search for such modes. Here the term longitudinal mode designates a fluctuation along the sublattice magnetization that in a common system with well-defined local moments is suppressed; longitudinal excitations, however, always arise from excitation and absorption of an even number of magnons as it has been demonstrated for MnF$_2$ [40]. We first studied the two antiferromagnetic zone centers (2,1,0) and (1,2,0), where longitudinal excitations arising from two-magnon processes are expected at the lowest energies [40]. In Fig. 6(i) the fitted background from the in-plane polarized transverse mode from Fig. 6(d) is used to separate a weak signal peaking at 29 meV. The signals for the two different **Q** values are assumed to possess the same shape but are scaled with the expected factors for geometry and twinning. Around 30 meV the stronger signal for **Q** = (2,1,0) compared to **Q** = (1,2,0) thus points to a longitudinal excitation in the sense that it is polarized parallel to the static moment parallel b. The energy of this mode corresponds fairly well to the double of the gap of the in-plane transverse branch and the strength is below 10% of that signal. Therefore, it seems most likely that this longitudinal signal stems from the two-magnon excitation, which is expected to appear in the longitudinal polarization channel [40,41]. Note that due to the large magnon gap in CRO, absorption processes do not play a role at low temperature, so that only the two-magnon excitation sensing twice the magnon gap is relevant in our measurements. A similar discussion about an intrinsic longitudinal mode has also been initiated
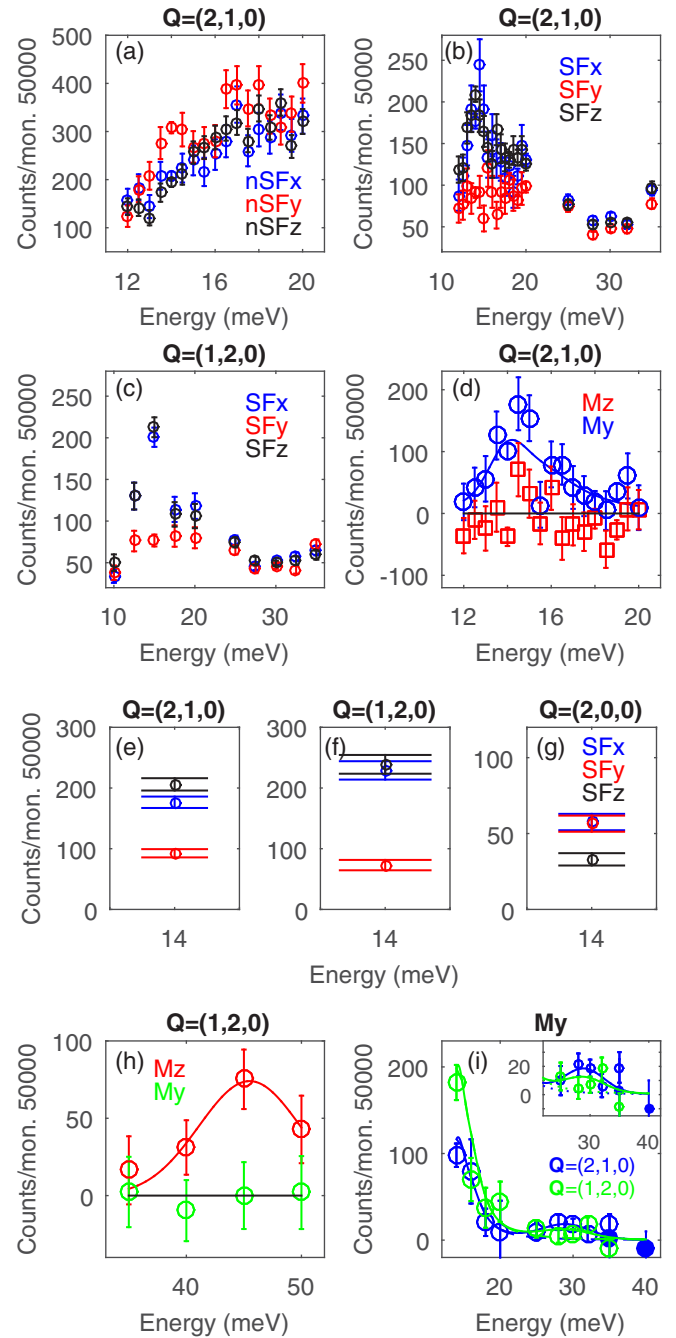
FIG. 6. Energy scans at various **Q** values with polarization analysis taken on partially twinned 1Ti. Raw data of different (a) nSF, and (b),(c),(e)–(g) SF channels with the polarization parallel to **x** (**y**),(**z**) in blue (red), (black) at different scattering vectors. (d),(h),(i) show the results of the polarization analysis with Eq. (1), in red M$_z$, and M$_y$ in blue (green) at **Q** = (2,1,0) (**Q** = (1,2,0)). In (d) the blue line depicts the modeled asymmetric shape resulting from the folding of the magnon dispersion with the resolution function, see Ref. [24], which is also used for the modeling in (i), but scaled with the expected correction factors for geometry and twinning fractions. The inset in (i) shows a zoom into the data.

for the parent material of FeAs-based superconductors, for which again the two-magnon explanation seems most likely

[31,42–44]. The 29 meV longitudinal signal observed in CRO at the antiferromagnetic zone center is thus not anomalous but just corresponds to the two-magnon excitation expected to contribute to the longitudinal channel.

The c polarized antiferromagnetic zone-center mode is detected at higher energy, where the unpolarized experiment found some evidence for additional scattering [24] but where the signal strength is expected to be rather small [31]. In order to cover the energies of the order of 40 meV we needed to use a larger value of $k_f = 4.1$ Å^{-1}, which also allows one to avoid the contamination appearing at $E = 44$ meV for the standard value of $k_f = 2.662$ Å^{-1}. The magnetic signals polarized along $\mathbf{z} \simeq c$ and along $\mathbf{y}$ at large energies are shown in the scan at $(1,2,0)$ in Fig. 6(h) and show that the zone-center c-polarized magnon possesses a large energy of 45.5(1.5) meV. Its signal strength is in rough agreement with the signal strength of the in-plane transverse mode, because the energy is enhanced by a factor three. Our conclusion of c polarized modes at the ferromagnetic and antiferromagnetic zone centers agrees with the interpretation of similar polarized neutron scattering experiments performed with twinned crystals in a different scattering geometry [25].

This large c anisotropy is remarkable, as it strongly deforms the magnon dispersion in CRO with respect to a simple isotropic model. The splitting of the two antiferromagnetic zone-center magnons, 14 and 45.5 meV, is larger than the dispersion of the in-plane branch to the zone boundary. As will be discussed below, the entire dispersion of transverse branches is, nevertheless, well described with the $S = 1$ spin-wave model using the Holstein-Primakoff transformation. The in-plane and c-polarized branches exchange their character: While the c-polarized mode is the high-energy mode at the antiferromagnetic zone center, it appears at the lower energy of the in-plane transverse magnon at the ferromagnetic zone center, in accordance to the data shown in Fig. 6(g). The in-plane polarized branch thus starts at 14 meV at the antiferromagnetic zone center, exceeds to the zone boundary at 41 meV and then continues to stiffen till 45.5 meV at the ferromagnetic zone center. The out-of-plane polarized branch just exhibits the opposite dispersion. By comparing the intensities at the ferromagnetic zone centers $\mathbf{Q} = (2,0,0)$ and $\mathbf{Q} = (0,2,0)$ with an energy transfer of 45 meV we may confirm the in-plane transverse character of this high-energy mode appearing at the ferromagnetic zone center. The expected ratio of the signals taking into account the different twinning fractions and geometry factors amounts to 1:2.5 for a transverse and to 2.5:1 for a longitudinal magnon. We obtain a ratio of 0.1(2) indicating the transverse in-plane character. Evidence for an intrinsic longitudinal high-energy branch could not be obtained in our experiment [25,45].

2. Spin-wave calculations of the magnon dispersion

The anisotropy gap of the c-polarized transverse magnon of 45.5 meV leads to the uncommon feature in the magnon dispersion, that the transverse in-plane branch continues to increase in energy between the zone boundary and a ferromagnetic zone center [25]. This peculiarity can, however, be well described with a rather conventional model.
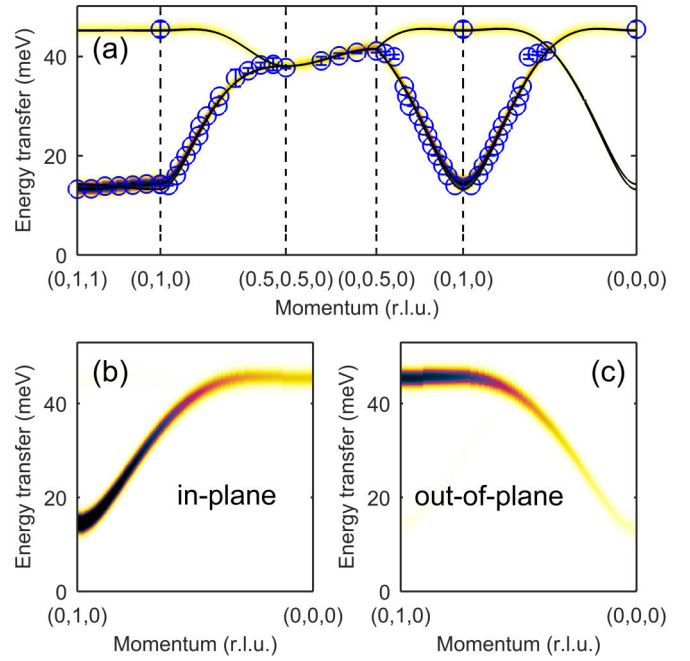
FIG. 7. Magnon dispersion calculated with the SpinW program using the values given in the text. The blue circles denote the fit values of the dispersion obtained in this and previous [24] neutron scattering studies. The black lines are the calculated dispersion and the color code denotes the calculated neutron scattering intensity of the convoluted spectra. In each panel black stands for maximum intensity and white for none. In (a) all transverse magnon modes are shown and in (b),(c) only the in-plane- and out-of-plane polarized transverse modes are shown, respectively, illustrating the opposite dispersion of these branches.

The Hamiltonian, which is used for the description of the magnon dispersion is given by:

$$H = \sum_{\mathbf{i},\mathbf{j}} J_{i,j} \mathbf{S_i} \cdot \mathbf{S_j} + \gamma \sum_i \left(S_i^x \right)^2 + \epsilon \sum_i \left(S_i^z \right)^2. \quad (2)$$

The sum runs over pairs of magnetic ions, so that each pair or bond appears twice and S is set to 0.67 following the experimental results in Ref. [11]. The spin-wave calculations using the SpinW program and the parameters $J = 5.6$ meV, $J_{na,b} = 0.6$ meV, $J_c = -0.03$ meV, $\gamma = 1.4$ meV, and $\epsilon = 24.5$ meV give a good description of the magnon dispersion obtained in this and our previous [24] neutron scattering studies [Fig. 7(a)], and the main parameters J and ϵ agree with Ref. [25]. Panels Figs. 7(b) and 7(c) show the in-plane and c-polarized branches, respectively, starting at an antiferromagnetic zone center and proceeding to a ferromagnetic one. In this figure the color code denotes maximum neutron scattering intensity of the convoluted spectra with black color and zero intensity with white color. The energy resolution is set to 1 meV. The spin-wave calculation thus perfectly describes not only the energy dispersion but also the polarization of the magnon branches. Note that this rather uncommon dispersion is described with strong single-ion parameters arising from SOC. These strong anisotropy terms interfere with the Heisenberg interaction parameters in contrast to models invoking only weak anisotropy. Therefore, the J parameter differs from that obtained by fitting

only the lower part of the dispersion with a small uniaxial anisotropy [24]. Figure 7(a) shows that the nonsinusoidal parts of the dispersion are perfectly described, clearly better than without the strong anisotropy terms. It is, however, important to note that the model is not unique. It is possible to obtain similar fitting by partially reducing the single-ion anisotropy and by inducing an anisotropic nearest-neighbor interaction.

The coupling parameter J_c acting between neighboring layers splits the magnon modes into two by introducing a finite dispersion perpendicular to the planes. Whether the lower or upper mode is seen at $\mathbf{Q} = (0,1,0)$ is determined by the sign of J_c. With the partially detwinned crystals (in particular with the experiment on 1TiB) it is possible to determine the sign of this interaction. Here it is chosen to couple spins at (0,0,0) and (0,0.5,0.5). The dominant b components of these spins are parallel for the A centering and antiparallel for the B centering. If J_c is positive (negative), corresponding to an antiferromagnetic (ferromagnetic) coupling, the upper (lower) mode is seen at $\mathbf{Q} = (0,1,0)$. The experimental data reveal that the upper mode is seen at $\mathbf{Q} = (0,1,0)$, so the coupling is ferromagnetic, stabilizing the A-centered phase. This coupling contradicts the observation of a B-centered structure as the main magnetic scheme, see Sec. III B. CRO thus exhibits the uncommon situation that the minimum magnon energy does not occur at the magnetic Bragg peaks. This observation can be attributed to an anisotropic J_c which differs for the a and b spin components.

3. Density functional calculations of magnetic structure and interaction

The linearized augmented plane wave (LAPW) method as implemented in the WIEN2K package [46] was used for the DFT calculations. The exchange correlation potential for the generalized gradient approximation (GGA) was chosen to be in the form proposed in Ref. [47]. The SOC was treated in a second variational way. The parameter of the plane-wave expansion was chosen to be $R_{MT} K_{\max} = 7$, where R_{MT} is the smallest atomic sphere radii ($R_{MT}^{Ca} = 2.15$ a.u., $R_{MT}^{Ru} = 1.99$ a.u., $R_{MT}^{O} = 1.71$ a.u.) and $K_{\max}$ the plane-wave cutoff. We used a mesh consisting of 800 k points. The on-site Hubbard repulsion and intra-atomic Hund's exchange were taken to be $U = 3$ eV and $J_H = 0.7$ eV [48,49] in the GGA+U [50] and GGA+U+SOC calculations.

The exchange parameters were recalculated via total energies of three different collinear magnetic configurations (a ferromagnetic and two, in the c direction differently stacked, antiferromagnetic configurations) using the GGA+U approach. We found that $J = 4.9$ meV, which agrees with the results of the spin-wave calculations.

In order to estimate the single-ion anisotropy we add SOC to the calculation scheme and computed the energies of two configurations, where all spins are either directed along c or lie in the a,b plane. The antiferromagnetic order was assumed in these calculations. The lowest total energy corresponds to the configuration, where all spins are directed predominantly along the b axis. The single-ion anisotropy is found to be very large, $\epsilon = 20.1$ meV, again in good agreement with experiment.

Very recently microscopic magnetic parameters were calculated for similar U and J_H values finding a nearest-neighbor
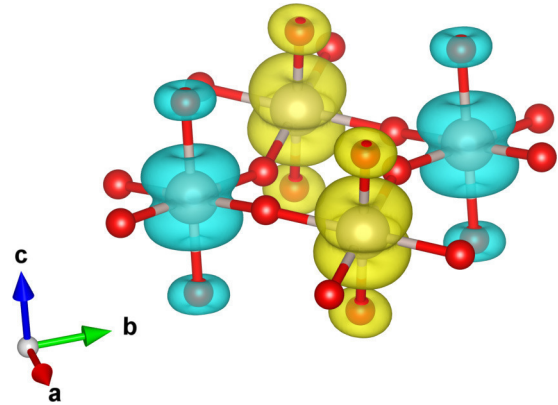

FIG. 8. The spin-density plot, as obtained in the GGA+U+SOC calculations with magnetic moments directed along the b axis. Small red balls are O ions. Different colors of the volumetric data correspond to different spin projections. One may see that there is no spin polarization on the planar oxygens, while apical ones have considerable magnetic moment, which is parallel to the moment of nearest Ru ions.

interaction of 3–6 meV and a large single ion anisotropy in good agreement with our results [51].

The spin moments were estimated by integrating the spin density obtained in the GGA+U+SOC calculation inside each atomic sphere with the radii R_{MT} specified for Ru and O above. The spin moment on the Ru ions was calculated to be $M_s^{Ru} = 1.27\mu_B$ (i.e., $S = 0.63$), while the orbital moment is $M_l^{Ru} = 0.13\,\mu_B$. We also find a sizable magnetic moment on the apical O $M_s^O = 0.11\mu_B$, while planar ligands stay nonmagnetic. The total spin density is shown in Fig. 8, which illustrates the significant polarization of the apical oxygens as well as the orbital character of the spin density at the Ru position. The total moment, $M_s^{Ru} + 2M_s^O - M_l^{Ru}$, agrees well with the powder neutron diffraction result [11], and the small value of the orbital moment indicates that CRO is not close to a $j = 0$ state driven by SOC as it is also deduced from the calculations in Ref. [51].

C. Additional modes and magnetic polarization of oxygen

The previous unpolarized experiments gave evidence for an additional scattering at the lower energy of 5 meV that could not be explained by the magnon dispersion expected for a simple square-lattice antiferromagnet. The data, which are presented in the mappings shown in Figs. 9(a) and 9(b), were obtained on the thermal TAS IN8 [24]. Panel (c) shows some characteristic scans included in (b). The 5 meV signal is much weaker than the in-plane transverse mode in particular when considering the by a factor of three reduced energy. Furthermore, it is not possible to connect this low-energy feature with a dispersing branch with a slope comparable to that of the transverse branch. Instead the intensity of this feature seems to be rather localized in $\mathbf{Q}$ space and to exhibit a flat dispersion. The signal could also be followed along the vertical direction without any indication for finite dispersion.

In Ref. [24] it was speculated that this extra mode could arise from the orbital disorder induced by the Ti substitution, a scenario which can now be ruled out by the comparison of Ti-containing and Ti-free CRO. Figures 9(d) and 9(e) show
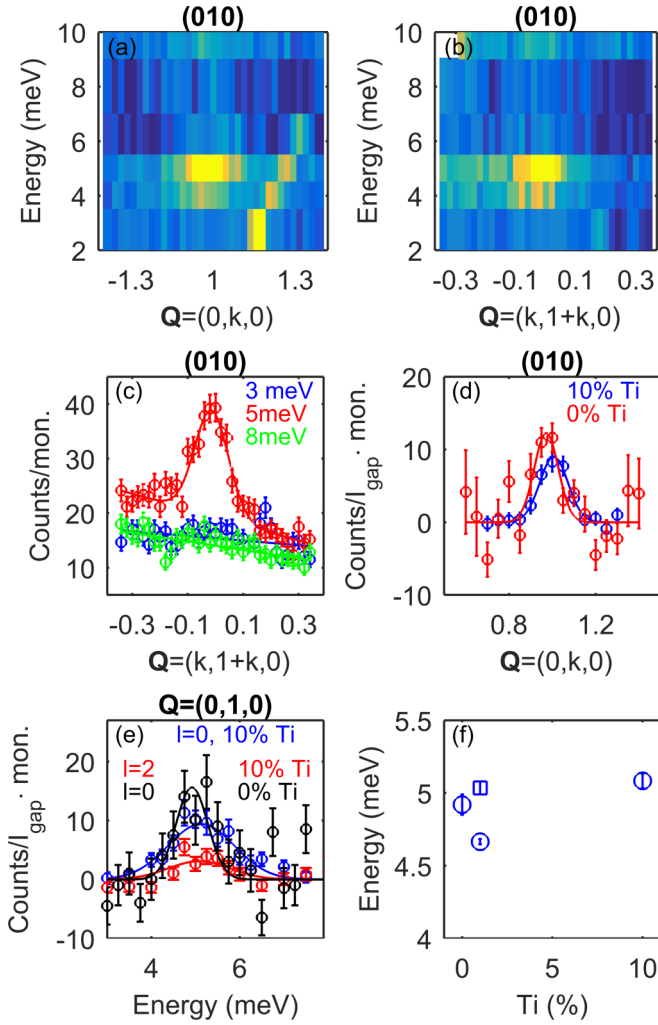
FIG. 9. Additional magnon branch near 5 meV. (a),(b) show scattering maps of energy versus **Q** taken on 1Ti. (c) presents some characteristic scans included in (b) for an energy transfer of 3 meV (5 meV), (8 meV) in blue (red), (green). The data in (a)–(c) are taken from Ref. [24]. (d) shows **Q** scans with an energy transfer of 5 meV for 10Ti (blue) and 0Ti (red). The intensities are scaled with the maximum intensities of the scans in Fig. 5. Scaled in the same way are the energy scans in (e) at **Q** = (1,0,l) using the crystals 10Ti, $l = 0$ (blue), $l = 2$ (red) and 0Ti, $l = 2$ (black). (f) presents the energy of this additional mode at **Q** = (0,1,0) for crystals containing different amounts of Ti.

Q and energy scans across the 5 meV signal on samples with 0 and 10% of Ti. Most interestingly there seems to be no difference in the strength of the low-energy signal when normalized to that of the in-plane gap mode at ∼14 meV. The additional signal is thus intrinsic to the magnetic order in CRO, and it is not induced by disorder, which must be significantly enhanced in Ti10. The Ti content furthermore does not change the energy of the additional scattering, see the fitted energy maxima displayed in Fig. 9(f). The minor variation between measurements on the same concentration on different spectrometers can be attributed to the energy calibration.
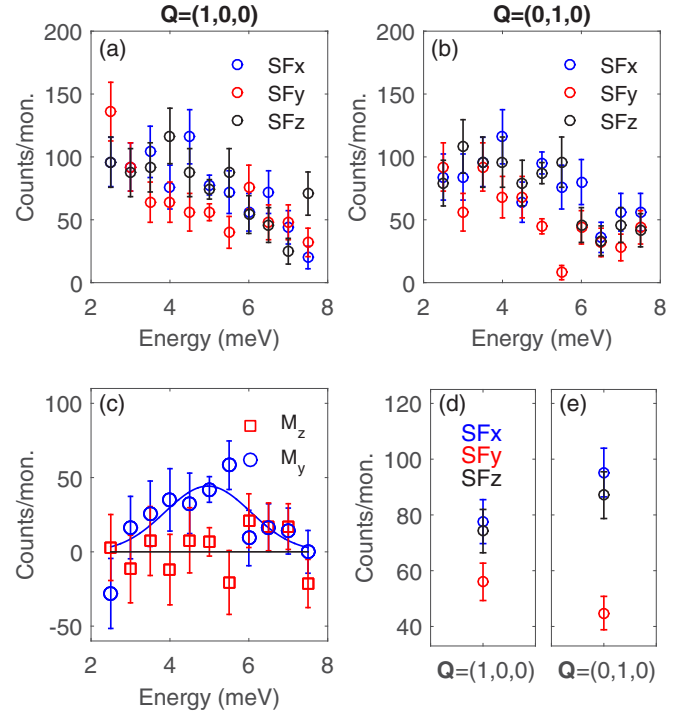
FIG. 10. Polarization analysis of the additional mode. SF intensities of energy scans at (a),(d) **Q** = (1,0,0), and (b),(e) **Q** = (0,1,0) for the SFx (SFy), (SFz) channel in blue (red), (black). (c) shows the results of the polarization analysis with Eq. (1), in red M$_z$ and in blue M$_y$. (d),(e) present only the 5 meV data of the two **Q** positions, which are measured with higher statistics.

The polarization of the additional mode was determined with polarized neutron scattering following the same procedures as those used to determine the character of the dispersion at higher energies. The polarization analysis directly shows that the additional excitation possesses an in-plane character, because it is not observed in the SFy channel (or in M_z), see Fig. 10. Comparing the intensities at **Q** = (1,0,0) and **Q** = (0,1,0) one may furthermore deduce that the additional mode is a polarized, which is transverse with respect to the static moment. The expected ratio of the intensities at 5 meV between **Q** = (0,1,0) and **Q** = (1,0,0) based on the twinning fractions and the geometry factor is 1:2.5 for an in-plane transverse mode and 2.5:1 for an in-plane longitudinal mode, respectively. The measured ratio is 0.25(21) characterizing this mode as an in-plane transverse mode.

The simple antiferromagnetic square lattice exhibits a magnon dispersion consisting of two transverse branches, which were both observed at larger energy in CRO, see above. In order to explain the additional mode the model needs to be extended, and the weakness and localization of the signal point to a smaller moment with smaller coupling.

The GGA+U calculations on CRO reveal a small magnetic moment situated at the two apical oxygens of 0.11 μ_B each. Such a polarization of the oxygen results from the strong hybridization between Ru 4d and O 2p orbitals. DFT calculations on several ferromagnetic or nearly ferromagnetic ruthenates find a sizable amount of magnetic moment on O, which in total sum up to about 30% of the entire magnetization

[52]. Experimentally this sizable magnetization of the O states has been observed by polarized neutron diffraction on $Ca_{1.5}Sr_{0.5}RuO_4$ where indeed 33% of the magnetization stems from O states [53]. CRO, however, exhibits antiferromagnetic order, in which the O bridging two antiparallel Ru moments cannot be polarized, see Fig. 1(a). Therefore, there is no moment on the in-plane O sites, which is also confirmed by the DFT calculations of CRO. However, the apical O is connected only to a single Ru site and can be polarized.

There are two principal contributions to the exchange between Ru and O moments due to hopping between O $2p$ and Ru $4d$ orbitals in the scenario where the Ru d_{xy} orbital is doubly occupied and the d_{xz} and d_{yz} singly occupied, see, e.g., Ref. [21]. One is a hopping from the p_x and p_y to the d_{xz} and d_{yz} orbitals, respectively. There, because of Pauli exclusion principle, only antiparallel spins can hop, leaving parallel spins in the now singly occupied O p orbitals. In total this yields a ferromagnetic coupling:

$$J_{Ru-O}^{t_{2g}-p} \sim \frac{-2t_{pd\pi}^2}{\varepsilon_{t_{2g}} - \varepsilon_p}, \tag{3}$$

where $t_{pd\pi}$ is the hopping integral between d_{xz} and p_x, and d_{yz} and p_y orbitals of Ru and oxygen. $\varepsilon_{t_{2g}}$ and ε_p are the centers of the Ru t_{2g} and apical O p bands. The factor two in Eq. (3) reflects the fact that there are two processes (virtual hoppings from p_x to d_{zx} and from p_y to d_{yz} orbitals) contributing to this ferromagnetic Ru-O exchange.

The second contribution to the Ru-O exchange comes from the hopping from the p_z orbital of O to the empty $d_{3z^2-r^2}$ orbital of Ru. Because of Hund's rule, predominantly parallel spins hop, leaving antiparallel spins on the O p_z orbital. This yields an antiferromagnetic coupling between Ru and O moments:

$$J_{Ru-O}^{e_g-p} \sim \frac{t_{pd\sigma}^2}{\varepsilon_{e_g} - \varepsilon_p} \frac{J_H}{\varepsilon_{e_g} - \varepsilon_p}. \tag{4}$$

Here $t_{pd\sigma}$ is the hopping matrix element between a p_z orbital of O and an empty $d_{z^2-r^2}$ orbital of Ru, cf. Ref. [21].

The σ hopping is larger than the π one ($|t_{pd\sigma}| \sim 2.2|t_{pd\pi}|$) [54], but the antiferromagnetic exchange (Eq. 4) occurs through the e_g band, which lies much higher in energy than t_{2g}. Our GGA+U calculations show that $\varepsilon_{t_{2g}} - \varepsilon_p \sim 1$ eV, while $\varepsilon_{e_g} - \varepsilon_p \sim 4.7$ eV. There is only one such antiferromagnetic exchange path, in contrast to two for ferromagnetic exchanges [Eq. (3)] and Hunds exchange on the Ru, $J_H \sim 0.7$ eV, also slightly reduces this exchange [Eq. (4)]. Therefore, one should expect ferromagnetic coupling to dominate, so that the moment of oxygen would be parallel to the moment of neighboring Ru. Our DFT calculations support this conclusion.

We have extended the spin-wave model by a small moment on the apical oxygens, 0.11 μ_B, coupled ferromagnetically to the next Ru moment, see Fig. 1(a). This extension necessitates to reduce the single-ion anisotropy parameter γ in order to keep the anisotropy gap of the in-plane transverse mode at the correct energy. The additional mode cannot be obtained at an energy near 5 meV at the antiferromagnetic zone center without introducing an anisotropy in terms of a single ion anisotropy for the magnetic moment on the O sites or an anisotropic coupling parameter. Because the single ion anisotropy stems from SOC which is small in O, the
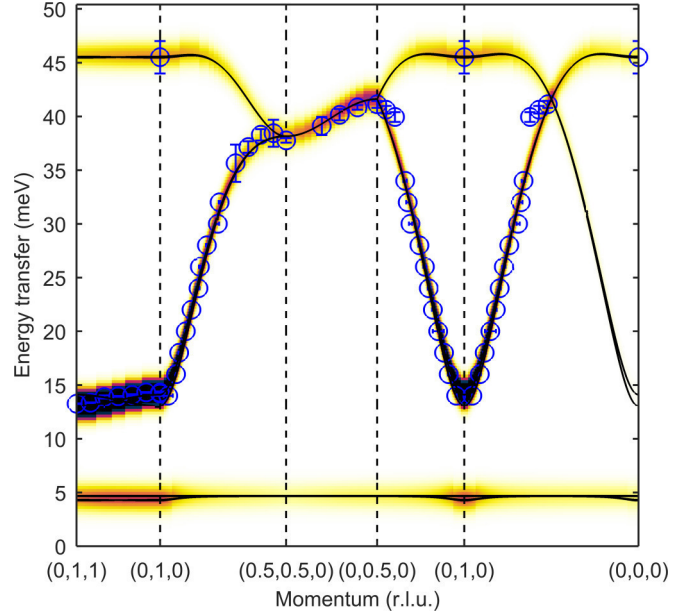
FIG. 11. Magnon dispersion calculated with the SpinW program including the additional mode. The labeling corresponds to the one in Fig. 7.

first scenario seems to be less likely. A better choice is an anisotropic coupling, because the Ru with its larger SOC is also involved in this process. Therefore, we used $J_{RuO} = (-1.5, -3.5, -1.5)$ meV to fit the experimental results. With this anisotropic coupling, γ has to be reduced to 0.5 meV to keep the in-plane transverse mode at the experimental value. With this extension we can perfectly describe the additional feature, see Fig. 11. The flat dispersion of the additional branch results from the lack of coupling between two O moments and perfectly describes the experimental finding. Also the localization of the signal strength at the antiferromagnetic zone center is well reproduced by this model. We can, therefore, conclude that the additional moment, situated on the apical O site and ferromagnetically coupled to the Ru, can explain the additional low-energy magnetic signal in CRO. We also tried to reproduce the data with the O moments being antiferromagnetically coupled to Ru, but such a scenario cannot explain the location of the scattering in Q space.

The significant polarization of the O site is another consequence of the strong hybridization of the Ru $4d$ and O p orbitals resulting in large hopping parameters, which can already be deduced from the closeness of the metallic phase of CRO. It furthermore yields a convincing explanation of the reduced moment, because the in-plane oxygen ion, which should carry a similar amount of charge carriers, cannot be magnetically polarized in the antiferromagnetic structure reducing the ordered moment from the simple $S = 1$ expectation. The ordered moment may thus also oscillate in length by transferring moment between Ru and in-plane O, which can give rise to a longitudinal mode, as an alternative explanation for the observation in Ref. [25].

IV. CONCLUSIONS

10% Ti substitution in CRO results in a stabilization of the insulating phase up to at least 700 K and reduces the

TABLE I. Structural data of the single crystal x-ray diffraction analysis.

Ti content	10%	10%	1%	1%	0%	0%
Temperature	100 K	293 K	100 K	293 K	100 K	293 K
wR(all,F)	0.022	0.0429	0.0521	0.048	0.0549	0.0262
Ru1, Ti1						
x	0	0	0	0	0	0
y	0	0	0	0	0	0
z	0	0	0	0	0	0
U_{11}	0.00119(3)	0.00284(3)	0.00197(5)	0.00348(5)	0.00295(4)	0.00368(4)
U_{22}	0.00164(4)	0.00330(4)	0.00245(5)	0.00368(5)	0.00373(5)	0.00409(5)
U_{33}	0.00151(4)	0.00378(3)	0.00262(4)	0.00390(4)	0.00351(5)	0.00403(4)
U_{12}	−0.00003(3)	−0.000019(15)	0.00000(4)	−0.00001(2)	0.00001(3)	−0.000015(12)
U_{13}	−0.00009(2)	−0.000172(13)	−0.00005(3)	−0.00019(2)	−0.00011(4)	−0.000187(12)
U_{23}	−0.00011(2)	−0.00025(2)	−0.00012(3)	−0.00021(2)	−0.00006(3)	−0.000228(14)
occupancy Ru	0.870(2)	0.866(2)	0.969(3)	0.978(3)	0.9768(18)	0.9859(17)
occupancy Ti	0.130(2)	0.134(2)	0.031(3)	0.022(3)		
Ca1						
x	0.00753(3)	0.01019(2)	0.00479(4)	0.00912(3)	0.00513(4)	0.00909(2)
y	0.05003(4)	0.03986(4)	0.05634(5)	0.04365(5)	0.05536(4)	0.04350(5)
z	0.352152(13)	0.351206(12)	0.352293(17)	0.350910(16)	0.35217(2)	0.350894(13)
U_{11}	0.00420(6)	0.00988(5)	0.00485(7)	0.01022(8)	0.00599(7)	0.01034(6)
U_{22}	0.00526(8)	0.01163(7)	0.00530(9)	0.01104(9)	0.00678(8)	0.01153(8)
U_{33}	0.00261(5)	0.00530(5)	0.00360(7)	0.00523(7)	0.00460(8)	0.00537(6)
U_{12}	−0.00092(5)	−0.00239(4)	−0.00077(7)	−0.00227(5)	−0.00081(6)	−0.00220(3)
U_{13}	−0.00002(4)	0.00020(3)	0.00007(6)	0.00032(4)	0.00004(7)	0.00030(3)
U_{23}	−0.00047(4)	−0.00047(4)	−0.00022(6)	−0.00023(6)	−0.00021(6)	−0.00026(4)
occupancy	1	1	1	1	1	1
O1						
x	0.19908(12)	0.20016(9)	0.19577(15)	0.19758(12)	0.19604(16)	0.19770(9)
y	0.29878(14)	0.29890(10)	0.30051(15)	0.30081(12)	0.30057(16)	0.30061(9)
z	0.02532(6)	0.02228(5)	0.02700(7)	0.02325(6)	0.02681(9)	0.02322(4)
U_{11}	0.0048(2)	0.00732(15)	0.0049(3)	0.0072(2)	0.0057(3)	0.00734(16)
U_{22}	0.0052(3)	0.00788(18)	0.0050(3)	0.0068(2)	0.0059(3)	0.00695(16)
U_{33}	0.0060(2)	0.01175(18)	0.0061(3)	0.0108(2)	0.0074(3)	0.01106(17)
U_{12}	−0.0024(2)	−0.00339(13)	−0.0019(2)	−0.00312(18)	−0.0016(2)	−0.00263(12)
U_{13}	−0.00055(17)	0.00025(14)	0.0006(2)	0.00088(18)	0.0005(3)	0.00107(13)
U_{23}	0.00039(19)	−0.00013(15)	0.0000(2)	−0.0010(2)	−0.0004(3)	−0.00078(14)
occupancy	1.033(4)	1.028(3)	1.016(4)	1.014(4)	1.012(5)	1.009(4)
O2						
x	−0.06456(13)	−0.05697(12)	−0.06762(18)	−0.05808(18)	−0.06701(18)	−0.05813(13)
y	−0.01939(14)	−0.01561(11)	−0.02114(16)	−0.01661(13)	−0.02093(16)	−0.01684(10)
z	0.16450(6)	0.16468(4)	0.16458(7)	0.16488(6)	0.16453(9)	0.16491(4)
U_{11}	0.0064(2)	0.0121(2)	0.0071(3)	0.0128(3)	0.0082(3)	0.0123(3)
U_{22}	0.0072(3)	0.0132(2)	0.0067(3)	0.0125(3)	0.0080(3)	0.0125(2)
U_{33}	0.0034(2)	0.00558(16)	0.0045(3)	0.0055(2)	0.0059(3)	0.00531(16)
U_{12}	0.00075(20)	0.00089(15)	0.0005(2)	0.0009(2)	0.0004(2)	0.00108(15)
U_{13}	0.00013(16)	0.00065(14)	0.0004(2)	0.00065(19)	−0.0001(3)	0.00066(15)
U_{23}	0.00001(18)	0.00023(13)	0.0002(2)	0.0002(2)	0.0002(3)	−0.00008(13)
occupancy	1.046(5)	1.040(5)	1.025(5)	1.029(5)	1.028(6)	1.012(5)

structural distortions, but magnetic properties are very little changed. Crystals with only 1% of Ti show only minor shifts of structural and magnetic transition temperatures and can thus be taken as representative for pure CRO.

Various neutron scattering experiments on partially untwinned crystals of Ca$_2$Ru$_x$Ti$_{1-x}$O$_4$ were performed to determine the magnetic structure and magnon dispersion in the insulating state. Most remarkable is the large magnetic anisotropy, which results in a splitting of the two transverse

zone-center modes that exceeds the full dispersion because of magnetic exchange. The entire dispersion of transverse magnon branches, however, is perfectly described by a conventional spin-wave model, in which the strong impact of the SOC is reflected by large anisotropy parameters. DFT calculations within the GGA$+U$ approximation yield an orbital moment of only $0.13 \mu_B$, which indicates that CRO is not close to a $j = 0$ state, which can be seen in the discrepancy of the experimental magnon dispersion with the

$j = 0$ calculation [23]. The calculated magnetic interaction and anisotropy parameters reasonably well agree with those obtained by fitting the dispersion, and also the ordered moment is correctly reproduced in the DFT calculation.

The DFT study finds a sizable amount of magnetic moment on the apical oxygen reminiscent of previous reports on ferromagnetic ruthenates. This additional moment explains an additional signal appearing in the neutron scattering experiments at lower energy and limited to the antiferromagnetic zone center. Extending the spin-wave model to the weakly ferromagnetic coupled oxygen moments describes the flat dispersion and the limited appearance in **Q** space of this signal. The spin-wave dispersion in CRO is thus dominated by the impact of strong SOC and by the presence of magnetic moments on the oxygen sites.

Note added in proof. Recently, a revised version of Ref. [25] appeared as [55].

TABLE II. Structural and physical characteristics of crystals containing different amounts of Ti.

	0% Ti	1% Ti	10% Ti
T_N (K)	112.6(2)	112.3(2)	107.2(3)
T_{MI} (K)	362(1)	358(1)	
300 K			
a (Å)	5.4098(3)	5.4098(3)	5.4247(4)
b (Å)	5.4691(4)	5.4683(4)	5.4585(5)
c (Å)	11.9745(6)	11.9781(9)	11.9536(9)
ϵ	0.00545(14)	0.00537(17)	0.00311(17)
$Ru - O1_{aver.}$ (Å)	1.9816(8)	1.9852(7)	1.9779(5)
$Ru - O2$ (Å)	2.0018(9)	2.003(8)	1.9932(5)
$O - O \| a$ (Å)	2.815(1)	2.817(1)	2.815(1)
$O - O \| b$ (Å)	2.792(1)	2.792(1)	2.782(1)
$\theta - O1$ (deg)	11.253(17)	11.38(2)	10.896(12)
$\theta - O2$ (deg)	9.278(20)	9.423(2)	9.260(9)
ϕ (deg)	11.628(16)	11.666(13)	11.171(11)
100 K			
a (Å)	5.377(11)	5.3957(3)	5.4189(4)
b (Å)	5.5915(12)	5.6023(3)	5.5483(5)
c (Å)	11.789(3)	11.7725(7)	11.7982(10)
ϵ	0.0176(2)	0.0188(4)	0.0118(6)
$Ru - O1_{aver.}$ (Å)	2.0099(6)	2.0120(6)	1.9996(5)
$Ru - O2$ (Å)	1.9765(12)	1.9751(8)	1.9753(7)
$O - O \| a$ (Å)	2.829(1)	2.829(1)	2.827(1)
$O - O \| b$ (Å)	2.856(1)	2.862(1)	2.829(1)
$\theta - O1$ (deg)	12.912(21)	12.986(16)	12.201(14)
$\theta - O2$ (deg)	11.089(19)	11.199(19)	10.680(11)
ϕ (deg)	11.801(18)	11.823(17)	11.287(15)

APPENDIX A: CRYSTAL STRUCTURE DETERMINATION OF $Ca_2Ru_xTi_{1-x}O_4$

Complete crystal structure analyses were performed with an X8-APEX by Bruker AXS single-crystal diffractometer with a goniometer in kappa geometry and x-ray radiation from a molybdenum anode with a wavelength of $\lambda = 0.71073$ Å. The distance between the sample and the detector was set to 50 mm. Structure refinements were carried out using Jana2006 [56]. A type I extinction correction was applied during the refinements and the data were corrected for absorption. The thermal parameters for Ru1 and Ti1 were constrained to be equal, and the total occupancy of this site was fixed to 1. The results of the structural refinements are given in Table I. Table II presents further characteristics of the crystal structure as well as the metal-insulator- and antiferromagnetic transition temperatures. T_N is determined from the magnetization curves presented in Fig. 2(a) by finding the zero point of the second
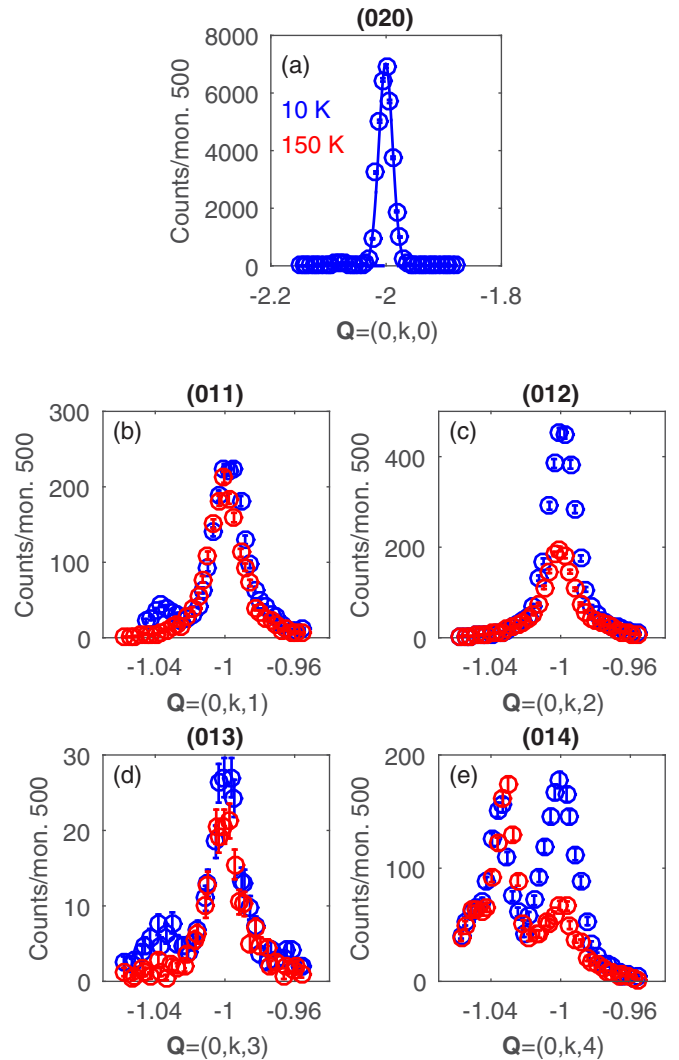
FIG. 12. Elastic neutron scattering scans of 1TiB across (a) **Q** = (0,2,0), (b) **Q** = (0,1,0), (c) **Q** = (0,1,l), (d) **Q** = (0,1,2), (e) **Q** = (0,1,2). Blue color denotes scans taken in the magnetic phase at 10 K and red color scans taken in the nonmagnetic phase at 150 K.

derivation. T_{MIT} is determined in the same way from the resistance curves presented in this figure.

APPENDIX B: MAGNETIC STRUCTURE DETERMINATION OF $Ca_2Ru_{0.99}Ti_{0.01}O_4$

The crystal 1TiB used in our previous neutron scattering study [24] was further investigated on the thermal TAS IN3 at the ILL. The crystal was mounted in the [010]/[001] orientation into a ILL orange cryostat, k_f was set to 2.662 $Å^{-1}$ for all scans and a pyrolitic graphite filter was used to suppress higher order wavelength. Rocking scans revealed the mosaic spread to be less than $0.5°$. With the good resolution of the IN3 it is easily possible to resolve the Bragg peaks from the two twins present in the crystal. The twinning ratio amounts to 20:1, which is deduced from rocking scans of strong nuclear Bragg reflections at the 2Θ scattering angles of the (020) and

(200) reflections. Figure 12(a) shows a longitudinal scan over the (020) reflection; the smaller twin is barely seen in the tail. Scans across the positions, where magnetic scattering can be expected, are shown in (b)–(e). There several scans of the kind (01l) are compared at 10 K, in the antiferromagnetic phase, and at 150 K, in the nonmagnetic phase. It is clearly seen that the minority twin gains intensity for an odd l and not for an even l. The majority twin gains intensity for even l and much less, but also clearly detectable, for odd l. The (012) and (014) reflections are magnetic Bragg peaks for the B-centered phase but not for the A-centered one. So the strong gain of intensity of these reflections in the antiferromagnetic phase reveals an almost exclusive B-centered phase. Opposite the (011) and (013) peaks are Bragg peaks in the A-centered phase, but not in the B-centered one. So the gain of intensity at low temperatures of those peaks points to the A-centered phase, which is however much weaker than the gain of the Bragg peak intensities of the B-centered phase. So the main stacking scheme of this crystal is the B-centered one.

[1] S. Nakatsuji, S. Ikeda, and Y. Maeno, J. Phys. Soc. Jpn. **66**, 1868 (1997).

[2] S. Nakatsuji and Y. Maeno, Phys. Rev. Lett. **84**, 2666 (2000).

[3] O. Friedt, M. Braden, G. André, P. Adelmann, S. Nakatsuji, and Y. Maeno, Phys. Rev. B **63**, 174432 (2001).

[4] J. P. Carlo, T. Goko, I. M. Gat-Malureanu, P. L. Russo, A. T. Savici, A. A. Aczel, G. J. MacDougall, J. A. Rodriguez, T. J. Williams, G. M. Luke, C. R. Wiebe, Y. Yoshida, S. Nakatsuji, Y. Maeno, T. Taniguchi, and Y. J. Uemura, Nat. Mater. **11**, 323 (2012).

[5] S. Nakatsuji, V. Dobrosavljević, D. Tanasković, M. Minakata, H. Fukazawa, and Y. Maeno, Phys. Rev. Lett. **93**, 146401 (2004).

[6] Y. Maeno, H. Hashimoto, K. Yoshida, S. Nishizaki, T. Fujita, J. G. Bednorz, and F. Lichtenberg, Nature (London) **372**, 532 (1994).

[7] K. Ishida, H. Mukuda, Y. Kitaoka, K. Asayama, Z. Q. Mao, Y. Mori, and Y. Maeno, Nature (London) **396**, 658 (1998).

[8] G. M. Luke, Y. Fudamoto, K. M. Kojima, M. I. Larkin, J. Merrin, B. Nachumi, Y. J. Uemura, Y. Maeno, Z. Q. Mao, Y. Mori, H. Nakamura, and M. Sigrist, Nature (London) **394**, 558 (1998).

[9] Y. Maeno, S. Kittaka, T. Nomura, S. Yonezawa, and K. Ishida, J. Phys. Soc. Jpn. **81**, 011009 (2012).

[10] C. S. Alexander, G. Cao, V. Dobrosavljevic, S. McCall, J. E. Crow, E. Lochner, and R. P. Guertin, Phys. Rev. B **60**, R8422 (1999).

[11] M. Braden, G. André, S. Nakatsuji, and Y. Maeno, Phys. Rev. B **58**, 847 (1998).

[12] T. Mizokawa, L. H. Tjeng, G. A. Sawatzky, G. Ghiringhelli, O. Tjernberg, N. B. Brookes, H. Fukazawa, S. Nakatsuji, and Y. Maeno, Phys. Rev. Lett. **87**, 077202 (2001).

[13] E. Gorelov, M. Karolak, T. O. Wehling, F. Lechermann, A. I. Lichtenstein, and E. Pavarini, Phys. Rev. Lett. **104**, 226401 (2010).

[14] D. Sutter, C. G. Fatuzzo, S. Moser, M. Kim, R. Fittipaldi, A. Vecchione, V. Granata, Y. Sassa, F. Cossalter, G. Gatti, M. Grioni, H. M. Rønnow, N. C. Plumb, C. E. Matt, M. Shi, M. Hoesch, T. K. Kim, T.-R. Chang, H.-T. Jeng, C. Jozwiak, A.

Bostwick, E. Rotenberg, A. Georges, T. Neupert, and J. Chang, Nat. Commun. **8**, 15176 (2017).

[15] J. H. Jung, Z. Fang, J. P. He, Y. Kaneko, Y. Okimoto, and Y. Tokura, Phys. Rev. Lett. **91**, 056403 (2003).

[16] T. Hotta and E. Dagotto, Phys. Rev. Lett. **88**, 017201 (2001).

[17] A. V. Puchkov, M. C. Schabel, D. N. Basov, T. Startseva, G. Cao, T. Timusk, and Z.-X. Shen, Phys. Rev. Lett. **81**, 2747 (1998).

[18] A. Liebsch and H. Ishida, Phys. Rev. Lett. **98**, 216403 (2007).

[19] A. Liebsch, Europhys. Lett. **63**, 97 (2003).

[20] V. I. Anisimov, I. A. Nekrasov, D. E. Kondakov, T. M. Rice, and M. Sigrist, Eur. Phys. J. B **25**, 191 (2002).

[21] D. I. Khomskii, *Transition Metal Compounds* (Cambridge University Press, Cambridge, England, 2014).

[22] G. Khaliullin, Phys. Rev. Lett. **111**, 197201 (2013).

[23] A. Akbari and G. Khaliullin, Phys. Rev. B **90**, 035137 (2014).

[24] S. Kunkemöller, D. Khomskii, P. Steffens, A. Piovano, A. A. Nugroho, and M. Braden, Phys. Rev. Lett. **115**, 247201 (2015).

[25] A. Jain, M. Krautloher, J. Porras, G. H. Ryu, D. P. Chen, D. L. Abernathy, J. T. Park, A. Ivanov, J. Chaloupka, G. Khaliullin, B. Keimer, and B. J. Kim, arXiv:1510.07011.

[26] H. Fukazawa, S. Nakatsuji, and Y. Maeno, Physica B (Amsterdam) **281**, 613 (2000).

[27] S. Kunkemöller, F. Sauer, A. A. Nugroho, and M. Braden, Cryst. Res. Technol. **51**, 299 (2016).

[28] J. Rodríguez-Carvajal, Physica B (Amsterdam) **192**, 55 (1993).

[29] S. Toth and B. Lake, J. Phys. Condens. Matter **27**, 166002 (2015).

[30] In *Neutron Scattering from Magnetic Materials*, edited by T. Chatterji (Elsevier Science, Amsterdam, 2005).

[31] N. Qureshi, P. Steffens, S. Wurmehl, S. Aswartham, B. Büchner, and M. Braden, Phys. Rev. B **86**, 060410 (2012).

[32] J. J. Randall and R. Ward, J. Am. Chem. Soc **81**, 2629 (1959).

[33] M. Braden, W. Reichardt, S. Nishizaki, Y. Mori, and Y. Maeno, Phys. Rev. B **57**, 1236 (1998).

[34] M. Braden, W. Reichardt, Y. Sidis, Z. Mao, and Y. Maeno, Phys. Rev. B **76**, 014505 (2007).

[35] M. Braden, A. H. Moudden, S. Nishizaki, Y. Maeno, and T. Fujita, Physica C (Amsterdam) **273**, 248 (1997).

[36] X. Ke, J. Peng, D. J. Singh, T. Hong, W. Tian, C. R. Dela Cruz, and Z. Q. Mao, Phys. Rev. B **84**, 201102 (2011).

[37] M. Braden, O. Friedt, Y. Sidis, P. Bourges, M. Minakata, and Y. Maeno, Phys. Rev. Lett. **88**, 197002 (2002).

[38] P. Steffens, J. Farrell, S. Price, A. P. Mackenzie, Y. Sidis, K. Schmalzl, and M. Braden, Phys. Rev. B **79**, 054422 (2009).

[39] P. Steffens, O. Friedt, P. Alireza, W. G. Marshall, W. Schmidt, F. Nakamura, S. Nakatsuji, Y. Maeno, R. Lengsdorf, M. M. Abd-Elmeguid, and M. Braden, Phys. Rev. B **72**, 094104 (2005).

[40] W. Schweika, S. V. Maleev, T. Brückel, V. P. Plakhty, and L.-P. Regnault, Europhys. Lett. **60**, 446 (2002).

[41] I. U. Heilmann, J. K. Kjems, Y. Endoh, G. F. Reiter, G. Shirane, and R. J. Birgeneau, Phys. Rev. B **24**, 3939 (1981).

[42] C. Wang, R. Zhang, F. Wang, H. Luo, L. P. Regnault, P. Dai, and Y. Li, Phys. Rev. X **3**, 041036 (2013).

[43] M. Fidrysiak, Eur. Phys. J. B **89**, 41 (2016).

[44] F. Waßer, C. H. Lee, K. Kihou, P. Steffens, K. Schmalzl, N. Qureshi, and M. Braden, arXiv:1609.02027.

[45] Jain *et al.* report evidence for a longitudinal mode appearing at 52 meV at the FM zone center. $\mathbf{Q} = (2,2,0)$ is the smallest scattering vector for which an energy transfer of 52 meV at a FM zone center is not prohibited by kinematics in our setup using $k_f = 4.1$ Å^{-1}. A smaller $\mathbf{Q}$ is however required due to the magnetic form factor in order to detect weak magnetic signals. In spite of very long counting we could not pick up a magnetic signal at this position. We also tried to find an almost equivalent longitudinal magnetic signal at $\mathbf{Q} = (2.2,0,0)$, where the longitudinal branch proposed in Ref. [25] should not possess an energy far from 52 meV and exhibit about half of the strength of the transversal branch at 45 meV at $\mathbf{Q} = (0,2,0)$, which we found to have 150(40) Counts/(mon 500000). At $\mathbf{Q} = (2.2,0,0)$ we could not pick up a sizable magnetic signal [13(34) and 16(39) Counts/(mon. 500000) for M_y and M_z, respectively]. So we cannot deliver experimental hints for this longitudinal mode, but we cannot exclude its presence due to the big error bars and the different $\mathbf{Q}$ position. Note that one data point in one spin flip channel is measured for 50 minutes.

[46] P. Blaha, K. Schwarz, G. Madsen, D. Kvasnicka, and J. Luitz, *WIEN2k, An Augmented Plane Wave + Local Orbitals Program for Calculating Crystal Properties* (Techn. Universität Wien, Wien, 2001).

[47] J. P. Perdew, K. Burke, and M. Ernzerhof, Phys. Rev. Lett. **77**, 3865 (1996).

[48] S. Lee, J.-G. Park, D. T. Adroja, D. Khomskii, S. Streltsov, K. A. McEwen, H. Sakai, K. Yoshimura, V. I. Anisimov, D. Mori, R. Kanno, and R. Ibberson, Nat. Mater. **5**, 471 (2006).

[49] S. V. Streltsov and D. I. Khomskii, Phys. Rev. B **86**, 064429 (2012).

[50] V. I. Anisimov, F. Aryasetiawan, and A. I. Lichtenstein, J. Phys. Condens. Matter **9**, 767 (1997).

[51] G. Zhang and E. Pavarini, Phys. Rev. B **95**, 075145 (2017).

[52] I. I. Mazin and D. J. Singh, Phys. Rev. B **56**, 2556 (1997).

[53] A. Gukasov, M. Braden, R. J. Papoular, S. Nakatsuji, and Y. Maeno, Phys. Rev. Lett. **89**, 087202 (2002).

[54] W. A. Harrison, *Elementary Electronic Structure* (World Scientific, Singapore, 1999), p. 817.

[55] A. Jain, M. Krautloher, J. Porras, G. H. Ryu, D. P. Chen, D. L. Abernathy *et al.*, Nature Physics, doi:10.1038/nphys4077; arXiv:1705.00222.

[56] V. Petříček, M. Dušek, and L. Palatinus, Z. Kristallogr. **229**, 345 (2014).

Magnetic shape-memory effect in SrRuO₃

S. Kunkemöller,[1] D. Brüning,[1] A. Stunault,[2] A. A. Nugroho,[3] T. Lorenz,[1] and M. Braden[1,*]

[1]*II. Physikalisches Institut, Universität zu Köln, Zülpicher Strasse 77, D-50937 Köln, Germany*

[2]*Institut Laue Langevin, 71 Avenue des Martyrs, CS 20156, F-38042 Grenoble Cedex 9, France*

[3]*Faculty of Mathematics and Natural Science, Institut Teknologi Bandung, Jalan Ganesha 10, 40132 Bandung, Indonesia*

As most perovskites, SrRuO₃ exhibits structural phase transitions associated with rotations of the RuO₆ octahedra. The application of moderate magnetic fields in the ferromagnetically ordered state allows one to control these structural distortions, although the ferromagnetic order occurs at six times lower temperature than the structural distortion. Our neutron-diffraction and macroscopic measurements unambiguously show that magnetic fields rearrange structural domains, and that for the field along a cubic $[110]_c$ direction, a fully detwinned crystal is obtained. Subsequent heating above T_C into the paramagnetic phase causes a magnetic shape-memory effect, where the initial structural domains recover.

The discovery of type-II multiferroics has initiated strong interest in the control of magnetism by electric fields as well as in its inverse, the control of a structural distortion by magnetic fields [1]. While commonly the combination of magnetism and ferroelectric order is considered in the field of multiferroics, the control of structural distortions by magnetic fields is not restricted to polar distortions. Here, we show that indeed also an antiferrodistortive structural distortion, an oxygen octahedron rotation occurring in most perovskites, can be driven by weak magnetic fields in SrRuO₃ due to a strong spin-orbit coupling. The manipulation of antiferrodistortive structural domains by magnetic fields opens new paths in magnetoelectric or magnetoelastic coupling in oxides, but it also has to be taken into account when analyzing the magnetic field dependence of any physical property in single-crystalline or thin-film SrRuO₃ [2].

Materials showing strong shape changes in response to an applied magnetic field are well known among Heusler alloys, in which the field either induces a structural phase transition or rearranges martensitic domains [3–5]. The fact that the initial shape can be recovered by reducing the magnetic field or by heating is called the magnetic shape-memory effect. In oxides these phenomena are very rare [6], but we discovered the domain rearrangement as well as the shape-memory effect in SrRuO₃ [7]. This perovskite exhibits many fascinating physical properties [2], such as an Invar effect of the thermal expansion [8], a linear resistivity that breaks the Ioffe-Regel limit at moderate temperatures [9], and an anomalous Hall effect [10] that has been linked to the existence of magnetic monopoles in momentum space [11] but is still intensely debated [2,12–14]. Many of the experimental studies of SrRuO₃ are performed using thin-film samples, because of the lack of high-quality single crystals [2]. Only recently have such crystals become available by the floating-zone growth technique in a mirror furnace [15,16].

The high-temperature cubic structure of SrRuO₃ [17] (space group $Pm\bar{3}m$) transforms upon cooling to a tetragonal ($I4/mcm$) phase at 975 K and at 800 K to an orthorhombic phase ($Pnma$) [7,18,19] [see Fig. 1(a)]. The symmetry reduction from cubic to orthorhombic results in six twin domain orientations that mimic the original cubic symmetry. The orthorhombic lattice parameters a, b, c are related to the cubic $a_c \simeq 3.93$ Å via $\vec{a} \parallel [101]_c$, $\vec{b} \parallel [010]_c$, and $\vec{c} \parallel [\bar{1}01]_c$ with $a \sim c \sim \sqrt{2}a_c$ and $b \sim 2a_c$ [20]. The fourfold axis of the tetragonal intermediate phase is b and can align along one of the cubic $[100]_c$, $[010]_c$, or $[001]_c$ directions, as is illustrated in Fig. 1(b). Thereby the twinning macroscopically restores the fourfold axes that are broken at the cubic-to-tetragonal transition. For each of these three arrangements, the orthorhombic a and c axes may interchange, leading to a total of six twin domain orientations [20], which restores the fourfold axis broken at the tetragonal-to-orthorhombic transition.

Large single crystals of SrRuO₃ were grown by the floating-zone technique as described in Ref. [16], from which we cut samples of nearly regular cubic shape with the edges aligned along the orthorhombic directions. Hence, four faces of the samples are cubic $(110)_c$ faces and two are cubic $(100)_c$ faces. The crystal structure of such a cube with an edge length of 3.2 mm was analyzed using the neutron diffractometer D9 at ILL [21]. The lattice-constant differences of the orthorhombic axes are too small to be resolved by the used instrument, thus the contributions of all six twins were superposed. The structural refinement is performed in space group $Pnma$ with JANA2006 [22] taking into account all six possible twin domain orientations as an incoherent superposition of intensities [21]. The refinement reveals the crystal to be twinned with highly unequal twinning fractions (see the Supplemental Material [21]), although no detwinning procedure was applied. The twinning fractions obtained at both temperatures agree within the error bars, underlining the reliability of the structural refinements including six twin domains and the proper treatment of the twin laws [21].

The twinning fractions and their changes in a magnetic field were investigated at the ILL D3 lifting-counter diffractometer using a crystal with an edge length of 2.5 mm [23]. In order to facilitate magnetic diffraction experiments, this sample was detwinned beforehand by applying the uniaxial-pressure procedure described in Ref. [16] and was aligned with the magnetic easy axis $c \parallel \vec{H}$. We analyzed the intensities of several Bragg reflections in order to determine the twinning
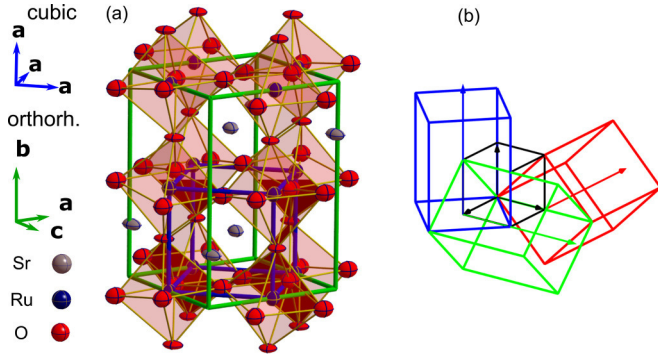
---

*braden@ph2.uni-koeln.de

FIG. 1. (a) Crystal structure of SrRuO$_3$ at 10 K as obtained from our single-crystal neutron-diffraction analysis. (b) Illustration of three orthorhombic twin orientations (colored) with their longest axis parallel to one of the cubic axes (black).

FIG. 2. Intensities of the (130), (031), and ($\bar{1}$30) reflections at various conditions. (a) and (b) show rocking scans of the (130) reflection at the starting point 200 K and 0 T (1), after cooling the sample to 2 K in 9 T (2), after heating to 200 K in 9 T (3), and finally at 230 K in 0 T (4). (c) shows the difference between the amplitudes at the starting point (1) and the successive steps (2)–(4). Amplitudes are obtained by fitting Gaussians with a constant background.

ratios. Uniaxial-pressure detwinning resulted in a sample with 85 vol % of the desired orientation, but the other twins could be clearly detected in our neutron-diffraction experiment. In the magnetic field and temperature dependent study we focused on the (031), (130), and ($\bar{1}$30) reflections because of their sizable intensity and accessibility with the lifting-counter diffractometer. Since the (130) reflection is forbidden in space group *Pnma*, its intensity results from the (031), (2$\bar{1}\bar{1}$), ($\bar{1}$12), (112), and (211) reflections of the other five twin orientations. These five reflections all possess a sizable structure factor comparable to the structure factor of the (031) reflection. Thus, the presence or absence of the (130) reflection signals, respectively, a multi- or a single-domain state with the twin orientation favored by the uniaxial pressure. The analysis of the ($\bar{1}$30) reflection, the Friedel equivalent of (130), yields the same information. We also analyzed the (031) reflection, which is allowed in space group *Pnma*, whereas the corresponding reflections of the other five twins are either forbidden or possess a considerably smaller structure factor. Therefore, the emergence of intensity at this reflection is opposed to that at the (130) and ($\bar{1}$30) reflections. The intensities of the three analyzed reflections did not change upon cooling from 170 to 10 K in the D9 experiment at zero field, proving that their intensity change cannot be associated with a change in the crystal structure, but must arise from a change in the twinning ratios. Figures 2(a) and 2(b) display the intensity at the (130) reflection in a sequence of magnetic field and temperature variations. Starting at 200 K and $\mu_0 H = 0$ T, the (130) intensity signals the presence of 15% minority twins. After field cooling in $\mu_0 H = 9$ T to 2 K, this (130) intensity is fully suppressed, i.e., the sample is transformed to the majority twin. On heating in 9 T to 200 K, the (130) intensity first partially reappears and then fully recovers at 230 K and $\mu_0 H = 0$ T. Note that at 230 K the sample is in its paramagnetic phase, but well below the structural transitions. Figure 2(c) presents the intensity changes of the (130) reflection together with those of the ($\bar{1}$30) and (031) reflections as a function of this sequence of four points in the magnetic field and temperature space. The intensities of (130) and of its Friedel equivalent ($\bar{1}$30) reflection well agree with each other, whereas the intensity of the (031) reflection shows the opposite behavior. Thus, all three reflections consistently reveal the systematic magnetic
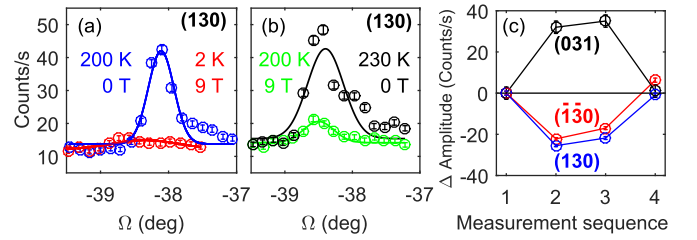
field and temperature dependence of the twinning ratio. At low temperature and high magnetic field the structural domains with the c axis parallel to the magnetic field grow at the cost of the other domains. Moreover, there is a shape-memory effect as the field-induced change of the domain fractions is reversed upon heating to the nonmagnetic phase. Note, however, that in contrast to the effect in Heusler alloys, the sample always stays in the structurally distorted phase.

The magnetic-field-induced switching of the structural domains also causes strong changes in the macroscopic sample length, which are studied using a capacitance dilatometer. Again, mm-sized single crystals of almost cubic shapes with edges parallel to the cubic [101]$_c$, [$\bar{1}$01]$_c$, and [010]$_c$ directions were used, which were partially detwinned by uniaxial-pressure cooling prior to the dilatometer experiments. After zero-field cooling to 5 K, the relative length changes $\Delta L_i(H)/L_0$ were measured along these three directions i up to $\mu_0 H = 9$ T in longitudinal configurations $\vec{H} \parallel L_i$. We find drastic elongations of the order of several 10^{-3} in the virgin curves of [101]$_c$ and [$\bar{1}$01]$_c$, when the field is initially ramped up, whereas much weaker effects are observed when the field is subsequently removed or reversed; see Fig. 3(a). For $\vec{H} \parallel L_i \parallel$ [010]$_c$, the behavior is completely different: The overall length change is reduced by about two orders of magnitude and the general field dependence is qualitatively different and almost nonhysteretic. These length changes can be naturally explained by magnetic-field-induced twin reorientations. The [101]$_c$ and [$\bar{1}$01]$_c$ directions refer either to the a, c, or [121] directions of orthorhombic domains. Thus, the magnetic field can pole the originally multidomain sample to a single-domain state with the magnetic easy axis c aligned along the field. Due to different orthorhombic lattice constants ($c/a = 1.0064$, $\sqrt{2}c/b = 1.0033$ at 10 K [24]), this poling causes a drastic elongation of several 10^{-3} in the respective virgin curves. The subsequent field-sweep cycle only requires a sign reversal of the magnetization $\vec{M}$, which can be achieved by a switching between 180° magnetic domains within a single structural domain. In the simplest view, such a sign reversal could occur without any length change, but one has to consider also the strains arising from the finite width of the domain walls during the magnetization reversal. These effects are small compared to the main effect in the virgin curve. The very weak
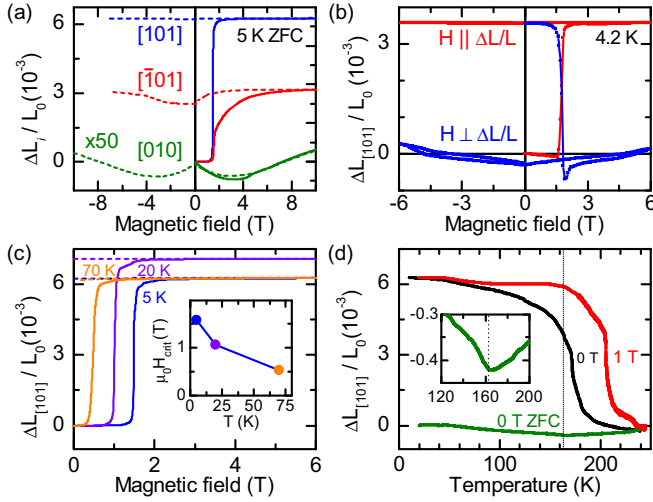
FIG. 3. (a) Relative length changes parallel to the magnetic field for the cubic $[110]_c$, $[\bar{1}01]_c$, and the $[010]_c$ directions (the data along $[010]_c$ were multiplied by a factor 50). Solid lines are virgin curves after zero-field cooling (ZFC) to 5 K, and dashed lines are obtained during subsequent field reversals. (b) Switching between the structural domains by applying the external field either along $[101]_c$ or along $[\bar{1}01]_c$ and measuring $\Delta L(H)/L$ along $[101]_c$. (c) $\Delta L(H)/L$ along $[101]_c$ for $H \parallel [101]_c$ as in (a), but for ZFC to $T = 5$, 20, or 70 K; the inset shows the reorientation fields of the corresponding virgin curves. (d) Temperature dependence $\Delta L(T)/L$ measured along $[101]_c$ for a multidomain state obtained by ZFC (green, with an enlarged view in the inset) in comparison to single-domain states, which were prepared by field poling at 5 K and decreasing the field to 0 (black) or 1 T (red). The vertical line marks $T_c = 163$ K of the ferromagnetic ordering.

effect for $\vec{H} \parallel L_i \parallel [010]_c$ has a similar origin, because this direction does not correspond to the magnetic easy axes of any of the six orthorhombic twin domains. The two orientations with $b \parallel \vec{H}$ have their easy axis in the plane perpendicular to the field, while the easy axes of the other four twins ($b \perp \vec{H}$) are at 45° with respect to $\vec{H}$. Consequently, the magnetic field cannot induce a structurally single-domain state with the longest axis $c \parallel \vec{H}$. Instead, the field first mainly reorients the 180° magnetic domains within the four $b \perp \vec{H}$ domains and then partially reorients the two $b \parallel \vec{H}$ domains into $b \perp \vec{H}$. In addition, the magnetization $\vec{M}$ continuously rotates from the respective easy c axis towards $\vec{H}$, as will be further discussed below in the context of the $\vec{M}(\vec{H})$ curves. This partial domain rearrangement, however, results in a much smaller length change, because the average of a and c differs from b by only 10^{-4} [24]. The corresponding changes $\Delta L_i(H)/L_0$ thus essentially reflect the intrinsic magnetostriction of SrRuO$_3$ and are in the range of 10^{-5}, as is typical for magnetic materials.

Figure 3(b) shows $\Delta L_i(H)$ data, which were obtained with a dilatometer that can be rotated in a split-coil magnet in order to vary the angle between $\vec{H}$ and the measured ΔL_i. For the measurement of $\Delta L_i \parallel [101]_c$, the partially detwinned sample was aligned with $[010]_c$ parallel to the rotation axis and we studied the longitudinal ($\vec{H} \parallel \Delta L_i \parallel [101]_c$) and the transverse ($\vec{H} \parallel [\bar{1}01]_c \perp \Delta L_i \parallel [101]_c$) configurations. Starting
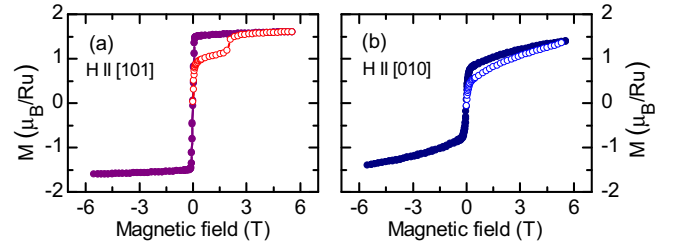

FIG. 4. Magnetization along the cubic $[101]_c$ (a) and $[010]_c$ (b) directions. Virgin curves (○) are obtained after zero-field cooling to 2 K and followed by full hysteresis cycles (●).

with an initially twinned crystal, a single-domain state with either $c \parallel [101]_c$ (longitudinal) or with $a \parallel [101]_c$ (transverse) is induced and remains stable after the field is removed again. The data of Fig. 3(b) were obtained after such an initial poling and clearly illustrate that the crystal reversibly switches between these two differently aligned single-domain states, if the field is subsequently applied and removed either in the longitudinal or the transverse direction. At $T \simeq 4.2$ K, the switching field amounts to $\mu_0 H_s \simeq 1.76$ T, in agreement with the corresponding values of Fig. 3(a) obtained on a different crystal. The magnetic-field-induced switching of the structural domains is remarkably sharp and, as shown in Fig. 3(c), the switching field decreases from $\mu_0 H_s \simeq 1.7$ T at 5 K to $\simeq 0.5$ T at 70 K.

Figures 3(c) and 3(d) illustrate the magnetic shape-memory effect of the structural domains. In zero field, the partially detwinned crystal exhibits a moderate temperature dependence of $\Delta L_i(T)/L_0$ ($L_i \parallel [101]_c$) with an anomaly at $T_c = 163$ K (see the inset). After field poling the crystal at 5 K to a single-domain state, very different $\Delta L_i(T)/L_0$ curves are obtained for $\mu_0 H = 0$ or 1 T. The temperature dependence of $\Delta L_i(T)/L_0$ is moderate up to about 100 or 150 K, but then a strong decrease of $\Delta L_i(T)/L_0$ sets in, which becomes most pronounced around 172 and 205 K for 0 and 1 T, respectively. The single-domain state enforced by the field poling thus remains stable up to rather high temperatures, but above the zero-field T_c the initial multidomain state recovers as in the diffraction experiment, which reveals the magnetic shape-memory effect [25].

The shape-memory effect must arise from a domain memory that withstands the domain realignment implied for magnetic fields along the $[110]_c$ direction. While the domain formation is well studied in ferromagnetic and ferroelectric materials, much less is known for ferroelastic transitions [26,27]. Ferroelastic domains spontaneously emerge in order to reduce local strains, as illustrated for thin films [26,27]. When cooling a single crystal from the melt, local strains occur, which cause a particular ferroelastic domain arrangement. Indeed, for La$_{2-x}$Sr$_x$CuO$_4$ exhibiting a similar octahedron rotation, it was observed that cooling through the structural transition always reproduces the same domain pattern [28]. The shape-memory effect in SrRuO$_3$ occurring near the ferromagnetic but well below the structural transition seems to be caused by such a strain memory.

Figure 4 shows the magnetization for $\vec{H} \parallel [101]_c$ and $\vec{H} \parallel [010]_c$ obtained in a commercial superconducting quantum interference device (SQUID) magnetometer (Quantum Design)

on partially detwinned crystals. After zero-field cooling the sample to 2 K, the virgin curve of $M(H)$ for $\vec{H} \parallel [101]_c$ rapidly increases to about $0.9\mu_B$/Ru, then it follows almost a plateau until it shows another step at $\mu_0 H_s \simeq 2$ T to a saturation value of $M_{sat} \simeq 1.6\mu_B$/Ru. In the subsequent field-sweep cycle, the intermediate plateau is absent and the $M(H)$ curve essentially switches between the two saturation plateaus with almost no hysteresis. This perfectly agrees with the magnetically induced structural change. In the virgin curve, the magnetic moments of the structural domains with $c \parallel H$ saturate first, then at $\mu_0 H_s \simeq 2$ T the other structural domains reorient and full saturation is reached. In subsequent field-sweep cycles, the sample remains in the structural single-domain state and $M(H)$ switches between 180° magnetic domains.

For $\vec{H} \parallel [010]_c$, the virgin curve of $M(H)$ also rapidly increases, but to a smaller value of $\simeq 0.5\mu_B$/Ru and then $M(H)$ continuously increases to $\simeq 1.4\mu_B$/Ru at $\mu_0 H = 6$ T; see Fig. 4(b). Upon decreasing the field, $M(H)$ does not follow the virgin curve, but approaches a larger remanent magnetization of $M_{rem} \simeq 0.75\mu_B$/Ru in zero field and finally $M(H)$ follows the reverted branch in the negative field range. As discussed above, this different behavior is related to the fact that $\vec{H} \parallel [010]_c$ does not correspond to the magnetic easy axis of any of the six orthorhombic twin orientations. Thus, M_{rem} stems from the four twins, whose easy axis c is at 45° with respect to $\vec{H}$ (thus $b \perp \vec{H}$), and the two $b \parallel \vec{H}$ orientations with the easy axis perpendicular to $\vec{H}$ do not contribute. With $M_{sat} \simeq 1.6\mu_B$/Ru, the occupation of the four contributing twin orientations in zero field can be estimated by $\sqrt{2}M_{rem}/M_{sat} \simeq 2/3$, yielding an equal domain population after the field decrease. The smaller initial increase in the virgin curve yields a population of only 40% for the four contributing $b \perp \vec{H}$ orientations, while the two noncontributing twins with $b \parallel \vec{H}$ would be populated by about 60%. This means that the initial field increase causes a sizable reorientation of structural domains, but this reorientation is rather gradual. These gradual changes most probably result from the fact that the magnetization cants from the respective easy-axis direction towards $\vec{H}$.

From an extrapolation of the measured $M(H)$ for $\vec{H} \parallel [010]_c$, one may estimate the intrinsic anisotropy field to $\mu_0 H_{an} \approx 10$ T, which agrees with the energy of the ferromagnetic resonance observed in time-resolved magneto-optical Kerr effect measurements [29]. A similar intrinsic anisotropy may be expected for the orthorhombic a direction, but this anisotropy remains hidden by the structural domain reorientation.

The magnetic-field-induced control of structural domains in SrRuO$_3$ is remarkable in view of the largely different magnetic and structural transition temperatures. The spin-orbit coupling in this $4d$ material is, however, significantly larger than in the well-studied $3d$ oxides. Thus, the elongation of the RuO$_6$ octahedron along c results in a sizable easy-axis anisotropy with an anisotropy field $\mu_0 H_{an} \approx 10$ T. This prevents magnetic spin-flop transitions in fields of the order of 1 T, but the magnetic energy $-\mu_0 \vec{H}\vec{M}$ can be gained by structural domain flops. Thus, a strong Ising anisotropy and weak pinning of structural domains are required, both of which seem to be fulfilled in SrRuO$_3$. The involved magnetic energy density can be estimated from $M_{sat} \simeq 1.6\,\mu_B$/Ru, the switching field $\mu_0 H_s \simeq 1.8$ T of the domain flop, and the volume per formula unit $V_{fu} \simeq 60$ Å^3 to $E_{mag} = \mu_0 H_s M_{sat}/V_{fu} \approx 0.4$ MPa. This small energy density is sufficient to induce a detwinning with macroscopic length changes up to several 10^{-3} in $\Delta L_i/L_0$, whereas comparable elastic distortions in usual single-domain solids would require energy densities in the GPa range. The field-induced domain flop seems to be visible already in the very early data of Kanbayasi [30], who reported anomalous switching effects and a tetragonal symmetry in flux-grown single crystals in higher fields. Moreover, the strange angular hysteresis in the magnetoresistance of thin-film samples is probably also related to structural domain flops [31].

In conclusion, the combination of neutron diffraction with macroscopic measurements reveals the magnetic control of structural domains in SrRuO$_3$. Applying magnetic fields of the order of only 1 T along one of the cubic $[110]_c$ directions, which by symmetry can become an orthorhombic c direction, induces a structurally single-domain state with the magnetic easy axis c aligned along the field. This single-domain state is stable at low temperatures so that successive magnetic field cycles yield narrow magnetic hysteresis loops without further structural domain changes. Rotating the field to another symmetry-equivalent cubic direction, e.g., $[\bar{1}10]_c$, even allows one to switch between different symmetry-equivalent single-domain states. Upon heating above the Curie temperature, the initial domain arrangement recovers and reveals the magnetic shape-memory effect. Magnetic fields along a cubic $[010]_c$ direction, which cannot become an easy axis, also induce a partial domain reorientation, but the intrinsic magnetic anisotropy of the order of 10 T remains visible. The magnetic field control of structural domains in SrRuO$_3$ arises from the large magnetic anisotropy due to the strong spin-orbit coupling in this $4d$ transition-metal oxide combined with the weak pinning of the structural domain walls. A similar control of structural domains should also be observable for other ferroic transitions, such as ferroelectric instabilities.

[1] D. Khomskii, Physics **2**, 20 (2009).

[2] G. Koster, L. Klein, W. Siemons, G. Rijnders, J. S. Dodge, C.-B. Eom, D. H. A. Blank, and M. R. Beasley, Rev. Mod. Phys. **84**, 253 (2012).

[3] K. Ullakko, J. K. Huang, C. Kantner, R. C. O'Handley, and V. V. Kokorin, Appl. Phys. Lett. **69**, 1966 (1996).

[4] A. Planes, Physics **3**, 36 (2010).

[5] A. Planes, L. Mañosa, and M. Acet, J. Phys.: Condens. Matter **21**, 233201 (2009).

[6] A. N. Lavrov, S. Komiya, and Y. Ando, Nature (London) **418**, 385 (2002).

[7] J. J. Randall and R. Ward, J. Am. Chem. Soc. **81**, 2629 (1959).

[8] T. Kiyama, K. Yoshimura, K. Kosuge, Y. Ikeda, and Y. Bando, Phys. Rev. B **54**, R756(R) (1996).

[9] P. B. Allen, H. Berger, O. Chauvet, L. Forro, T. Jarlborg, A. Junod, B. Revaz, and G. Santi, Phys. Rev. B **53**, 4393 (1996).

[10] M. Izumi, K. Nakazawa, Y. Bando, Y. Yoneda, and H. Terauchi, J. Phys. Soc. Jpn. **66**, 3893 (1997).

[11] Z. Fang, N. Nagaosa, K. S. Takahashi, A. Asamitsu, R. Mathieu, T. Ogasawara, H. Yamada, M. Kawasaki, Y. Tokura, and K. Terakura, Science **302**, 92 (2003).

[12] Y. Kats, I. Genish, L. Klein, J. W. Reiner, and M. R. Beasley, Phys. Rev. B **70**, 180407(R) (2004).

[13] N. Haham, Y. Shperber, M. Schultz, N. Naftalis, E. Shimshoni, J. W. Reiner, and L. Klein, Phys. Rev. B **84**, 174439 (2011).

[14] S. Itoh, Y. Endoh, T. Yokoo, S. Ibuka, J.-G. Park, Y. Kaneko, K. S. Takahashi, Y. Tokura, and N. Nagaosa, Nat. Commun. **7**, 11788 (2016).

[15] N. Kikugawa, R. Baumbach, J. S. Brooks, T. Terashima, S. Uji, and Y. Maeno, Cryst. Growth Des. **15**, 5573 (2015).

[16] S. Kunkemöller, F. Sauer, A. A. Nugroho, and M. Braden, Cryst. Res. Technol. **51**, 299 (2016).

[17] S. Cuffini, J. Guevara, and Y. Mascarenhas, Mater. Sci. Forum **228**, 789 (1996).

[18] C. W. Jones, P. D. Battle, P. Lightfoot, and W. T. A. Harrison, Acta Crystallogr., Sect. C **45**, 365 (1989).

[19] B. Chakoumakos, S. Nagler, S. Misture, and H. Christen, Physica B **241–243**, 358 (1998).

[20] Throughout this Rapid Communication we refer to the orthorhombic lattice, unless the cubic system is specified by a subscript. Note that in space group $Pnma$ the octahedron rotates around the orthorhombic b axis and tilts roughly around the a axis and that $a < c$, indicating an elongation of the octahedron basal plane along c in SrRuO$_3$.

[21] See Supplemental Material at http://link.aps.org/supplemental/10.1103/PhysRevB.96.220406 for results of the crystal structure determination performed with single crystals of SrRuO$_3$ by neutron diffraction at 10 and 170 K.

[22] V. Petříček, M. Dušek, and L. Palatinus, Z. Kristallogr. **229**, 345 (2014).

[23] Data obtained at D3 are available at http://dx.doi.org/10.5291/ILL-DATA.5-51-519.

[24] S. Lee, J. R. Zhang, S. Torii, S. Choi, D.-Y. Cho, T. Kamiyama, J. Yu, K. A. McEwen, and J.-G. Park, J. Phys.: Condens. Matter **25**, 465601 (2013).

[25] The uniaxial-pressure detwinning procedure [16] is not fully reproducible, because it depends on the initial twinning of the sample implied by its local strains. Applying the magnetic field along a $[010]_c$ direction was also found to induce changes of the twinning fractions that were not reversed upon heating until room temperature.

[26] A. L. Roitburd, Phys. Status Solidi A **37**, 329 (1976).

[27] I. A. Luk'yanchuk, A. Schilling, J. M. Gregg, G. Catalan, and J. F. Scott, Phys. Rev. B **79**, 144111 (2009).

[28] M. Braden, G. Heger, P. Schweiss, Z. Fisk, K. Gamayunov, I. Tanaka, and H. Kojima, Physica C **191**, 455 (1992).

[29] M. C. Langner, C. L. S. Kantner, Y. H. Chu, L. M. Martin, P. Yu, J. Seidel, R. Ramesh, and J. Orenstein, Phys. Rev. Lett. **102**, 177601 (2009).

[30] A. Kanbayasi, J. Phys. Soc. Jpn. **41**, 1879 (1976).

[31] M. Ziese, I. Vrejoiu, and D. Hesse, Phys. Rev. B **81**, 184418 (2010).

Magnetic shape-memory effect in SrRuO$_3$

S. Kunkemöller,[1] D. Brüning,[2] A. Stunault,[3] A. A. Nugroho,[4] T. Lorenz,[2] and M. Braden[2, *]

[1]*II. Physikalisches Institut, Universität zu Köln, Zülpicher Str. 77, D-50937 Köln, Germany*
[2]*II. Physikalisches Institut, Universität zu Köln, Zülpicher Str. 77, D-50937 Köln, Germany*
[3]*Institut Laue Langevin, 71 Avenue des Martyrs, CS 20156, F-38042 Grenoble Cedex 9, France*
[4]*Faculty of Mathematics and Natural Science, Institut Teknologi Bandung, Jalan Ganesha 10, 40132 Bandung Indonesia*

TABLE S-I. Crystal structure parameters of SrRuO$_3$ obtained from the single-crystal neutron diffraction experiment. Two sets of reflections were recorded at 170 and 10 K consisting of 1147 and 1642 reflections on the D9 neutron four-circle diffractometer, respectively, using an as-grown single crystal of SrRuO$_3$. Friedel-equivalent reflections were averaged yielding 617 and 833 symmetrically different ones with R$_{int}$ values of 2.28 and 2.33 % for the datasets. A gaussian extinction correction of type I is applied. The refinements yield R values of $wR(all)$ = 4.74 and 4.54 % for 10 and 170 K. Because the refinement yielded slightly negative U_{22} values for O1, isotropic atomic displacement parameters were applied to the oxygen positions. The atomic positions are given in fractions of the unit cell, the atomic displacements are given in Å^2, values in brackets indicate the error on the last digits. Twinning fractions are given for the 6 domain orientations for both temperatures.

10 K	twin 1,2,3	0.287(8)	0.326(4)	0.121(4)
	twin 4,5,6	0.134(3)	0.065(3)	0.066(3)
	Sr	Ru	O1	O2
x	0.0219(2)	0	−0.0045(3)	0.2783(3)
y	0.25	0	0.25	0.02855(13)
z	−0.0036(5)	0.5	0.4460(3)	0.7224(2)
ai	1	1.033(8)	0.971(13)	1.054(10)
U_{11}	0.0052(7)	0.0063(7)	0.0039(5)	0.0079(4)
U_{22}	0.0017(8)	0.0052(8)	0.0039	0.0079
U_{33}	0.0038(8)	0.0018(8)	0.0039	0.0079
U_{12}	0	0.0013(4)	0	0
U_{13}	0.0003(5)	0.0019(13)	0	0
U_{23}	0	0.0004(7)	0	0

170 K	twin 1,2,3	0.282(7)	0.329(4)	0.125(3)
	twin 4,5,6	0.131(3)	0.066(3)	0.066(3)
	Sr	Ru	O1	O2
x	0.0208(2)	0	−0.0033(3)	0.2786(3)
y	0.25	0	0.25	0.0299(2)
z	−0.0035(5)	0.5	0.4465(4)	0.7223(3)
ai	1	1.038(9)	0.938(13)	1.060(10)
U_{11}	0.0086(8)	0.0071(9)	0.0048(6)	0.0112(4)
U_{22}	0.0027(13)	0.0144(17)	0.0048	0.0112
U_{33}	0.0089(9)	0.0030(9)	0.0048	0.0112
U_{12}	0	0.0008(4)	0	0
U_{13}	0.0003(5)	0.0017(15)	0	0
U_{23}	0	0.0013(7)	0	0

Chapter 3

Further Topics

3.1 Single-crystal growth of layered Ruthenates in a mirror furnace

Growing a crystal is, by its very nature, the first step when performing a solid state experiment. Sample availability and sample quality are limiting factors in a special manner in research of layered Ruthenates. This applies particularly to neutron scattering experiments as there is the need of bigger samples than for most other experiments in experimental solid state physics. The lack of samples, which are big enough for neutron scattering is impressively demonstrated by some thousand publications on the ferromagnetic compound $SrRuO_3$ [24] but no reports of single-crystal neutron-scattering experiments investigating the magnetism on a microscopic level. Also the sample purity plays a crucial role in research of layered Ruthenates. Here, the most famous example of the relation of physical properties and sample quality is the suppression of the superconducting state in Sr_2RuO_4 by impurities [50]. Another example is the occurrence of quantum oscillations in $SrRuO_3$ [51]. The past has shown that the crucible-free optical floating zone technique is superior in comparison to other methods like flux growth regarding the sample quality and crystal size of layered Ruthenates. One example is $SrRuO_3$. Crystals are grown with a flux technique, the floating zone technique and thin films with several techniques, but the samples grown with the floating zone are the biggest and of purest quality indicated by the residual resistivity ratio and the coercive field [51, 44, 25].

A successful single crystal growth of a layered Ruthenate has to overcome two major problems. The possible intergrowth of different layered arrangements and the volatility of RuO_2. The layers of Ruthenates can epitaxially grow in different stackings [52]. In order to get a single-phase single crystal the growth parameters have to be accurately optimized and the stoichiometry has to be controlled, which is challenging due to the high volatility of RuO_2 during the crystal growth in a mirror furnace. In some cases more than 50% of the Ru is lost due to evaporation. The volatility of Ru depends on many parameters like temperature, atmosphere

content, pressure, growth speed, speed of the feed rod, diameter of the feed rod, size and shape of the molten zone. If the evaporation is not accurately controlled and compensated by the composition of the feed rod, the stoichiometry of the grown crystal becomes wrong. This can become visible in several ways. A Ru excess can produce intergrowth of other members of the Ruddlesden-Popper series with higher n or Ru metal or Ru oxide impurity phases. In Ru poor samples, members of the Ruddlesden-Popper series with lower n and non-Ru oxides or Ru defects can form (see 3.1.1). As a consequence of the optimization of the growth parameters the Ru excess has to be altered and the optimum has to be found out for every change of the growth parameters. Only in cases where the excess of Ru in the feed rod accurately compensates the evaporation of the RuO_2, a reliable evaluation about the quality of the growth parameters can be made.

The growth of all crystals was performed using the equipment, and following the procedure described in Ref. [25].

During this thesis one infinity and several single layered Ruthenates could be grown:

- $SrRuO_3$ (in total 10 g)
- $Ca_2Ru_{1-y}Ti_yO_4$, y=0,1,3,5,10 %

3.1.1 Optimization of growth parameters

3.1.1.1 $Ca_2Ru_{1-y}Ti_yO_4$

For the optimized crystal growth a sinter temperature of 1350 °C and a duration of 3 h was used, a Ru excess of 33.5 %, a crystal growth speed of 17 mm h^{-1}, a feed rod speed of 20 mm h^{-1}, a rotation speed of 20 rpm counterclockwise, a pressure of 10 bar, a gas mixture of 90 % Ar and 10 % O and a gas flow of 5 l min^{-1}. The necessity of variation of the parameters with changing titan content could not be observed.

Variation of the sintering atmosphere led to enhanced or reduced evaporation of RuO_2, enhancement in case of a higher O partial pressure and reduction in case of a lower O partial pressure than at ambient conditions. This became apparent in the XRD powder patterns, in which more of less RuO_2 was found for the alternated sintering atmosphere. In some attempts in which a lower O partial pressure was used, parts of the feed rod did not melt properly, which resulted in a failure of the single crystal growth.

Several attempts with a higher growth speed were performed. For a speed of 40 mm/h no single crystalline material could be obtained and for 25 and 20 mm/h only small single crystalline grains could be obtained.

Using a higher feed-rod speed naturally results in crystals with bigger diameters, which is of course desirable. But attempts with a high feed rod speed always resulted in non-homogeneous crystals. There was a radial gradient of Ru content in the crystals. In RuO$_2$ rich crystals the inner parts were not single crystalline like the outer parts and contained an excess of RuO$_2$, which became apparent in XRD powder patterns. In RuO$_2$ deficient crystals cracks occurred during the growth process in the mirror furnace, which hampered the crystal growth.

Increasing the O partial pressure results in a raised formation of 327 phase, which became apparent in XRD powder patterns. For lower O partial pressure the feed rod did not melt properly and no crystal could be grown.

The total pressure and the rotation speed were the same in all attempts.

If the evaporated RuO$_2$ during the growth in the mirror furnace was not accurately compensated, then the 327 phase grew. For an excess of RuO$_2$ and in case of a lack of RuO$_2$, cracks formed in the crystal during the crystal growth, which frequently ended the growth process.

With a few exceptions the resulting crystals are twinned. This seems to depend on the accuracy of the RuO$_2$ evaporation, which must be exactly the amount of excess of RuO$_2$ in the feed rod to get untwinned single crystals. The more accurate the evaporation is compensated, the more volume of the crystal has its orthorhombic *a*-axis close to the growth direction.

3.2 Spin Density in SrRuO$_3$

Polarized neutron scattering reveals an anisotropic spin-density distribution with magnetic density at the Ru and all O positions of SrRuO$_3$. At the Ru position a total magnetic moment of 1.17(5) μ_B and an orbital moment of 0.22(9) μ_B, at the apical O site of 0.15(3) μ_B and at the basal O site of 0.14(3) μ_B are found in perfect agreement with magnetization measurements. The shape of the orbitals with unpaired electrons agree with the interpretation of strong covalency effects due to strong π hopping between Ru d and O p orbitals. This pronounced shape of the spin-density distribution at 2 K does not change much at 200 K.

Neutron scattering is sensitive to both, the nucleus and magnetic moments. For a ferromagnet ($k = 0$) both contributions occur at the same position. Polarized neutron scattering significantly improves the sensitivity of such a diffraction experiment due to the interference term [47]. Here we used polarized neutrons to measure Flipping ratios (R=I$^+$/I$^-$, where I$^{+,-}$ are the neutron scattering intensities for the neutron spin parallel or antiparallel to the applied magnetic field) from which we deduced the spin-density distribution in the unit cell of SrRuO$_3$.

The polarized neutron-scattering measurements were performed at ILL using the Spin Polarized Hot Neutron Beam Facility D3 in the high-field set up with a lifting-counter detector. A 10 T cryomagnet was used and the Heusler monochromator produced a 95 % polarized neutron beam with a wavelength of 0.85 Å. Two Erbium filter were introduced to suppress higher order contaminations.

We used a nearly cubic piece of single crystalline $SrRuO_3$ [25, 26] with a mass of 60 mg. The crystal edges corresponded to the orthorhombic directions. The magnetic field was applied parallel to the c direction. The sample was field cooled down to 2 K in a field of 9 T. The magnetic field has two assignments, aligning the spins of the sample and guiding the neutron spins. A large set of 306 Flipping ratios was measured at 2 K and after heating to 200 K another set of 177 Flipping ratios. These sets contained 92 and 65 symmetrically inequivalent Flipping ratios with weighted R values for equivalent reflexions of 3.98 and 1.41%.

These data were used to obtain the spin density by performing a least square refinement using these lists of Flipping ratios with the program FULPROF [53], and by using the maximum entropy algorithm implemented in the CCSL [54]. With the program FULPROF two models for the spin density were refined. First, a monopol model with a maximum of two parameters per magnetic atom, where the one parameter corresponded to the total magnetic moment and the other one to the orbital moment. Second, a multipol model with which the shape of the spin density could be refined. For that the program FULPROF used the Ru^+ magnetic form factor. A discussion of the justification of this approximation can be found in Ref. [55]. The maximum entropy algorithm is a model-free method to reconstruct the spin density. The structural data were taken from refinements of the data presented in Ref. [26].

The focus of this study is laid on the low temperature spin density. The dataset recorded at 2 T contains more reflections than the dataset recorded at 200 K. These additional reflections are recorded at higher $sin(\Theta)/\lambda$ or are reflections which contain no contribution of the Ru because of its higher symmetric position. This is the reason for the higher weighted R value of the dataset recorded at 2 K. But these data have special importance for the refinement of the orbital moments and of the O contribution to the spin density.

The refinement of the monopol model with the data recorded at 2 K results in a total magnetic moment at the Ru site of 1.17(5) μ_B and an orbital moment of 0.22(9) μ_B, at the apical O site of 0.15(3) μ_B and at the basal O site of 0.14(3) μ_B. These moments make the magnetic moment per formula unit $M_{Ru} + M_{O1} + 2M_{O2} - M_{orbital} = 1.25(7)$ μ_B. At the O sites there are 27% of the total magnetic moment. These large moments at the O sites, resulting from strong covalency effects because of the large pd hopping and the near degeneracy of the Ru t_{2g} and O p_π states [56], are also found experimentally in other layered Ru compounds by neutron scattering [55, 28, 57, 36].
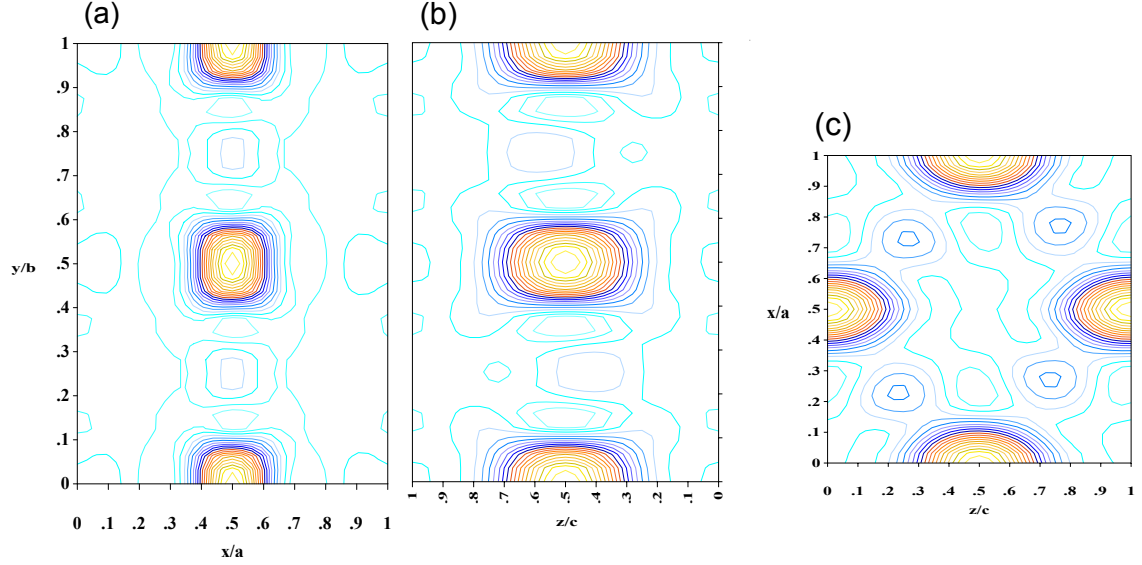
Figure 3.1: *Spin density maps as obtained from fitting a multipol model with the program FULPROF. The maps are obtained with the program GFourier 04.06. The three panel show cuts perpendicular to (a) c, (b) a and (c) b at the unit-cell boundary. The color code denote high spin density in yellow and low spin density in green.*

Table 3.1: *Resulting magnetic moments of the analyzes using different methods and at different temperatures.*

	monopol	multipol	integration mem	SQUID
2 K				
Ru all	1.17(5)	-	0.91	
Ru orbital	0.22(9)	-	-	
O1	0.15(3)	0.16(3)	0.07	
O2	0.14(3)	0.15(2)	0.12	
total	1.24(7)	-	1.21	1.65(3)
200 K				
Ru all	0.28(2)	-	0.29	
Ru orbital	0.11(5)	-	-	
O1	−0.04(2)	0.085(10)	0.025	
O2	0.029(10)	0.018(10)	0.031	
total	0.16(3)	-	0.35	

The small orbital moment is also consistent with observations in the other compounds, underlining once more that the magnetism in Ruthenates can be described mainly by spin moments with a largely quenched orbital moment and that the spin-orbit coupling is relevant but not strong enough to couple S and L to J.

Addressing the anisotropic spin-density distribution demands a fit with a multipol model. Here a model with 14 parameters for the Ru position is fitted. The fit with this model results in significantly smaller R values compared to the fit with the monopol model, a R(1-Flip)W-factor of 16.3 for the multipol model compared to 36.5 for the monopol model. In Fig. 3.1 cuts through the spin-density distribution parallel to the orthorhombic axes can be seen. The spin density around the Ru position becomes clearly anisotropic. The magnetic moments on the O sites become 0.16(3) and 0.15(2) μ_B for the apical and basal O, respectively.

Even more detailed cards of the spin density distribution can be obtained by an image reconstruction using the maximum entropy algorithm from the CCSL. The spin density is discretized into 125000 pixels, 50 in each direction. From this spin-density reconstruction the total magnetic moments can be obtained by numerical integration. The radius for the Ru position is chosen to be 1.2 Å and to 0.9 Å for the O positions. Note that the distance between two neighboring Ru and O ions is less than 2 Å.This leads to magnetic moments of 0.91 μ_B at the Ru site, of 0.07 μ_B at the apical O site and of 0.12 μ_B at the basal O site. Therefore, the total magnetic moment per formula unit amounts to 1.21 μ_B. The study in Ref. [55] also found smaller magnetic moments with the maximum entropy algorithm because of the negative bias of this algorithm against any magnetic spin density. Here, the value of the magnetic moment at the Ru position found by the maximum entropy algorithm is 11% smaller than the magnetic moment found by fitting a monopol model and 60% smaller for the apical O.

The figure with the cuts obtained by the maximum-entropy reconstruction, Fig. 3.2, shows the same cuts like Fig. 3.1, which are obtained by fitting a multipol model. Cuts of the *ab* plane, seen in panels (a), are very similar. Both clearly show the contribution of the apical O lying between the Ru ions placed at (0.5,0), (0.5,0.5) and (0.5,1) and the spin density at the Ru position has notches along the orthorhombic axes in both cuts, to name the two key features. Panels (b) and (c) reveal the largest differences in the spin density obtained by the two different methods. The spin density obtained by the multipol model is clearly more extended in the c direction, even though this feature is also indicated in the cuts obtained by the maximum entropy algorithm. That the largest deviation of the spin density obtained by the two different methods is along the c direction might be rooted in the experimental setup. The c axis of the crystal was mounted parallel to the magnetic field, i.e. vertically. Therefore, this direction was only accessible by moving the lifting counter detector. This movement is limited and only reflections (hkl) with l=0,1,2 could be measured. For h and k there was no limitation.
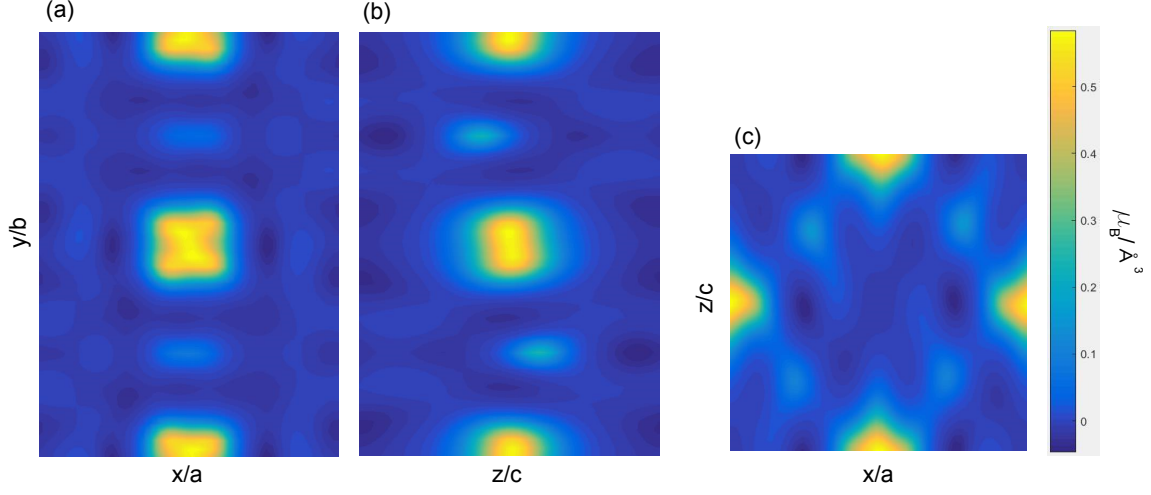
Figure 3.2: *Spin density map at* 2 K *as obtained by the maximum entropy algorithm. The same cuts like in Fig. 3.1 are shown.*

Figure 3.3: *Spin density maps at 2 K as obtained by the maximum entropy algorithm. (a) shows a cut perpendicular to* $[10-1]$, *which cuts the O octahedrons nearly at their corners. So the Ru position is in the middle of the picture. (b) shows a cut perpendicular to that shown in (a), again, the Ru position is placed at the middle of the picture. (c) shows a cut in the same direction like (b), but a basal O is placed in the middle of the picture. (d) shows a cut perpendicular to b at* $y = 0$.
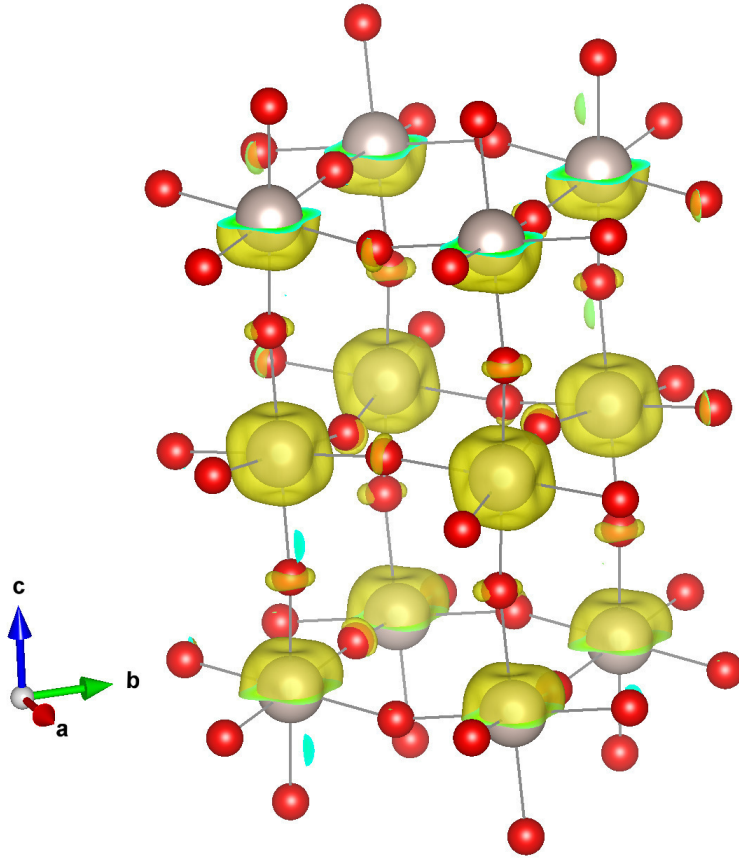
Figure 3.4: *Iisosurfaces of the spin density as obtained by LDA calculations. The isosurfaces of the magnetic density in yellow . The gray and red balls denote the Ru and O ions, respectively. Next-nearest neighbor ions are connected by gray lines. The picture is provided by S. V. Streltsov*

The details of the spin-density distribution allow one to draw conclusions about the orbital occupation with unpaired electrons. Therefore, cuts along the diagonals of the a- and c-axes, close to the high temperature cubic directions, which cuts the O octahedrons nearly at their corners, are performed, and can be seen in Fig. 3.3. There a cut parallel to the a, c plane is presented. The spin-density distribution at the O position points to an imbalance of the orbital occupation of the p orbitals. The O orbitals which allow a π hopping are those with less extension in the direction to the Ru position. This feature is clearly seen at both O positions, but seems to be more pronounced at the apical O position. These experimental observations support the conclusion drawn from calculations, which revealed strong π hopping between the Ru d and O p orbitals [56]. The spin density at the Ru position is quite isotropic along the orthorhombic directions. This points to an equal occupation of all the Ru t_{2g} bands.

The calculated spin density in the LSDA approximation performed by Z. Pchelkina

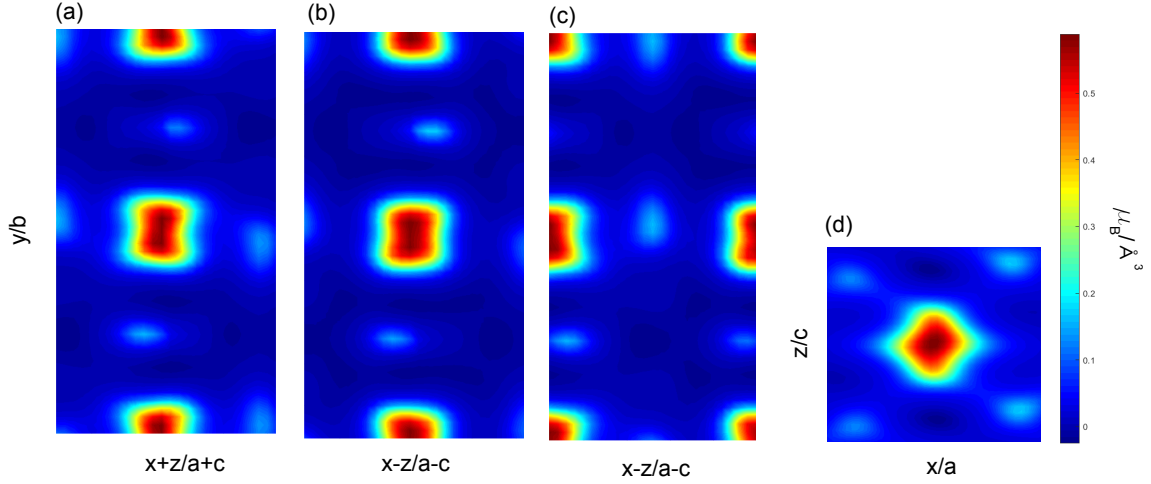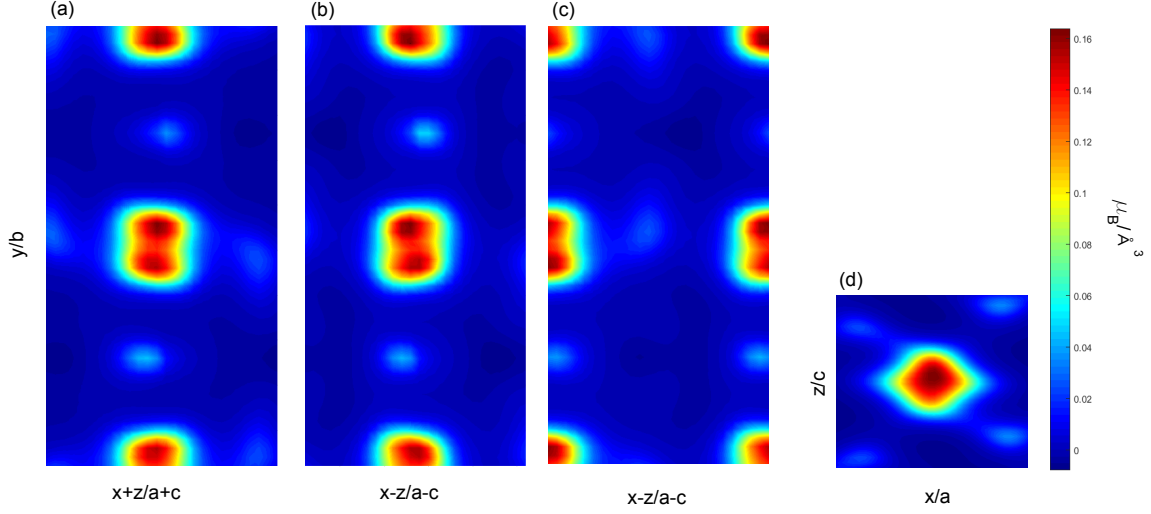**Figure 3.5:** *Spin density maps at 200 K as obtained by the maximum entropy algorithm. The same cuts as in Fig. 3.3 are shown, but obtained by the data recorded at 200 K.*

and S. V. Streltsov can be seen in Fig. 3.4. Isosurfaces of the spin density are shown in yellow, while the Ru ions are indicated by gray and the O by red balls. Next-nearest neighbor ions are connected by gray lines. In these calculations the Hubbard U is set to zero ($U = 0$ meV). The calculated O contribution is in full agreement with the spin density obtained by experiment. Even the flat shape with less extension in the direction of the neighboring Ru ions is perfectly found. The spin density around the Ru positions is also quite isotropic along all three orthorhombic directions and the notches are also found in accordance with the experiment.

Figure 3.5 shows the spin-density reconstruction obtained by the maximum entropy algorithm for the data recorded at 200 K. The shape of the distribution does not change a lot. The main difference is the reduced total moment at this higher temperature. The result of the integration of the moments is 0.293 μ_B at the Ru position, 0.0248 μ_B at the apical O position, 0.0312 μ_B at the basal O position, in total 0.347 μ_B per formula unit. The integration over the whole unit cell results in 0.2932 μ_B per formula unit.

In conclusion the spin-density distribution of SrRuO$_3$ could be obtained by either refining a model to the measured Flipping ratios or by reconstructing the distribution with a maximum entropy algorithm. The obtained total magnetic moments per formula unit by these two methods agree with the magnetization measurements. A O contribution to the spin density of about one third is observed. The shape of this contribution proves experimentally that the π hopping between the Ru d and O p is the most likely hopping. The shape of the spin density around the Ru position indicates a quite equal occupation of the Ru t_{2g} orbitals. To solve the question of the magnetic anisotropy, demands specialized calculations in connection with more

detailed experiments on the magnetism in $SrRuO_3$. A better resolution of the spin density along the c direction, which was not achievable in the used set up, and details of the magnon dispersion in an orthorhombic setting, from which more accurate exchange parameter should be obtained, are desired.

Chapter 4

Discussion

The strongest cohesion of the present work is the compound point of view. All samples are (distorted) Ruddlesden-Popper Ruthenates. That is originated in the similarity of the growth process. All compounds could be grown with the floating-zone method and the specialties in the growth process are the same for all grown samples, see 3.1.

A second cohesion are the used experimental methods. The method used for crystal growth is solely the floating-zone method and the central measurement method is neutron scattering. But the variety of the used measurement methods is quite large. Several neutron scattering techniques are used, diffraction and inelastic techniques both with and without controlling the polarization of the neutron, X-Ray scattering techniques using several experimental setups and magnetization as well as resistivity measuring methods.

Even though the crystal structure of all analyzed compounds has large similarity, the Ru is surrounded by the O forming an octahedron, which are corner connected, the physical properties reveal a huge diversity. A very prominent example of layered Ruthenates, where small changes in the chemical composition and crystal structure have a large impact on the physical properties is the series $Ca_xSr_{2-x}RuO_4$, which connects the Mott-Insulator Ca_2RuO_4 [12, 13] with the superconductor Sr_2RuO_4 [7] and includes a spin-density wave [9, 10] and metamagnetism [8, 11].These changes of the ground state are induced by substituting the isovalent Ca by Sr, which change the oxygen octahedrons, the rotation and distortion of the shape [6]. In the present work three compounds of this series are investigated, the Mott-Insulator Ca_2RuO_4 with Ti substitutions, $Ca_{0.5}Sr_{1.5}RuO_4$ with a spin-density wave and the superconductor Sr_2RuO_4. The last investigated compound in the present work is $SrRuO_3$, a ferromagnetic metal, which is the infinite layered Strontiumruthenate.

Despite this numerousness of physical properties in the layered Ruthenates there are central themes occurring in the research. One is competing magnetic correlations and, another one, is the spin-orbit coupling.

This concluding discussion sheds light on the presented scientific work from several viewpoints, first, from the point of neutron scattering techniques, then lying the focus on the advances in sample preparation and third from two physical points of view, magnetic correlations and spin-orbit effects.

4.1 The neutron scattering point of view

Once more, neutron scattering using large high-quality single crystals is proven to be a powerful technique to study magnetism on a microscopic level. All the unique experimental possibilities provided by neutron scattering, (1) to study magnetic excitations in the whole Brillouin zone, (2) to determine magnetic ordering and (3) the high sensitivity to detect light atoms in scattering experiments, play a key role in the present work. The top discoveries of the neutron scattering studies conducted in this work are:

(1a) The magnon dispersion of Ca_2RuO_4 was determined throughout the whole Brillouin zone giving an important contribution to the discussion of the ground state of this compound and revealing the enhanced strength of spin-orbit coupling in that 4d system [35, 36].

(1b) The incommensurable magnetic fluctuations in Sr_2RuO_4 , which are induced by the Fermi-surface nesting of the quasi one-dimensional bands, were studied in the superconducting and non-superconducting state up to very low energies, far below the expected cooper-pair binding energies. Therefore, it is strongly suggested that the one dimensional band are not the active bands driving the superconductivity [22].

(2a) A spin-density wave has been confirmed in $Ca_{0.5}Sr_{1.5}RuO_4$. The propagation vector amounts to $(0.305, 0.305, 1)$ and the spins freeze in like in spin- or cluster-glasses becoming static at about $4\,K$ [10].

(2b) The spin density distribution in the unit cell of $SrRuO_3$ could be reconstructed using polarized neutron diffraction data, see Chap. 3.2.

(3a) The oxygen octahedron rotation of $SrRuO_3$ was determined with high precision very efficiently. Thus, it became possible to shed light on the six-fold twinning of this compound and the changing twinning fraction induced by magnetic fields. A reorientation of the crystal structure in the magnetic phase induced by magnetic fields and a memory effect of the reorientation, which goes in hand with a magnetic shape-memory effect, was discovered in that oxide [26].

Having large and high quality single crystals is a necessary condition for all these neutron scattering experiments which reveal these physical properties. Performing

neutron scattering experiments demands larger crystals than most of the other experimental methods used in physical research.

The smallest crystal used in a neutron scattering experiment of the present work, a $SrRuO_3$ crystal, has been used for diffraction experiments. In these experiments the optimal crystal size is most of the times not the largest one available, because of extinction effects. So, on the one hand, larger crystals increase the intensity of scattered beam, but, on the other hand, also the extinction is increased, which reduces the intensities of the single reflections in a complex manner. The size of the used crystals was about 2x2x2 mm. With these crystals the extinction became perceivable but not too harmful [25, 26].

The diffraction experiment on $Ca_{0.5}Sr_{1.5}RuO_4$ used the largest crystal available. The mass of this crystal was 20 times larger than the mass of the $SrRuO_3$ crystal [10, 26]. In this experiment the focus lay on the detection of very few and weak magnetic reflections and their position. Thus, the maximum available ratio of the intensity of the peak to the background was the main criteria of the crystal choice. As extinction effects only increased the uncertainty in the determination of the ordered moment, which was performed by comparing strong Bragg reflections to magnetic ones, the largest crystal available was chosen [10].

In several inelastic neutron scattering experiments in the present work more than one crystal was used; several crystals were coaligned [35, 36, 22]. The largest assembly of crystals mounted in this work consisted of 7 crystals with a total mass of $9\,g$ and was used in a time-of-flight neutron scattering experiment [58].

The coalignment of crystals with an accuracy of two degrees can be achieved with Cologne's Laue-diffraction equipment easily, which does not imply quickly. A better coalignment of one degree needs some effort. A accuracy of two degrees is perfectly fine for the performed thermal triple-axis neutron scattering experiments. Using ILLs IN8 in a double focusing configuration even allows for much worse mosaic spreads, which naturally arise in twined Ca_2RuO_4 crystals [35]. Using cold triple-axis spectrometers a better mosaic spread is desirable. In the diffraction experiment using ILLs D9 the mosaic spread of 0.5 degree and the non-gaussian and non-isotropic distribution of the structural domains prevented the determination atomic positions being more accurate [26] than the results of neutron powder experiments [59] or X-Ray diffraction experiments [60, 25].

4.2 The sample preparation point of view

All single crystals used in the present work were grown by the optical floating zone technique as this is the method of choice in the growth of Ruddlesden-Popper Ruthenates [50, 31, 42, 61, 44, 25]. With this method not only the largest, but

also the purest crystals could be grown [50, 42, 44, 25]. The purity of the crystals is of outstanding importance in the research of layered Ruthenates as some of the most interesting physical properties only occur in very pure crystals like the superconductivity in Sr_2RuO_4 [50] or the metamagnetism associated with quantum criticality in $Sr_3Ru_2O_7$ [29, 62].

Progress in the crystal growth of layered Ruthenates is achieved in the present work in several regards, (1) new chemical substitutions are established, (2) larger crystals than ever of certain compounds were grown and (3) purer crystals than the already existing could be obtained.

(1a) To date, the substitution of Ti in Ca_2RuO_4 is not mentioned in the literature elsewhere (to our best knowledge). This substitution is also studied in many other layered Ruthenates [63, 33, 64, 65]. Studying substitution series is a common approach in solid state physics. The most prominent series of chemical substitutions in the layered Ruthenates is the series $Ca_xSr_{2-x}RuO_4$ [31], which links the Mott-insulator Ca_2RuO_4 [12] with the superconductor Sr_2RuO_4 [7]. In the present work several Ca_2RuO_4 single crystals with Ti substitutions could be grown, compounds which were never grown before.

(2a) Carlo et al. [9] vainly tried to find a magnetic peak in $Ca_{0.5}Sr_{1.5}RuO_4$. They could not pick up a conclusive signal even though they searched at the correct position in the Brillouin zone. We could find this signal and even prove the direction of the magnetic moment by polarized neutron scattering [10]. With the polarization analysis one easily loose two orders of magnitude of signal strength. It seems to be unlikely that the instrument we chose is the only reason for the better performance of our experiment compared to Carlo et al.. Our crystal seems to be much larger than their crystal. An important aspect to achieve a better ratio of the peaks amplitude to the background.

(2b) The size of the $SrRuO_3$ crystals grown in the present work allow for the first time to conduct neutron scattering experiment using single crystals of $SrRuO_3$ [25]. Despite the huge interest in that compound, documented by some thousand publications on this compound [24], there are no reports of single-crystal neutron-scattering experiments investigating the magnetism on a microscopic level.

(2c) Moreover, larger crystals than the available crystals to date could be grown in the case of Ca_2RuO_4 [35, 36]. These crystals tend to not survive the first order structural phase-transition slightly above room temperature [37, 38]. For neutron scattering experiments using single crystals a lot of these pieces must be coaligned [39]. In this work the breaking of the crystals into small pieces at the structural phase transition could be overcome in two ways. In both cases the phase transition is broadened, in the first case by introducing small amounts of Ti and in the second case by growing a crystal with a bad mosaic

spread (about 4 degrees). That turned out to be sufficient to obtain crystals with a mass of about $1\,g$ [35, 36].

(3a) One of these Ca_2RuO_4 crystals with 1% Ti turned out to be an untwinned one. With this crystal it was possible to determine the propagation vector of the magnetic ordering [36]. There are two possibilities for this vector [66] in Ca_2RuO_4 and it was only possible to unambiguously determine this vector with an untwinned crystal.

(3b) The $SrRuO_3$ crystals grown in the present work are crystals of purest quality indicated by the residual resistivity ratio and the coercive field compared to the crystals grown by flux method or thin films [51, 44, 25], which were the only available crystals at the starting of this thesis.

4.3 Physical points of view

Competing magnetic fluctuations and spin-orbit coupling link the research of layered Ruthenates. A milestone in the discussion of magnetic fluctuations in the layered Ruthenates is the proposal that ferromagnetic fluctuations are the driving force behind the binding of the Cooper pairs in Sr_2RuO_4 [15]. The discussion of spin-orbit-coupling in the Ruthenates became prominent more recently.

4.3.1 Magnetic correlations

Several kinds of magnetic correlations occurring in layered Ruthenates. There are truly ferro- and antiferromagnetic correlations, which even lead to static ferro- or antiferromagnetic ordering [23, 12]. Another static magnetic order in layered Ruthenates is a spin-density wave with a propagation vector of $(0.3, 0.3, 1)$ [33]. But there are even more possible propagation vectors for magnetic correlations in layered Ruthenates. For a summarizing article discussing these incommensurate correlations see Ref. [67].

The correlations are not restricted to one propagation vector in one compound. An impressive example is Ca_2RuO_4 , the ground state is antiferromagnetic but applying pressure leads to static ferromagnetic order [68].

All kind of known static magnetic order in the layered Ruthenates play a role in the present work. The magnon dispersion of the antiferromagnet Ca_2RuO_4 was investigated in detail shedding light on the role of spin-orbit coupling in that compound, see 4.3.2.

The incommensurable spin-density wave was confirmed in $Ca_{0.5}Sr_{1.5}RuO_4$ [10]. These magnetic fluctuations are also present in Sr_2RuO_4 [49] and are considered as an option to be the driving force behind the coupling of the Cooper pairs [18]. By analyzing these magnetic fluctuations using inelastic neutron scattering in the present work, this could be ruled out.

Another option for the coupling of the Cooper pairs are ferromagnetic fluctuations [15]. The initial proposal was inspired by the ferromagnetism of $SrRuO_3$. In the present work the confusion regarding the anisotropy of the magnetism in that compound [24] could be solved by respecting the change of the crystal directions of a $SrRuO_3$ sample in a magnetic field during the performed magnetization measurements [26]. Furthermore the magnetization density in the unit cell could be determined giving insight into the shape of the singly occupied orbitals and the hybridization of the O and Ru orbitals. Knowing that the incommensurable fluctuations in Sr_2RuO_4 are not responsible for the pairing of the spins [22] concentrates the research activities on the ferromagnetic fluctuations and makes the in depth understanding of the ferromagnetism in $SrRuO_3$ an important step towards the understanding of the superconductivity of Sr_2RuO_4 .

4.3.2 Spin-orbit efects

Spin-orbit coupling is the only possibility to couple the spin with the crystal lattice. For most 3d transition-metal compounds one can treat spin-orbit coupling as a weak perturbation. It leads to single-site and exchange magnetic anisotropy, possibly to an antisymmetric (Dzyaloshinskii-Moriya) exchange, and it largely determines the magnetoelastic coupling and magnetostriction. The situation can be different in case of strong spin-orbit coupling, which causes novel phenomena such as the anomalous Hall effect [69], the spin Hall effect [70] and topological insulators [71, 72]. Strong spin-orbit coupling is able to change the character of the multiplet state of the corresponding ions. These strong spin-orbit effects are well established in 5d materials [73] [35].

The next interesting question is, of course, what happens for an intermediate strength of spin-orbit interaction? The Ruthenates, 4d systems, are such systems with intermediate spin-orbit interaction.

In the present work several experiments could be performed, which reveal the strong influence of spin-orbit coupling on the physical properties of layered Ruthenates.

The magnon dispersion of Ca_2RuO_4 possesses huge anisotropy gaps, which are a product of anisotropies of the crystal structure and spin-orbit coupling, which couples the spin to the crystal lattice. These anisotropies govern the dispersion in the whole Brillouin zone [35, 39, 40, 36, 74].

$SrRuO_3$ also possesses strong magnetic anisotropies, even though they are expected to be appreciably weaker. From the magnetization curves a gap of the magnon dispersion of about $1\,meV$ is expected, which is much weaker than the 14 or $40\,meV$ in Ca_2RuO_4. However, this anisotropy is strong enough to change the twinning ratio of a macroscopic crystal by applying a magnetic field of moderate strength. This magnetic field aligns the magnetic moment parallel to the field direction, which changes the oxygen octahedron rotation in a way that the magnetic easy axis is parallel to the field direction. In that case, the lattice constant differences of the orthorhombic crystal structure may lead to a change of the crystal shape [26].

As discussed in the introduction there are two contrary scenarios for the ground state of layered Ruthenates, i.e. for a $4d^{4+}$ configuration in a distorted O octahedron. On the one hand a non-magnetic state, which is stabilized by spin-orbit coupling and a octahedron elongation (S1). And, on the other hand, there is a magnetic ground state with quenched orbital momentum and $S = 1$, which is stabilized by an octahedron contraction and the exchange interaction (S2).

In Sr_2RuO_4 the O octahedron is slightly elongated with no temperature anomaly. Consistently there is no static magnetic order in this compound but, nevertheless, the paramagnetic term dominates the susceptibility [75].

In contrast to this elongated octahedron shape, the octahedra in $SrRuO_3$ and Ca_2RuO_4, which both possess static magnetic order, are contracted at low temperatures. In both compounds the octahedra become more contracted on cooling, which bring the systems closer to S2 [36, 26].

Obviously, in Ca_2RuO_4 S2 is realized because this compound has a magnetic ground state. In the active discussion about the magnetism in Ca_2RuO_4 [76, 34, 35, 39, 40, 74], started by G. Khaliullin, he considered the two scenarios S1 (without exchange interaction) and S2 as a singlet and excited triplet. The excitation in this picture is due to the magnetic exchange interaction at zero temperature and the splitting of singlet and triplet is reduced by a O octahedron flattening, i.e. a suitable non-cubic crystal field. Therefore, in case of similar energy for S1 and S2, there is a quantum critical point. The key feature of this quantum criticality is a longitudinal mode, which changes the amplitude of the magnetic moment. This mode is identified as a Higgs mode [76] and an amplitude mode is found in neutron scattering experiments [40]. But there are more possible reasons for a reduced magnetic moment beside the excitonic scenario, like a hybridization of the Ru $4d$ states with the O $2p$ states, which can result in different averaged oxidation steps to the nominal 4^+ for Ru. This is actually realized in many layered Ruthenates and experimentally proven [55, 57], Chap. 3.2 and, of course, in Ca_2RuO_4 itself [36]. A charge transfer between the O $2p$ states and the Ru $4d$ states can modify the size of the magnetic moment. The source of the amplitude mode is not fully clear yet, but the very small orbital moment of

$0.13\,\mu_{\mathrm{B}}$ points into the direction that Ca_2RuO_4 is far away from the quantum critical point.

The symmetry of the crystal field in Ca_2RuO_4 is even lower than tetragonal, but the splitting induced by this orthorhombic symmetry is much weaker than the splitting induced by the tetragonal crystal field. This becomes apparent in the anisotropy parameters of the magnon dispersion, which differ by more than a factor of ten. The orthorhombic crystal field splits the energy levels of the xz and yz orbitals, increasing the xz and decreasing the yz. Of course, this may lead to an unequal population of these states reducing the ordered magnetic moment.

The analysis of the spin-density distribution of $SrRuO_3$ also revealed a orbital momentum $(0.22(9)\,\mu_{\mathrm{B}})$. This larger orbital momentum points into the direction, that $SrRuO_3$ is closer to the quantum critical point than Ca_2RuO_4. This is also reflected in the smaller contraction of the O octahedra. Therefore the non-cubic crystal field is weaker and $SrRuO_3$ is closer to S1 than Ca_2RuO_4 is, assuming a similar exchange interaction.

Bibliography

[1] C. Fischer and J. Güdler, *Förderatlas 2015* (Wiley-VCH, 2015).

[2] G. Cao and L. DeLong, *Frontiers Of 4d- And 5d-transition Metal Oxides.* (World Scientific, 2013).

[3] W. Witczak-Krempa, G. Chen, Y. B. Kim and L. Balents, Annual Review of Condensed Matter Physics **5**, 57 (2014).

[4] S. N. Ruddlesden and P. Popper, Acta. Cryst. **10**, 538 (1957).

[5] D. I. Khomskii, *Transition Metal Compounds* (Cambridge University Press, 2014).

[6] O. Schumann, Dissertation, *Structural Investigations on layered Manganites and Ruthenates*, Universität zu Köln, (2010).

[7] Y. Maeno, H. Hashimoto, K. Yoshida, S. Nishizaki, T. Fujita, J. G. Bednorz and F. Lichtenberg, Nature (London) **372**, 532 (1994).

[8] S. Nakatsuji and Y. Maeno, Phys. Rev. B **62**, 6458 (2000).

[9] J. P. Carlo, T. Goko, I. M. Gat-Malureanu, P. L. Russo, A. T. Savici, A. A. Aczel, G. J. MacDougall, J. A. Rodriguez, T. J. Williams, G. M. Luke, C. R. Wiebe, Y. Yoshida, S. Nakatsuji, Y. Maeno, T. Taniguchi and Y. J. Uemura, Nature Materials **11**, 323 (2012).

[10] S. Kunkemöller, A. A. Nugroho, Y. Sidis and M. Braden, Phys. Rev. B **89**, 045119 (2014).

[11] S. Nakatsuji, D. Hall, L. Balicas, Z. Fisk, K. Sugahara, M. Yoshioka and Y. Maeno, Phys. Rev. Lett. **90**, 137202 (2003).

[12] S. Nakatsuji, S. Ikeda and Y. Maeno, J. Phys. Soc. Jpn. **66**, 1868 (1997).

[13] S. Nakatsuji, T. Ando, Z. Mao and Y. Maeno, Physica B: Condensed Matter **259-261**, 949 (1999).

[14] J. J. Randall and R. Ward, J. Am. Chem. Soc **81**, 2629 (1959).

[15] T. Rice and M. Sigrist, J. Phys.: Cond. Matter **7**, L643 (1995).

[16] Y. Maeno, T. M. Rice and M. Sigrist, physicstoday **54**, 42 (2001).

[17] A. P. Mackenzie and Y. Maeno, Rev. Mod. Phys. **75**, 657 (2003).

[18] Y. Maeno, S. Kittaka, T. Nomura, S. Yonezawa and K. Ishidak, Journal of the Physical Society of Japan **81**, 011009 (2012).

[19] C. Kallin, Reports on Progress in Physics **75**, 042501 (2012).

[20] A. P. Mackenzie, T. Scaffidi, C. W. Hicks and Y. Maeno, npj Quantum Materials **2**, 40 (2017).

[21] A. P. Mackenzie, T. Scaffidi, C. W. Hicks and Y. Maeno, ArXiv e-prints 1706.01942 (2017).

[22] S. Kunkemöller, P. Steffens, P. Link, Y. Sidis, Z. Q. Mao, Y. Maeno and M. Braden, Phys. Rev. Lett. **118**, 147002 (2017).

[23] A. Callaghan, C. W. Möller and R. Ward, Inorg Chem **5**, 1572 (1966).

[24] G. Koster, L. Klein, W. Siemons, G. Rijnders, J. S. Dodge, C.-B. Eom, D. H. A. Blank and M. R. Beasley, Rev. Mod. Phys. **84**, 253 (2012).

[25] S. Kunkemöller, F. Sauer, A. A. Nugroho and M. Braden, Crystal Research and Technology **51**, 299 (2016).

[26] S. Kunkemöller, D. Brüning, A. Stunault, A. A. Nugroho, T. Lorenz and M. Braden, submitted to Phys. Rev Lett, see also arXiv:1709.05688 (2017).

[27] L. Klein, J. S. Dodge, C. H. Ahn, J. W. Reiner, L. Mieville, T. H. Geballe, M. R. Beasley and A. Kapitulnik, Journal of Physics: Condensed Matter **8**, 10111 (1996).

[28] P. C. Steffens, Dissertation, *Magnetismus in geschichteten Ruthenaten*, Universität zu Köln, (2008).

[29] R. S. Perry, L. M. Galvin, S. A. Grigera, L. Capogna, A. J. Schofield, A. P. Mackenzie, M. Chiao, S. R. Julian, S. I. Ikeda, S. Nakatsuji, Y. Maeno and C. Pfleiderer, Phys. Rev. Lett. **86**, 2661 (2001).

[30] M. K. Crawford, R. L. Harlow, W. Marshall, Z. Li, G. Cao, R. L. Lindstrom, Q. Huang and J. W. Lynn, Phys. Rev. B **65**, 214412 (2002).

[31] S. Nakatsuji and Y. Maeno, Journal of Solid State Chemistry **156**, 26 (2001).

[32] J. Kafalas and J. Longo, Journal of Solid State Chemistry **4**, 55 (1972).

[33] M. Braden, O. Friedt, Y. Sidis, P. Bourges, M. Minakata and Y. Maeno, Phys. Rev. Lett. **88**, 197002 (2002).

[34] A. Akbari and G. Khaliullin, Phys. Rev. B **90**, 035137 (2014).

[35] S. Kunkemöller, D. Khomskii, P. Steffens, A. Piovano, A. A. Nugroho and M. Braden, Phys. Rev. Lett. **115**, 247201 (2015).

[36] S. Kunkemöller, E. Komleva, S. V. Streltsov, S. Hoffmann, D. I. Khomskii, P. Steffens, Y. Sidis, K. Schmalzl and M. Braden, Phys. Rev. B **95**, 214408 (2017).

[37] C. S. Alexander, G. Cao, V. Dobrosavljevic, S. McCall, J. E. Crow, E. Lochner and R. P. Guertin, Phys. Rev. B **60**, R8422 (1999).

[38] O. Friedt, M. Braden, G. André, P. Adelmann, S. Nakatsuji and Y. Maeno, Phys. Rev. B **63**, 174432 (2001).

[39] A. Jain, M. Krautloher, J. Porras, G. H. Ryu, D. P. Chen, D. L. Abernathy, J. T. Park, A. Ivanov, J. Chaloupka, G. Khaliullin, B. Keimer and B. J. Kim, ArXiv e-prints (2015).

[40] A. Jain, M. Krautloher, J. Porras, G. H. Ryu, D. P. Chen, D. L. Abernathy, J. T. Park, A. Ivanov, J. Chaloupka, G. Khaliullin, B. Keimer and B. J. Kim, Nat Phys **13**, 633 (2017).

[41] Z. Mao, Y. Maeno and H. Fukazawa, Materials Research Bulletin **35**, 1813 (2000).

[42] R. Perry and Y. Maeno, Journal of Crystal Growth **271**, 134 (2004).

[43] N. Kikugawa, L. Balicas and A. P. Mackenzie, Journal of the Physical Society of Japan **78**, 014701 (2009).

[44] N. Kikugawa, R. Baumbach, J. S. Brooks, T. Terashima, S. Uji and Y. Maeno, Crystal Growth & Design **15**, 5573 (2015).

[45] G. Dhanaraj, K. Byrappa, V. Prasad and M. Dudley, in *Springer Handbook of Crystal Growth*, hrsg. v. G. Dhanaraj, K. Byrappa, V. Prasad and M. Dudley (Springer, 2010).

[46] W. Marshall and S. W. Lovesey, *Theory of Thermal Neutron Scattering* (Oxford University Press, New York, 1971).

[47] T. Chatterji, *Neutron Scattering from Magnetic Materials* (Elsevier Science, 2005).

[48] G. Shirane, S. M. Shapiro and J. M. Tranquada, *Neutron Scattering with a Triple-Axis Spectrometer* (Cambridge University Press, 2004).

[49] Y. Sidis, M. Braden, P. Bourges, B. Hennion, S. NishiZaki, Y. Maeno and Y. Mori, Phys. Rev. Lett. **83**, 3320 (1999).

[50] Z. Q. Mao, Y. Mori and Y. Maeno, Phys. Rev. B **60**, 610 (1999).

[51] A. P. Mackenzie, J. W. Reiner, A. W. Tyler, L. M. Galvin, S. R. Julian, M. R. Beasley, T. H. Geballe and A. Kapitulnik, Phys. Rev. B **58**, R13318 (1998).

[52] Y. Xin, G. Cao and J. Crow, Journal of Crystal Growth **252**, 372 (2003).

[53] J. Rodríguez-Carvajal, Physica B: Condensed Matter **192**, 55 (1993).

[54] S. F. Gull and J. Skilling, *MEMSYS III Quantified Maximum Entropy Subroutine Library*, Meldreth, UK, 1989.

[55] A. Gukasov, M. Braden, R. J. Papoular, S. Nakatsuji and Y. Maeno, Phys. Rev. Lett. **89**, 087202 (2002).

[56] I. I. Mazin and D. J. Singh, Phys. Rev. B **56**, 2556 (1997).

[57] V. Granata, L. Capogna, F. Forte, M.-B. Lepetit, R. Fittipaldi, A. Stunault, M. Cuoco and A. Vecchione, Phys. Rev. B **93**, 115128 (2016).

[58] K. Jenni et al., To be published .

[59] S. Bushmeleva, V. Pomjakushin, E. Pomjakushina, D. Sheptyakov and A. Balagurov, Journal of Magnetism and Magnetic Materials **305**, 491 (2006).

[60] F. Sauer, Diplomarbeit, University of Cologne, (2015).

[61] R. Fittipaldi, D. Sisti, A. Vecchione and S. Pace, Crystal Growth & Design **7**, 2495 (2007).

[62] S. A. Grigera, R. S. Perry, A. J. Schofield, M. Chiao, S. R. Julian, G. G. Lonzarich, S. I. Ikeda, Y. Maeno, A. J. Millis and A. P. Mackenzie, Science **294**, 329 (2001).

[63] R. F. Bianchi, J. A. G. Carrió, S. L. Cuffini, Y. P. Mascarenhas and R. M. Faria, Phys. Rev. B **62**, 10785 (2000).

[64] P. Steffens, J. Farrell, S. Price, A. P. Mackenzie, Y. Sidis, K. Schmalzl and M. Braden, Phys. Rev. B **79**, 054422 (2009).

[65] X. Ke, J. Peng, D. J. Singh, T. Hong, W. Tian, C. R. Dela Cruz and Z. Q. Mao, Phys. Rev. B **84**, 201102 (2011).

[66] M. Braden, G. André, S. Nakatsuji and Y. Maeno, Phys. Rev. B **58**, 847 (1998).

[67] P. Steffens, O. Friedt, Y. Sidis, P. Link, J. Kulda, K. Schmalzl, S. Nakatsuji and M. Braden, Phys. Rev. B **83**, 054429 (2011).

[68] F. Nakamura, T. Goko, M. Ito, T. Fujita, S. Nakatsuji, H. Fukazawa, Y. Maeno, P. Alireza, D. Forsythe and S. R. Julian, Phys. Rev. B **65**, 220402 (2002).

[69] N. Nagaosa, J. Sinova, S. Onoda, A. H. MacDonald and N. P. Ong, Rev. Mod. Phys. **82**, 1539 (2010).

[70] A. Shitade, H. Katsura, J. Kuneš, X.-L. Qi, S.-C. Zhang and N. Nagaosa, Phys. Rev. Lett. **102**, 256403 (2009).

[71] M. Z. Hasan and C. L. Kane, Rev. Mod. Phys. **82**, 3045 (2010).

[72] X.-L. Qi and S.-C. Zhang, Rev. Mod. Phys. **83**, 1057 (2011).

[73] W. Witczak-Krempa, G. Chen, Y. B. Kim and L. Balents, Annual Review of Condensed Matter Physics **5**, 57 (2014).

[74] G. Zhang and E. Pavarini, Phys. Rev. B **95**, 075145 (2017).

[75] Y. Maeno, K. Yoshida, H. Hashimoto, S. Nishizaki, S. ichi Ikeda, M. Nohara, T. Fujita, A. P. Mackenzie, N. E. Hussey, J. G. Bednorz and F. Lichtenberg, J. Phys. Soc. Jpn. **66**, 1405 (1997).

[76] G. Khaliullin, Phys. Rev. Lett. **111**, 197201 (2013).

Short Summary

Once more, neutron scattering using large high-quality single crystals is proven to be a powerful technique to study magnetism on a microscopic level. Several layered Ruthenate single-crystals could be grown in better quality or larger dimensions than the existing crystals at the starting of this work, enabling the neutron scattering studies [10, 35, 25, 36, 26]. Thus important progress in the research of layered Ruthenates could be achieved:

The incommensurable magnetic fluctuations in Sr_2RuO_4, which are induced by the Fermi-surface nesting of the quasi one-dimensional bands, were studied in the superconducting and non-superconducting state up to very low energy transfers, far below the expected cooper-pair binding energies. Therefore, it is strongly suggested that the quasi one-dimensional bands are not the active band driving the superconductivity [22], giving an important contribution to the question of the symmetry of the superconducting order parameter.

The magnon dispersion of Ca_2RuO_4 was determined throughout the whole first Brillouin zone giving an important contribution to the discussion of the ground state of this compound and revealing the enhanced strength of spin-orbit coupling in that $4d$ system [35, 36].

The oxygen octahedron rotation of $SrRuO_3$ was determined with high precision very efficiently. Thus, it became possible to shed light on the six-fold twinning of this compound and the changing twinning fraction induced by magnetic fields. A reorientation of the crystal structure in the magnetic phase induced by magnetic fields and a memory effect of the reorientation, which goes in hand with a magnetic shape-memory effect, was discovered in that oxide [26].

The spin density distribution in the unit cell of $SrRuO_3$ could be reconstructed using polarized neutron diffraction data, see 3.2.

A spin-density wave has been confirmed in $Ca_{0.5}Sr_{1.5}RuO_4$. The propagation vector amounts to $(0.305, 0.305, 1)$ and the spins freeze in like in spin- or cluster- glasses becoming static at about $4\,K$ [10].

Kurzzusammenfassung

Wieder einmal hat sich die Neutronenstreuung an hochqualitativen Einkristallen als effektive Methode erwiesen, um Magnetismus auf mikroskopischer Ebene zu untersuchen. Eine Vielzahl an geschichteten Ruthenat-Einkristallen konnte während dieser Arbeit gezüchtet werden, die zu Beginn dieser Arbeit noch gar nicht oder nicht in der hier erreichten Qualität und Größe zur Verfügung standen. Diese Kristalle ermöglichten erst den Großteil der hier gezeigten Messungen [10, 35, 25, 36, 26]. So konnte eine ganze Reihe von wissenschaftlichen Erkenntnissen gewonnen werden:

Die inkommensurablen magnetischen Fluktuationen in Sr_2RuO_4, welche induziert werden durch das Fermiflächen Nesting der quasi eindimensionalen Bänder, ist in der supraleitenden und nicht-supraleitenden Phase bis hin zu sehr niedrigen Energieüberträgen, weit unterhalb der zu erwartenden Cooperpaarbindungsenergie, untersucht worden. Als Ergebnis dieser Untersuchungen lässt sich stark vermuten, dass die quasi eindimensionalen Bänder nicht die treibende Kraft der Supraleitung [22] sind, was auch einen wichtigen Beitrag zur Frage der Symmetrie des Ordnungsparameters der Supraleitung leistet.

Die Magnonendispersion in Ca_2RuO_4 ist in der ganzen ersten Brillouinzone bestimmt. Dies ist ein wichtiger Beitrag zur Diskussion um den Grundzustand dieses Systems und hat die erhöhte Stärke der Spin-Bahn Kopplung in diesem $4d$ System offenbart [35, 36].

Die Sauerstoffoktaederrotation in $SrRuO_3$ konnte mit hoher Präzision und sehr effizient bestimmt werden. Damit wurde es möglich die 6-fache Verzwilligung dieses Systems zu erhärten und die sich in einem angelegten Magnetfeld ändernden Zwillingsverhältnisse zu bestimmen. Die Reorientierung der Kristallstruktur in einem angelegten Magnetfeld und der Memory-Effekt dieser Reorientierung, welcher Hand in Hand geht mit einem Formgedächtniseffekt, wurde somit in diesem System entdeckt [26].

Die Spindichteverteilung von $SrRuO_3$ in der Einheitszelle wurde anhand von Daten aus polarisierten Neutronenstreuexperimenten errechnet, siehe 3.2.

Die Spindichtewelle in $Ca_{0.5}Sr_{1.5}RuO_4$ wurde experimentell bestätigt. Der Propagationsvektor ist $(0.305, 0.305, 1)$ und die Spins frieren, ähnlich wie in einem Spin- oder Clusterglas ein, und werden zu einer statischen Ordnung bei $4\,K$ [10].

Own Contributions to the Publications

The following lists the experimental contribution of the author to the publication. All neutron scattering experiments were performed in cooperation with the local contacts and under guidance of Prof. Dr. Markus Braden.

Spin-density-wave ordering in $Ca_{0.5}Sr_{1.5}RuO_4$ studied by neutron scattering: All experiments were already conducted in the authors Diploma thesis. The author grew the crystals and performed the characterization by powder XRD measurements on crushed parts. He performed the resistivity measurements. He conducted the non-polarized neutron scattering experiments and analyzed the data. The results were again analyzed thoroughly in the present work and then the publication was written.

Highly Anisotropic Magnon Dispersion in Ca_2RuO_4: Evidence for Strong Spin Orbit Coupling: The author grew the crystals, performed the characterization by powder XRD measurements on crushed parts and magnetic susceptibility measurements. He conducted the neutron scattering experiments and analyzed the data.

Magnetic anisotropy of large floating-zone-grown single-crystals of $SrRuO_3$: The author grew the crystals, checked phase purity by performing powder XRD measurements on crushed parts, conducted the resistivity measurements, the magnetic characterization and detwined the crystals. He confirmed the successful detwining by XRD measurements using single crystals and one wavelength.

Absence of a Large Superconductivity-Induced Gap in Magnetic Fluctuations of Sr_2RuO_4: The author conducted the neutron scattering experiments at ILL and analyzed these data.
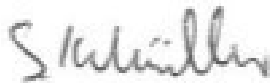
Magnon dispersion in $Ca_2Ru_{1-x}Ti_xO_4$: Impact of spin-orbit coupling and oxygen moments: The author grew the crystals, checked phase purity by performing powder XRD measurements on crushed parts, conducted the resistivity measurements and the magnetic characterization. He conducted the neutron scattering experiments, with exception of the measurements using the IN3 at ILL, analyzed the data and performed the spin-wave calculations using the SpinW program.

Magnetic shape-memory effect in SrRuO$_3$: The author grew the crystals, checked phase purity by performing powder XRD measurements on crushed parts, conducted the magnetic characterization and detwined the crystals. He conducted the neutron scattering experiments and analyzed the data.

Erklärung

Ich versichere, dass ich die von mir vorgelegte Dissertation selbständig angefertigt, die benutzten Quellen und Hilfsmittel vollständig angegeben und die Stellen der Arbeit – einschließlich Tabellen, Karten und Abbildungen –, die anderen Werken im Wortlaut oder dem Sinn nach entnommen sind, in jedem Einzelfall als Entlehnung kenntlich gemacht habe; dass diese Dissertation noch keiner anderen Fakultät oder Universität zur Prüfung vorgelegen hat; dass sie – abgesehen von unten angegebenen Teilpublikationen – noch nicht veröffentlicht worden ist sowie, dass ich eine solche Veröffentlichung vor Abschluss des Promotionsverfahrens nicht vornehmen werde. Die Bestimmungen der Promotionsordnung sind mir bekannt. Die von mir vorgelegte Dissertation ist von Universitätsprofessor Dr. Markus Braden betreut worden.

Köln, den 01.05.2018

Stefan Kunkemöller